ELECTROCATALYSIS ON PtZn SURFACE – FUNDATMENTAL STUDIES AND THE APPLICATIONS IN PEM FUEL CELLS

by

AYA SODE

B.Sc., DALHOUSIE UNIVERISTY, 2002

A THESIS SUBMITTED IN PARTIAL FULFILLMENT OF
THE REQUIREMENTS FOR THE DEGREE OF

DOCTOR OF PHILOSOPHY

in

THE FACULTY OF GRADUATE STUDIES
(Chemistry)

THE UNIVERSITY OF BRITISH COLUMBIA
(Vancouver)

February 2009

Abstract

The PtZn alloy was characterized and studied as a possible candidate for proton exchange membrane fuel cells (PEMFCs). Zn was electrochemically deposited on a bulk Pt substrate and the alloy was spontaneously formed at ambient conditions, as confirmed by Auger electron spectroscopy (AES). PtZn decreased the oxygen reduction reaction (ORR) overpotential by 30 mV with respect to that measured for Pt. The alloy was also prepared in a similar manner on a membrane electrode assembly (MEA) and studied in a single stack fuel cell. The PtZn MEA also showed an improved performance compared to the Pt MEA. Carbon monoxide oxidation catalysis was also investigated. Zn modification of a Pt substrate makes the resulting surface rough, and the roughness was compensated through the measurement of capacitance. Although, in this case, Zn modification did not enhance the catalytic activity compared to Pt, cycling the potential in a CO saturated acidic solution made the PtZn surface smoother and more Pt-rich. The ORR catalytic activity was also compared to Pt with equivalent roughness. PtZn showed enhancement in the kinetics of the reaction, indicating Zn modification had impact on improving the ORR catalytic activity beyond the roughness effect. The PtZn surface becomes Zn-rich after cycling the potential in an oxygen saturated acidic solution. The stability of the alloy under fuel cell operating conditions was also studied. PtZn nanoparticles were formed on glassy carbon substrates and the surface and bulk alloy compositions were determined before and after the alloy was polarized in an oxygen saturated acidic solution. Approximately 18% of Zn originally present in the alloy was lost after 40 hours of polarization at 0.8 V vs. RHE. It was also confirmed PtZn particles adhere well to carbon and were free from sintering effects. The cumulative results presented support that the PtZn alloy is thus a promising candidate for the cathode of PEMFCs.

Table of Contents

List of Tables

List of Figures

List of Symbols And Abbreviations

A	Area
A_{eject}	Area on the surface where Auger electrons are ejected
a	Intercept of a Tafel plot
a_i^{σ}	Activity coefficient of species i in the interface
$a_i^{sol'n}$	Activity coefficient of species i in a bulk solution
α	The transfer coefficient
AES	Auger electron spectroscopy
AFC	Alkaline Fuel Cell
B	Sensitivity factor
b	Slope of a Tafel plot
b_j	The number density of nuclei, j
C_D	Diffuse layer capacitance
C_d	Double layer capacitance
C_H	Inner layer capacitance
C_o^*	Concentration of oxidized species, o, in a bulk solution (in mol/L)
C_R^*	Concentration of reducible species, R, in a bulk solution (in mol/L)
χ	The change in enthalpy of adsorption
χ_i	The change in adsorption enthalpy of species, i, with respect to a coverage
CE	Counter electrode
CN_S	The lattice coordination number of the substrate
CO	Carbon monoxide
CO_{ads}	Adsorbed carbon monoxide
$COOH_{ads}$	Adsorbed formic acid
CV	Cyclic voltammogram

D_0	Diffusion coefficient of species, o
d	Radius of the microelectrode
$d_{0,\,Pt}$	The interatomic bond distance of Pt
$d_{0,\,Zn}$	The interatomic bond distance of Zn
DFT	Density functional theory
ΔE	Energy difference between Pt (1×1) and the hexagonal structure of Pt in the absense of CO
ΔE_{act}	The energy of the activation barrier in the presence of a catalyst
ΔH_{ads}	The enthalpy of adsorption
$\Delta H^o_{formation}$	The standard enthalpy of formation
ΔH_i	The enthalpy of adsorption at a certain coverage
ΔH_{S-M}	The enthalpy of bond formation between the metal and a substrate
$\Delta H_{0,i}$	The enthalpy of adsorption at zero coverage
$\Delta G_0^{\ddagger}$	The standard Gibbs free energy of the activation
δE	Energy difference between Pt (1×1) and the hexagonal structure of Pt in the presence of CO
DMFC	Direct Methanol Fuel Cell
DPV	Differential pulse voltammetry
E	Potential
E_{actual}	The potential applied to the system where the reaction produces net current
E_{anode}	Potential measured at the anode
$E_{cathode}$	Potential measured at the cathode
E_{cell}	Potential of the cell
E_{dep}	Carbon monoxide deposition potential
E_{Nernst}	Nernst (equilibrium) potential
E_p	Peak potential
E_{UPD}	The onset potential of underpotential deposition

E_W	Energy of the core orbital in an atom
E_{WXY}	Energy of an Auger electron
E_X	Energy of the electron in an upper orbital
E_Y	Energy of the electron in a valence orbital
E^o	Standard potential for the half-reaction
E^*	The activation energy of transformation of Pt-hex to Pt (1×1)
EDX	Energy dispersive X-ray spectroscopy
EMIC	1-ethyl- 3- methelimidazolium chloride
e	The charge on the electron; 1.602×10^{-19} C
ε	Dielectric constant of the solution medium
ε_0	Permitivity of free space
F	Faraday's constant; 96485 C/mol
f	Flux of the incident electron beam
f	The lattice mismatch
Φ_e	The work function of an atom
ϕ_2	The electrostatic potential at OHP
fcc	Face centred cubic
GC	Glassy carbon
GDE	Gas diffusion electrode
GDL	Gas diffusion layer
Γ_i	Surface excess concentration of species, i
Γ_{max}	Maximum surface excess concentration
γ	Surface tension
H_{ads}	Hydrogen adsorption
H_{des}	Hydrogen desorption
$HClO_4$	Perchloric acid

hcp	Hexagonal close pack
H_2O_2	Hydrogen peroxide
H_2SO_4	Sulfuric acid
η	Overpotential
I	The intensity contribution to the Auger electrons spectrum
i	Current
i_b	Current generated by a backward reaction
i_f	Current generated by a forward reaction
i_k	Kinetic current
i_l	Mass transfer-limiting current
i_{net}	Net current of a reaction
i_p	Peak current
i_T	The current measured at the SECM tip
$i_{T,\infty}$	The current measured at the SECM tip far from the sample surface
i_0	The exchange current
ICP-MS	Inductively coupled plasma- mass spectrometry
IHP	Inner Helmholtz plane
j	Current density or spin-orbit coupling quantum number
j_0	Exchange current density
K_{CO}	Exchange equilibrium constant for carbon monoxide
K_{eq}	Exchange equilibrium constant
K_{OH}	Exchange equilibrium constant for hydroxyl or an oxygen containing species
k_B	Boltzmann constant; $1.380_6 \times 10^{-23}$ J/K
k_{CO}	Rate constant of CO oxidation reaction
k^0	Standard rate constant
KL	Koutecky Levich
l	Orbital quantum number

λ	Inelastic mean free path
LM_2	The Zn Auger electron spectral peak at the kinetic energy of 990 eV
m	The number of atoms per unit volume of the sample
M	Transition metal
$\bar{\mu}_i$	Electrochemical potential of species, i
MCFC	Molten Carbon Fuel Cell
MEA	Membrane Electrode Assembly
MN_2	The Pt Auger electron spectral peak at the kinetic energy of 2040.8 eV
MN_3	The Pt Auger electron spectral peak at the kinetic energy of 1960.5 eV
N	Total number of adsorption sites on the surface
n	A number of electrons transferred in a redox reaction or the principle quantum number
n_i^σ	Amount of species, i, in the interface
n_j	Coherent neutron scattering length of species j
n_0	The population of an ion in the interfacial region
ν	The kinematic viscosity
NR	Neutron reflectometry
OH_{ads}	Adsorbed hydroxyl or an oxygen containing substance
OHP	Outer Helmholtz plane
ORR	Oxygen Reduction Reaction
p_{CO}	Carbon monoxide pressure
PAFC	Phosphoric Acid Fuel Cell
PEMFC	Proton Exchange Membrane Fuel Cell
Pt/C	Pt particles supported on carbon
Pt-hex	The hexagonal structure of Pt formed on a Pt (100) surface
θ	Surface coverage

θ_{CO}	Carbon monoxide coverage
θ_T	Total surface coverage
θ_{UPD}	The coverage of a UPD layer
$\theta_1 E_1$	Difference in the surface energy of the hexagonal Pt structure with or without the presence of carbon monoxide
$\theta_2 E_2$	Difference in the surface energy of Pt (1×1) with or without the presence of carbon monoxide
R	Gas constant; 8.3144 J/K mol
r	The perpendicular distance from the surface of a rotating disk electrode
ρ	The scattering-length density
RDE	Rotating disk electrode
RE	Reference electrode
RHE	Reversible hydrogen electrode
rpm	Rotation per minute
RRDE	Rotating ring disk electrode
σ	Cross section of the Auger process
S_1	The point at which the current is measured before the potential step is applied in the differential pulse mode
S_2	The point at which the current is measured after the potential step is applied in the differential pulse mode
SECM	Scanning electrochemical microscopy
SEM	Scanning (Secondary) electron microscopy
SHE	Standard hydrogen electrode
S-M	Substrate - metal
SOFC	Solid Oxide Fuel Cell
T	Temperature
T_{trans}	Instrumental constant describing the transmission efficiency of the electron

analyzer

TDS	Thermal desorption spectrometry
UHV	Ultra high vacuum
UPD	Underpotential deposition
WE	Working electrode
ω	The rotational frequency
x_2	The distance from the metal to OHP
y_i^{σ}	Activity coefficient of adsorbed species, i, which also accounts for adsorbate-adsorbate interaction in the interface
z	The parallel distance from the surface of a rotating disk electrode
z_{val}	Valence charge on an ion

Acknowledgments

My graduate school career has been supported by many people whom I just cannot express my gratitude well enough in words. First of all, I would like to thank my supervisor, Dr. Dan Bizzotto, for his guidance throughout the project. What you taught me was not only science but also the positive attitude towards facing challenges, both in research and in everyday life. I also wish I had quarter of your patience and scientific talent.

My project was a continuation of work by former students: Dr. Ed Guerra and Yanguo Yang. Some contents of this thesis were performed by two undergraduate students, Winton Li (supervised by Dr. Elod Gyenge, Department of Chemical Engineering) and Olivia Ye (supervised by Dr. Dan Bizzotto and myself, Department of Chemistry). Without their hard work, there would have been many important questions I would otherwise be unable to understand in my results. I also appreciate having Dr. Philip Wong in UBC Chemistry Department for his thoughtful inputs and for operating Auger electron spectrometer.

Help from technical staff at Department of Chemistry was essential to my research. I am especially thankful to Brian, Des and Raz in mechanical shop not only for machining equipment for my setups but also for keeping me entertained with their conversations. I also thank Brian Ditchburn in glass shop for making electrochemical cells and the glass accessories.

I would also like to acknowledge my colleagues in the lab: Dr. Emily Chung, Yanguo Yang, Dr. Jeff Shepherd, Dr. Robin Stoodley, Jannú Casanova Moreno, and Amanda Musgrove (Richer); for their constant help, friendship, useful discussion, and entertainment. I would especially like to thank Robin for his friendship. It was pleasure to work with you, and I wish I had your patience for problem-solving.

My friends have always provided me comfort and a little break from non-working experiments. I would especially like to acknowledge Ms. Chika Watanabe and Dr. Tak Ikeda for their constant mental support and for sharing their thoughts with me.

Finally, I would like to send my special thanks to Jannú for his constant encouragement. Gracias por estar conmigo. Disfruto tu compañía y te quiero.

1. Introduction

Alternative energy resources that are free from the limited supply and the emission of toxic or greenhouse gases are in high demand in response to the current oil and climate crises. Whether it would be solar power, wind power, or hydro power, it does not necessarily replace fossil fuels or coal instantly, but certainly need to be available as the equivalent options to fossil fuels, and the community needs to adapt to more environmentally benign options quickly.

One of such alternatives is a fuel cell, which is an electrochemical power supply device which converts chemical energy directly into an electrical energy at potentially high efficiency. There are several kinds of fuel cells, as shown in **Table 1-1**, and depending on their operating characteristics (*i.e.*, operation temperature, types of fuels *etc*), fuel cells can be used in a wide range of applications, including small portable devices, an automobile, or in a power plant. In this thesis, the focus will be on proton exchange membrane fuel cells (PEMFCs), which utilize air (oxygen) as an oxidant and hydrogen or a low-molecular weight alcohol as a fuel. The diagram of a PEMFC is shown in **Figure 1-1**. Energy conversion occurs in the membrane electrode assembly (MEA), which consists of an acidic solid electrolyte membrane separating a cathode on one side and an anode on the other side. At the anode, hydrogen gas or an alcohol, such as methanol, is oxidized to form protons:

$$H_2 \rightleftarrows 2H^+ + 2e^- \qquad E^o = 0.0 \text{ V vs. SHE} \qquad\qquad (1\text{-}1)$$

$$H_2O + CH_3OH \rightleftarrows CO_2 + 6H^+ + 6e^- \qquad E^o = 0.04 \text{ V vs. SHE} \qquad (1\text{-}2)$$
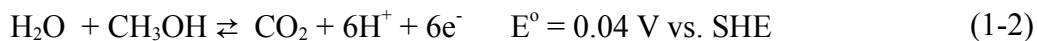
Electrons go through the external circuit as an electrical current available for generating useful work, and protons migrate to the cathode through the solid electrolyte. Oxygen is converted to water at the cathode with these protons:

$$O_2 + 4H^+ + 4e^- \rightleftarrows 2H_2O \qquad E^o = 1.23 \text{ V vs. SHE} \qquad\qquad (1\text{-}3)$$
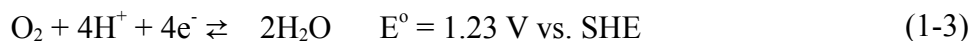
This reaction is called an oxygen reduction reaction (ORR). The power output of fuel cells is calculated by multiplying the potential difference between the cathode and anode (E_{cell}) at the corresponding current, *i*:

$$Power = E_{cell} \times i \tag{1-4}$$

The practical energy conversion efficiency of fuel cells are much higher than that of heat engines as they operate at a much lower temperature, and the heat rejection process is much less severe. In theory, the efficiencies of a PEMFC could be as high as 94.5 % [1]. In reality, fuel cells do lose energy to heat and the practical efficiency becomes ~65 % which is still more efficient than *e.g.,* gas and steam turbines whose conversion efficiency is ~33% [2].

Although the MEA may be considered the heart of fuel cells, there are numerous components or conditions that affect the performance of fuel cells. For example, the solid electrolyte must be fully humidified in order to carry protons from the anode to the cathode. However, water formed at the cathode also needs to exit the system to avoid flooding. Plates are placed on each side of MEA, called *flow field plates.* They are responsible for exhausting the water, among other tasks, such as distribution of reactants into MEAs, carry current away from cells, and cool down MEAs [2]. Manufacturing reliable flow field plates is challenging in order to satisfy all demands. Failure to do one or more of the tasks may drastically decrease the performance of the cell, and one must know the physical and chemical properties of materials used, the method of fabrication, and optimum operational conditions for a fuel cell to satisfy the energy demand. Therefore the fuel cell development requires expertise not only in electrochmistry, but also in material science, polymer science, mechanical engineering, fluid dynamics, and computational modeling, just to name a few. Fuel production is also another challenging research. Although the focus of this thesis is in the field of electrochemistry, it should be emphasized that fuel cell research is very interdisciplinary, and the contribution from all fields of science is the key to the prompt development of commercially viable fuel cells [2].

Table 1-1 Types of fuel cells and their characteristics [3]

Types of fuel cells	Ions exchanged in electrolyte	Operating temperature (^{o}C)	Chemical – electrical conversion efficiency (%)	Applications
Alkaline fuel cell (AFC)	OH^{-}	60-80	40-60	Automobiles, space shuttles
Phosphoric acid fuel cell (PAFC)	H^{+}	200	55	Generation of distributed power
Proton exchange membrane fuel cell (PEMFC)	H^{+}	80	45-60	Portable devices, automobiles
Molten carbon fuel cell (MCFC)	CO_3^{2-}	600	60-65	Distributed power generation
Solid oxide fuel cell (SOFC)	O^{2-}	1000	55-65	Base load power generation
Direct methanol fuel cell (DMFC)	H^{+}	80	35	Portable devices, automobiles
Heat engines		1000	~33	Steam and gas turbines
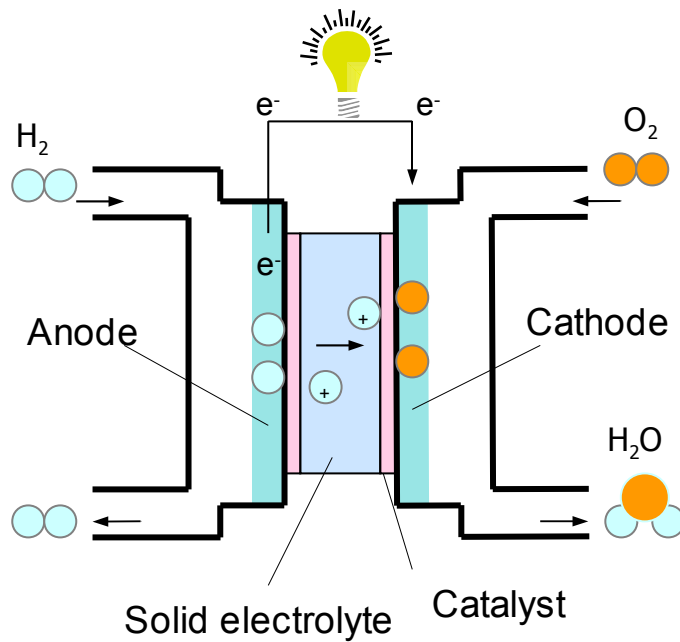
Figure 1-1 The diagram of a PEM fuel cell with hydrogen as the fuel. Hydrogen molecules are oxidized at the anode and oxygen molecules are reduced to water at the cathode. Electrons go through the external circuit to generate electricity. The anode, the solid electrolyte, and the cathode layers are the parts of a membrane electrode assembly (MEA).

1.1. Electrochemical reactions at the electrode

Reactions producing electricity in low temperature MEAs are kinetically slow and require the presence of catalysts. Currently, the most common catalyst is Pt. The amount of precious metals used in fuel cells has been drastically reduced over years, but such precious metals are expensive (currently 992 USD/oz or 15,872 USD/lb) [4] and, more problematically, rare. Dependence on precious metals alone as fuel cell catalysts will eventually lead to a similar catastrophe as fossil fuels are currently causing. Learning from the current situation, it is wise to look for alternative catalysts while the utilization of fuel cells is still low. Another challenge with

4

the fuel cell reactions is that the mechanisms of the reactions are not fully understood despite the decades of research effort. Knowledge of the active sites would be very useful when developing a catalyst, and the mechanistic research is actively pursued around the world.

An alternative catalyst to Pt is a Pt-based alloy using the first row of transition metals. They have actually been shown to improve the reaction rates significantly. At the same time, however, they are not very stable under acidic conditions. Also, those alloys are often Pt-rich in composition and therefore still requires a substantial amount of Pt. Stable Pt-alloys that maintain an improved catalytic activity over time is a key technological step towards fuel cell distribution for practical applications.

In this work, we examined a PtZn alloy as a possible candidate for an electrocatalyst for fuel cell reactions. There are three themes to the thesis: 1) electrochemical formation of PtZn and comparing its catalytic activity to that of pure Pt; 2) changes in surface characteristics before and after performing the reactions on the catalysts using electron spectroscopy; and 3) investigating the stability of PtZn under fuel cell operational conditions. The project has been initially started by previous students: Dr. Eduard Guerra first studied the Zn electrodeposition using Pt substrates in 2003. Together with Dr. Guerra, Mr. Yanguo Yang found that the PtZn alloy may be a possible candidate for ORR. Back then, and even now, there are numerous Pt-based alloys that showed an improved catalytic activity for fuel cell reactions, but PtZn had never been considered for the use in fuel cells, except the one reported by He *et. al.,* in 2007 [5] probably because of the susceptible nature of metallic Zn in an acidic condition. Our results, however, did not seem to show a significant issue with the stability of Zn in the PtZn alloy, which makes the work described in this thesis unique and potentially significant when compared to the other Pt-based alloys in literature or those already in use. Usage of Zn as an alloying metal is also advantageous over other popular alloying metal, such as Ni, because Zn is relatively inexpensive and abundantly available on the earth. The market price on Zn is 0.753 USD/lb; more than 9 times cheaper than Ni; 6.964 USD/lb [6]. Replacing even 30% of Pt by Zn could lower the cost for catalysts dramatically.

The second theme, surface characterizations of the catalyst, is important for understanding the mechanisms of fuel cell reactions. Because catalysis happens at the surface (*i.e.,* metal/solution interface), and the characteristics of the metal surface are often quite

different from the bulk, tracking the state of the surface becomes crucial to understanding the reaction pathways. We were able to trace the changes in the surface of PtZn by electrochemistry and with further support using ex-situ electron spectroscopy.

The third theme, the stability of the PtZn alloy, is crucial in a practical fuel cell application. One of the challenges researchers have faced when using Pt-based alloys in a fuel cell is the leaching of alloying metal into the solid electrolyte. One obvious reason this is not favorable is because protons migrate from the anode to the cathode by an ion exchange process through the solid electrolyte. The leached metal ions will occupy the sites necessary for proton movement which will decrease the performance of the fuel cells. Stability of these Pt-alloy catalysts is therefore extremely important in the fuel cell development. A stability examination method that is unique to the current literature has been proposed and studied. Combining the three themes and the results of the research presented in this thesis, PtZn appears to be a reasonable candidate for use in a PEMFC.

1.2. Outline of the thesis

Chapter 2 provides a literature review of the current understanding of fuel cell reaction catalysis on Pt and Pt-based alloys. It also reviews the previous experimental and theoretical studies on a PtZn alloy, which suggests that it may be a promising candidate as a fuel cell catalyst.

Chapter 3 describes experimental techniques used in this research. The work presented in this thesis employed some basic electrochemical techniques, as well as analytical methods for characterizing the chemical compositions of a sample surface or sample solutions.

Chapter 4 describes the electrochemical formation of PtZn alloy and its surface characterization with Auger electron spectroscopy (AES). We then compare the catalytic activities of Pt and PtZn for the ORR in an electrochemical setup. Kinetic data was deduced from the measurements. Results presented in this chapter show that PtZn is an effective catalyst candidate for ORR, one of the most sluggish fuel cell reactions. We also employed our PtZn in a single stack fuel cell and compared the performance to a Pt fuel cell. The PtZn alloy was also

prepared electrochemically directly onto a catalyst coated gas diffusion electrode. It was then pressed with the membrane and an anode to make a fuel cell. The performance was again compared to Pt fuel cell tested under identical conditions. The results obtained were essentially the same as the one we obtained in the first section of this chapter, *i.e.,* the PtZn fuel cell showed an improved performance compared to the Pt fuel cell. The bulk of the work described in this chapter has been published in *Journal of Physical Chemistry B* [7].

Chapter 5 reports on another catalytic reaction, carbon monoxide (CO) oxidation which is the rate determining step for the methanol oxidation, on Pt and PtZn. The surface roughness effects on the catalytic activities of fuel cell reactions were also examined. Although we were not able to prove PtZn improves the activity of the reaction, we observed changes in surface compositions of the metal alloy. Depending on the molecules that are adsorbed on the alloy surface, the surface became enriched with one of the alloy components. The surface also became smoother as CO was adsorbed onto the metal surfaces, and these observations were made through simple voltammetry. The work presented in this chapter was published in *Electrochimica Acta* [8].

Chapter 6 reports a new methodology to test the chemical stability of alloy metals and the results thus obtained. Previous to the new method, we had attempted two stability tests of PtZn in different methods, and the results are also presented. In the new method proposed, PtZn nanoparticles were first formed on glassy carbon substrates. A fixed potential was applied to the substrate under a condition similar to an operating fuel cell. The particle surface was then analyzed using ex-situ AES. The particle bulk composition were further analyzed using inductively-coupled plasma – mass spectrometry. This method shows the surface composition of the PtZn alloy in relation to its bulk composition.

Finally, the summary and conclusions are given in **Chapter 7** reviewing the results given in different sections of the thesis. Suggestions for the future work are also presented.

2. Literature Review

2.1. Introduction

This chapter has two main themes: The first is to review the current understanding of PEM fuel cell reaction catalysis and background theories of electrochemistry and heterogeneous catalysis. Two reactions are considered: Oxygen reduction reaction (ORR) and CO oxidation. The mechanisms of these reactions on a Pt surface on Pt-based alloys are summarized. The second theme is to review the characteristics of PtZn alloy. The formation of this alloy is facilitated by so-called an underpotential deposition (UPD) layer of Zn over the Pt surface. This alloy also exhibits characteristics distinct from its components. Alloying effects on Pt or Zn in PtZn are also compared to other alloys.

2.2. Proton exchange membrane fuel cell

2.2.1. Membrane electrode assembly

Proton exchange membrane fuel cells (PEMFCs) used in practical applications consist of a number of single stack cells connected in series. Typically passenger vehicles require ~100 kW power output and the power density of fuel cells are ~2.5 kW/L. A single stack fuel cell consists of a proton-conducting polymer (or solid electrolyte), sandwiched by two catalyst layers supported on carbon black. This sandwich unit is the membrane-electrode assembly (MEA), which essentially acts like an electrochemical cell. The solid electrolyte is an ionomer; *i.e.,* a polymer with a backbone containing ionizable functional groups attached at the end of the chains. For example, the most commonly used solid electrolyte is Nafion™ whose structure is shown in **Figure 2-1** [2]. Nafion™ consists of fluorinated carbon backbone with sulfonic acid attached at the end of the chains. When solid membranes are hydrated, the functional group ionizes and the counter ions (protons this case) will be readily replaced by incoming ions of the

same charge.

On the catalyst layers of the MEA (refer to **Figure 1-1**), either the hydrogen gas or a liquid methanol is fed as a fuel on the anode side. A PEMFC consuming the latter fuel is called a direct methanol fuel cell (DMFC). Protons are produced with either of the fuels, and they migrate through the electrolyte to the cathode side of the MEA, where the ORR takes place. For this reason, it is essential that the membrane is fully hydrated, and also the incoming gaseous fuel or oxidant is humidified. The most commonly employed catalyst material is Pt nanoparticles (~3 nm) dispersed on a carbon support for both anode and cathode in low-temperature PEMFCs because they catalyze the reactions reasonably well. The chemical stability of Pt is benign in rather severe fuel cell operating conditions, and Pt can be recycled. For these reasons, reaction catalysis is extensively studied on Pt as a benchmark for other catalyst candidates being developed or to help researchers understand the reaction mechanisms. The studies of catalysis on a Pt surface will be reviewed after describing the basic thermodynamics and kinetics of the electrode reactions.

Figure 2-1 Structure of Nafion™. Fluorinated carbon chains with sulfonic acid terminals. When Nafion is hydrated, sulfonic acid becomes ionized, and the protons will be involved in the ion exchange process [2].
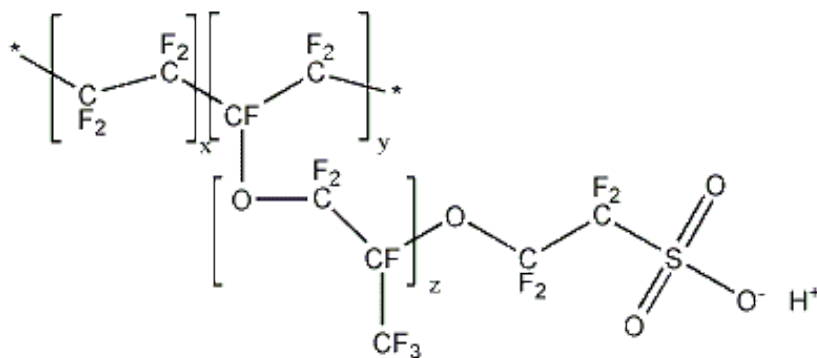
2.3. Electrochemistry

Electrochemistry is the study of the interactions of ions or molecules either among themselves or with the electrode material (*i.e.*, metal) under an applied electric field. Because fuel cells are electrochemical devices, understanding the fundamental theories of electrochemistry is essential in fuel cell research, especially in electrocatalysis – the focus of this thesis.

This section reviews the theories of electrochemistry, covering the structure of the double layer and the theory of electron transfer. The interfacial region is where adsorption of molecules and electron transfer take place, and is best described by the double layer theory. Electron transfer kinetics is explained in relation to the observed current-potential relationship.

2.3.1. Metal/liquid interface and electrical double layer

An interface is formed when two distinct media come into contact (*e.g.,* liquid/solid, solid/gas). Assuming a metal (electrode) is in contact with a solution containing ionic species, and a potential difference (with respect to a reference or ground) is applied to the electrode, there are potential ranges where no redox reaction occurs at the metal/solution interface. Under such a circumstance, the electrode is said to be *ideally polarized* and only charging current flows. In this particular case, the interface is called an electrical double layer and acts as a capacitor. It is important to note that the amount of charge residing on the metal side of the interface is counterbalanced by the amount of charge lining on the solution side of the interface.

The structure of the double layer is described by the Gouy-Chapman-Stern model. Gouy-Chapman-Stern model considers the liquid/solid interface as two capacitors in series. The first "capacitor" extends from the metal surface into the solution to an imaginary plane, called the Helmholtz plane. The second capacitor extends from the Helmholtz plane to the bulk solution, and is called the diffuse layer. This is illustrated in **Figure 2-2**. The capacitance of the double layer or *differential capacitance,* C_d, of the interface can be described by,

$$\frac{1}{C_d} = \frac{1}{C_H} + \frac{1}{C_D}$$

(2-1)

where C_H is the capacitance in the inner layer, and C_D is the capacitance of a diffuse layer.

The inner layer can further be divided into two planes, known as Inner Helmholtz plane (IHP) and outer Helmholtz plane (OHP), illustrated in **Figure 2-3**. At the IHP, either water molecules lined up by pointing their dipole moments against the charged metal surface or specifically adsorbed ions are found. Solvated ions close to the surface of the metal are found at the OHP. Since the charge accumulated in the vicinity to the metal surface lie along the OHP, the metal/solution interface up to the OHP acts as a simple capacitor (which is represented as a C_H). Assuming no specific adsorption, the potential across the inner layer decreases linearly as no charged species are found in that region, and the potential in diffuse layer decays as a sinh function. The differential capacitance can be expressed as

$$\frac{1}{C_d} = \frac{x_2}{(\epsilon \epsilon_0)} + \frac{1}{(2\epsilon \epsilon_0 z_{val}^2 e^2 n^0 / k_B T)^{1/2} \cosh(z_{val} e \phi_2 / 2 k_B T)}$$

(2-2)

where x_2 is the distance from the metal to the OHP, ϵ is the dielectric constant of the medium, ϵ_0 is permitivity of free space, z_{val} is the valence on the ions in the solution, e is the charge on electron (1.602×10^{-19} C), n_0 is the total number of an ion in the interfacial region, k_B is Boltzmann constant, T is the temperature, and ϕ_2 is the electrostatic potential at the OHP. Noting the first term corresponds to C_H, and the second to C_D, this equation shows that the C_H is independent of potential, whereas that of the diffuse layer is dependent on potential. C_d is dominated by the smaller of the two effective capacitors in series.
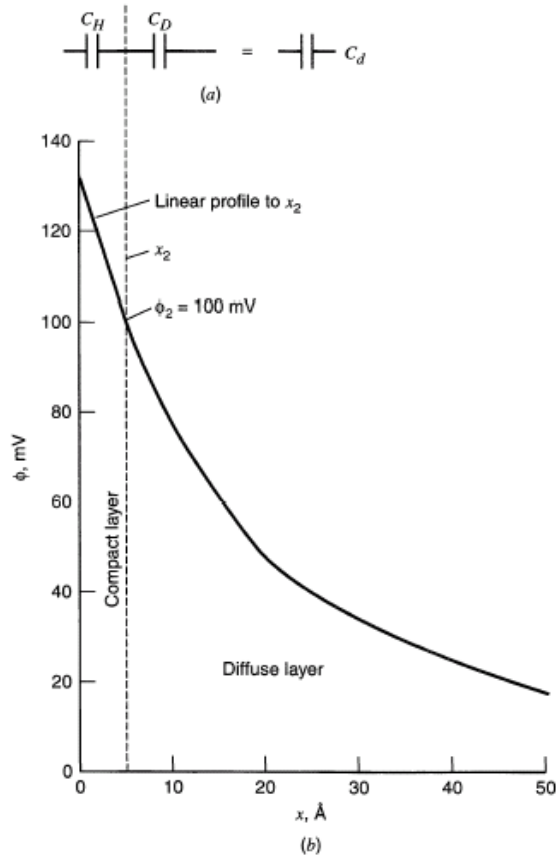
Figure 2-2 The double layer structure based on Gouy-Chapman-Stern model. The double layer capacitance, C_d, is considered as two capacitors in series, a capacitor at the inner layer and the diffuse layer capacitor; C_H and C_D, respectively. The figure shows the potential drop across the double layer, calculated for a 0.01 M 1:1 electrolyte at 298 K, assuming a potential of 100 mV at the Outer Helmholtz Plane. The compact layer is an alternative name for the inner layer. Reproduced with permission from [9]. Copyright 2001 John Wiley & Sons Ltd.
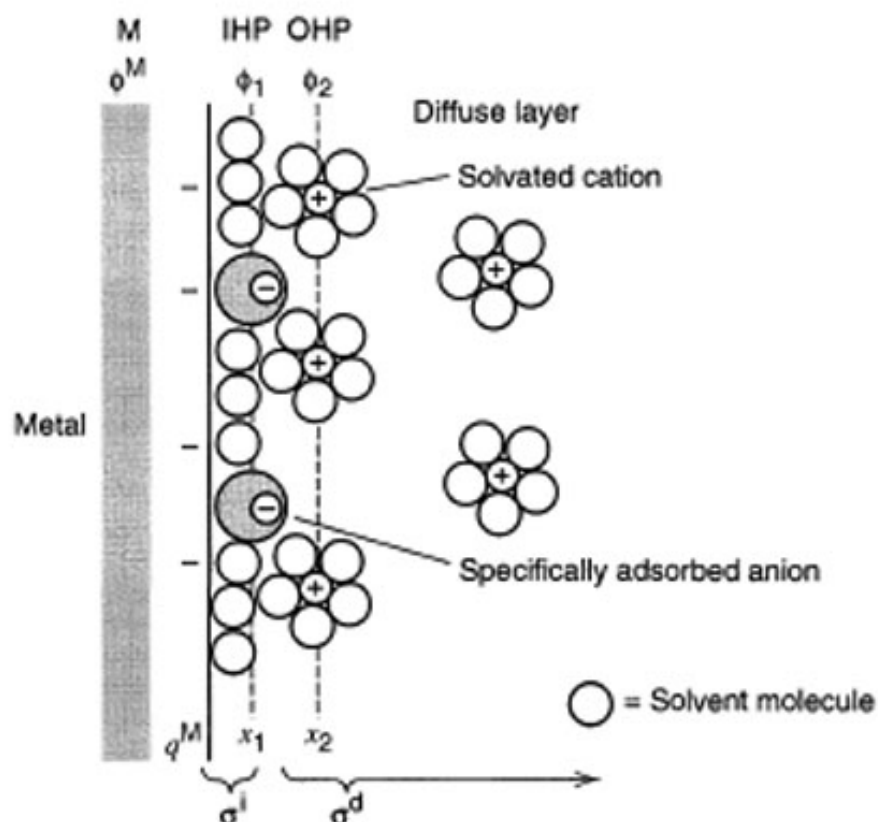
Figure 2-3 Double layer structure of metal/solution interface. The line at x_1 is inner-Helmholtz plane (IHP) and the line at x_2 is the outer-Helmholtz plane (OHP). Only water and specifically adsorbed ions are found at IHP, and ions can only reach to the OHP in solvated form. Reproduced in part with permission from [9]. Copyright 2001 John Wiley & Sons, Ltd.

Specific adsorption of ions (*e.g.,* SO_4^{2-} on Pt) may vary the potential gradient within the Helmholtz plane. Adsorbing ions with charge opposite to that on the electrode causes an increase in the gradient, while like charges result in a decrease [9].

2.3.2. Metal side of interface: surface dipole

The previous sections described the charge distributions in the solution side of the metal/ solution interface. The metal side of interface is the focus next.

The electron density profile with respect to distance from the metal surface is shown in **Figure 2-4** [10]. The electron density close to the surface (*i.e.,* distance = 0) is not confined to the surface, but is spread out into vacuum. This redistribution of charge over the surface is called *surface dipole* and assists to lower the surface energy of the metal. It also lowers the metal's *work function*. Work function is the minimum energy required to remove an electron from the Fermi level into vacuum [11]. The extent of the surface dipole increases with temperature and also with the roughness of the metal surface. Because of the electron spillage, the average work function on a rough surface is smaller than on a smoother surface [11].
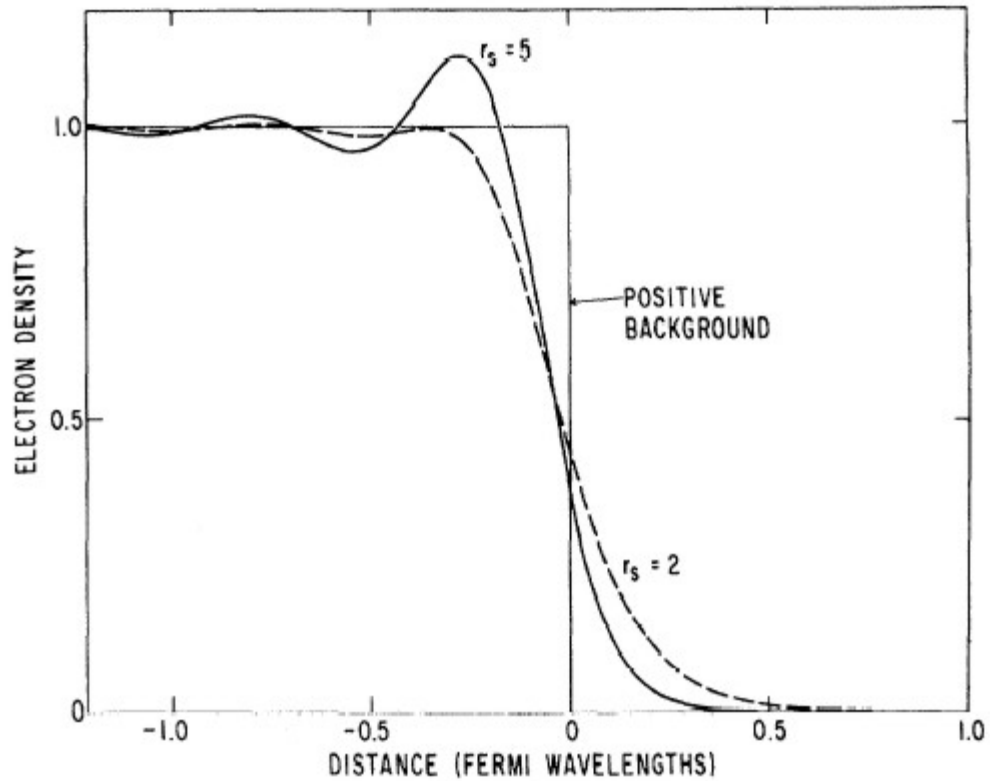
Figure 2-4 Electron density at a metal surface. Electrons "spill over" at the metal surface showing the deficit in the electron density below the Fermi level, creating the net surface dipole. Distance is shown in Fermi wavelength, which is direction- and element-dependent but is approximately 0.5 nm. Reprinted with permission from [10]. Copyright 1970 by American Physical Society. http://prola.aps.org/abstract/PRB/v1/i12/p4555_1

2.4. Thermodynamics and kinetics of electrode reactions

Thermodynamics and kinetics of electrode reactions, whether in an electrochemical cell or in a fuel cell, can be treated similarly. This section reviews basic electrochemistry relating potential (or "overpotential") and current.

2.4.1. Fuel cell power output

Power output of fuel cells is calculated as,

$$\text{Power} = \text{E}_{cell} \times i \tag{2-3}$$

where E_{cell} is defined as the difference between the potential of cathode and anode, $E_{cell} = E_{cathode} - E_{anode}$, at a particular current, i. The current can be substituted by the *current density, j,* which is the current normalized for the surface area of the catalyst. Theoretically $\text{E}_{cathode}$ and E_{anode} can be predicted by the Nernst equation,

$$E_{Nernst} = E^0 + \frac{RT}{nF} \ln \frac{C_O^*}{C_R^*} \quad \text{(For a cathodic reaction; Ox + ne}^- \rightleftarrows \text{Red)} \tag{2-4}$$

E_{Nernst} is the potential of the cell, E^0 is the standard potential of the redox reaction, R is the gas constant (8.3144 J/K mol), T is the temperature, F is Faraday's constant (96485 C/mol), n is the number of electrons involved in the electron transfer, and C^* is the bulk concentrations of species, and Ox and Red which stand for oxidized and reduced forms of the species, respectively. The Nernst equation relates potential to concentrations in the electrolyte at thermodynamic equilibrium. In an electrochemical cell, however, reaction equilibrium may or may not be realized depending on the conditions. For example, the rates of reactions are very much dependent on the applied potential. Also, the theoretical equilibrium potential for the ORR is 1.23 V vs. SHE, but if Pt is used as a catalyst, an oxide film would form at potentials higher than 0.85 V vs. SHE in an acidic condition. The presence of oxide on the surface would interfere with the ORR reaction pathway, decreasing the current as compared to the oxide-free Pt surface

at the same applied conditions.

2.4.2. Current-potential relationship in kinetics

2.4.2.1. Overpotential

When forward and backward reactions have considerably different rates, the reaction is said to be irreversible. The extent of irreversibility is often expressed by the *overpotential* (or *polarization*), η:

$$\eta = E_{actual} - E_{Nernst} \tag{2-5}$$

E_{actual} is the potential where the reaction produces net current, therefore overpotential is the extra potential needed to drive the reaction at a certain rate in addition to the Nernst potential [9]. There are three mechanisms contributing to overpotentials: 1) activation overpotential; 2) ohmic overpotential; and 3) concentration overpotential. Activation overpotential is due to the slow kinetics of the chemical reactions at an anode or a cathode, ohmic overpotential arises due to electrical resistance in the cell, and concentration overpotential is due to mass transfer limitation. These are illustrated in **Figure 2-5** [9]. Ideally, the potential-current relation shows a straight horizontal line, shown at the top of the figure; however, potential constantly drops with increasing current due to one or more types of overpotentials.
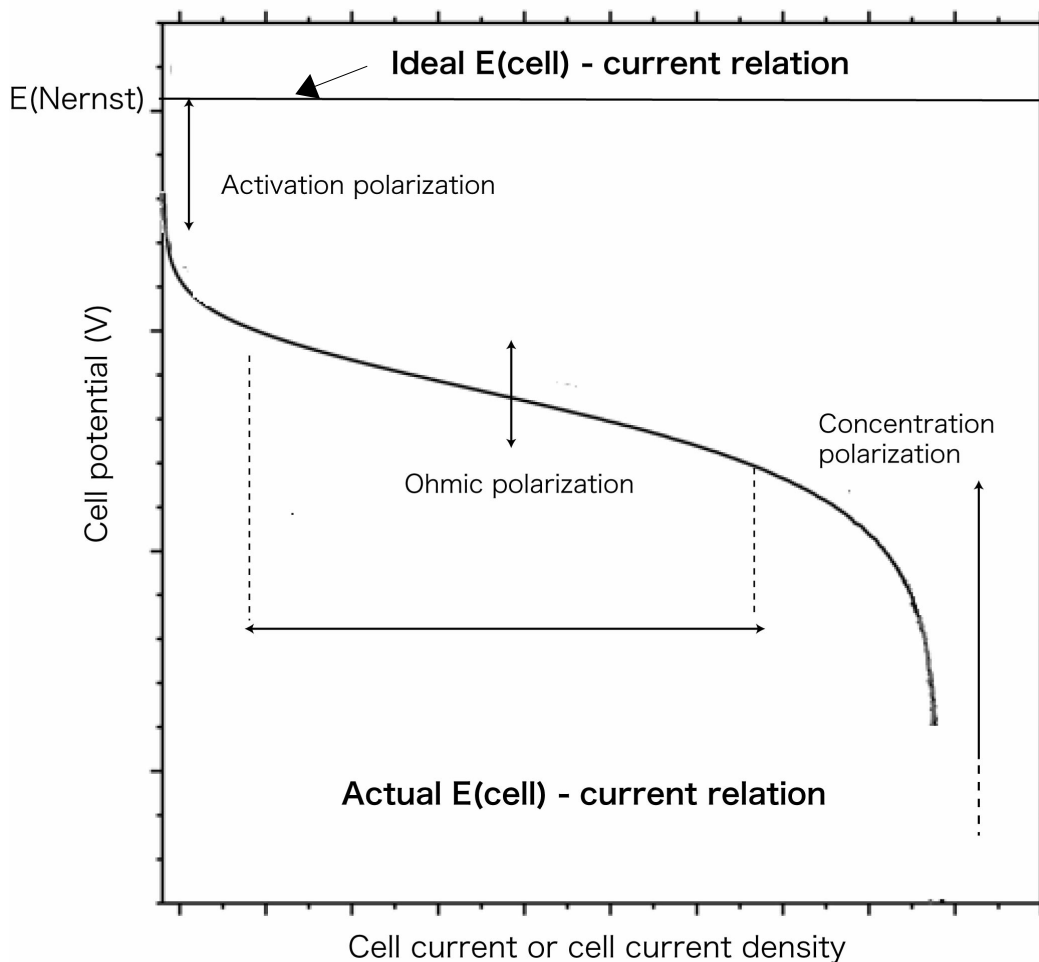
Figure 2-5 A polarization curve showing the three mechanisms of overpotential observed in a fuel cell. The integral of the curve is essentially the power output from the fuel cell. The theoretical potential of the cell is calculated by the Nernst equation, and the potential is ideally constant regardless the current flow. However, the potential is lost in overcoming the reaction irreversibility (activation polarization), the internal electrical resistance (ohmic polarization), and the reactant mass-transfer limitation to the catalyst surface (concentration polarization).

2.4.2.2. Current-overpotential relationship

The net current flow is simply the difference between forward and backward reaction current (i_f and i_b, respectively), and it is important to derive the equation relating potential (or overpotential) to the net current flow. Transition state theory is used in the derivation, which is detailed in [9]. For a one electron-transfer reaction with the transition state in forward and backward directions shown in **Figure 2-6.** The net current, i_{net}, which is a measure of the reaction rate, at a particular overpotential is calculated using the following equation, called the Butler-Volmer equation [12]:

$$i_{net} = i_f - i_b = i_0 \left[\exp\left(\frac{\alpha F \eta}{RT} \right) - \exp\left(\frac{-(1-\alpha) F \eta}{RT} \right) \right] \tag{2-6}$$

The term α is a transfer coefficient; a term related to the symmetry of the activation barrier to the reaction. The notations F, R, and T are the same as the ones used for the Nernst equation. The term, i_o, is called the exchange current, which is the current at dynamic equilibrium flowing in both forward and backward directions (so the net current is zero). The exchange current is proportional to the standard rate constant (k^0) of the reaction,

$$i_0 = FAk^0 C_o^{*(1-\alpha)} C_R^{*\alpha} \tag{2-7}$$

where A is an area of the electrode material. The exchange current is therefore a good measure of the intrinsic facility of the reaction [9].

When the overpotential for the forward reaction is large (*i.e.,* $|\eta| > 118$ mV), the contribution to the net current or current density from the backward reaction is minimal, hence the second term in Butler-Volmer expression can be neglected. Solving for overpotential, the equation becomes,

$$\eta = a + b \, \log(j) \tag{2-8}$$

where a = [(2.3RT/αF)*log j_0], b = -2.3RT/αF, and j is the current density, which is the area normalized current. This expression is known as the Tafel equation. Tafel plot is an important diagnostic tool for determining thermodynamic parameters, *i.e.,* α and j_0, deduced by plotting η

(or E) against log j, assuming reaction mechanism does not change within the range of extrapolation [9].

The presence of a catalyst is required for most of the fuel cell reactions. A catalyst is defined as a substance that increases the rate of a chemical reaction without being a part of its end products [13]. Most of the fuel cell reactions fall into the category of heterogeneous catalysis, *i.e.*, a catalytic process with the reacting molecules and the catalyst in the different phases (*e.g.*, gas phase molecules reacting on a solid catalyst). The concept of heterogeneous catalysis is described next. Because catalytic processes are sensitive to surface structures, a lot of work elucidating reaction mechanisms has been performed on Pt single crystals of low-Miller indices, as Pt is so far the best fuel cell catalyst. The structures of the crystals are also shown.
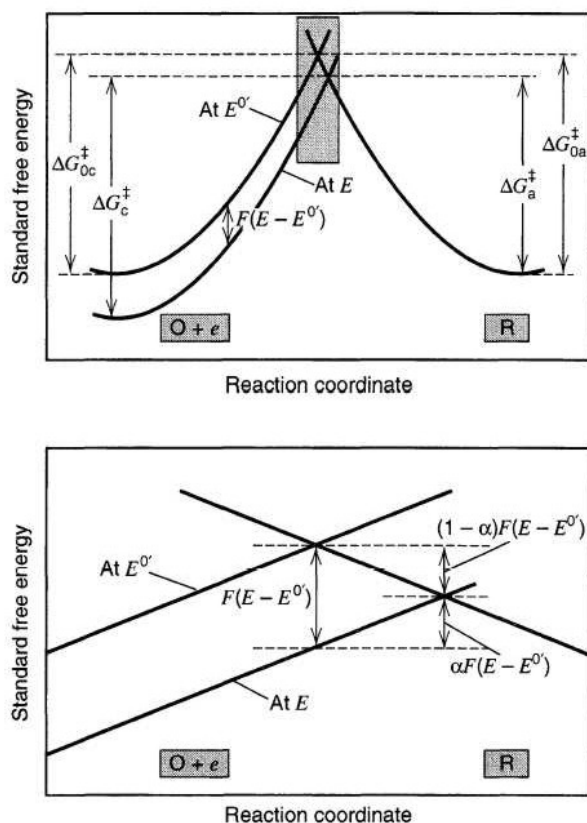
Figure 2-6 The transition state of the forward and backward reactions. $\Delta G_0^{\ddagger}$ shows the standard Gibbs energy of the reaction at the equilibrium potential. When a potential is applied externally, the potential curve shifts, as shown in the top figure. The transfer coefficients, α for the forward reaction or $(1-\alpha)$ for the reverse reaction, describes the contribution to the net current from either side of the reaction. Reproduced with permission from [9]. Copyright 2001 John Wiley & Sons Ltd.

2.4.3. Heterogeneous catalysis

Fuel cell catalysis or electrocatalysis is heterogeneous catalysis involving a metal surface interacting with the solvated gas molecules. The concept of catalysis is to increase the reaction kinetics by lowering the activation energy of the reaction that would otherwise be sluggish. This is achieved by adsorption of the reactant molecules onto the catalyst surface. Surface of solids generally are unsaturated (*i.e.,* have fewer neighboring atoms than the bulk), thereby the molecules in a gas phase can chemisorb onto the surface atoms. This process leads to weakening or even breaking the chemical bonds of the adsorbed molecules, which is called a dissociative chemisorption [11]. **Figure 2-7** shows the Lennard-Jones energy diagram for such a process for a molecule, A_2. The difference between the two potential curves is the energy of dissociation of the molecules (designated as E_{diss}). ΔE_{act} is the activation barrier that the molecules need to overcome in the presence of catalyst. The adsorption energy of the molecule is denoted as ΔH_{ads} in the diagram. Because ΔE_{act} is smaller than ΔH_{ads}, A_2 is stabilized on the surface while the dissociation of A-A bonds occurs [11].
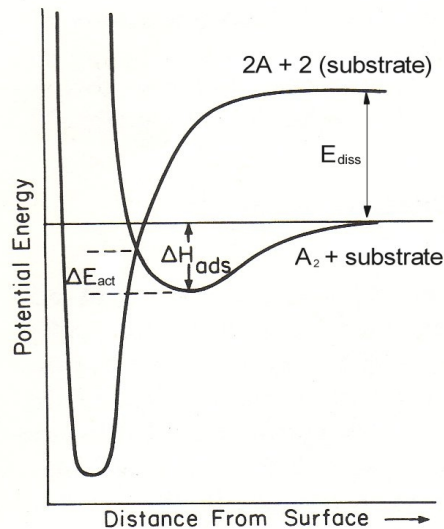
Figure 2-7 Energy diagram showing the dissociative chemisorption process in heterogeneous catalysis. The adsorption energy of A onto a site on a substrate is lowered to ΔE_{act} by the presence of catalyst. Adapted from [14].

The activation energy of any reaction is calculated using Arrhenius equation, including the electrocatalytic reaction [15]:

$$\frac{d(\log i_0)}{d(1/T)} = \frac{\Delta E_{act}}{2.3RT}$$

(2-9)

Adsorption of molecules onto the catalyst surface, particularly onto the electrode surface (*i.e.,* metal/solution interface) is governed by the Gibbs adsorption isotherm:

$$-d\gamma = \sum_i \Gamma_i d\bar{\mu}_i$$

(2-10)

The term, γ is the surface tension which is the energy required to create a new surface with an area A, and $\bar{\mu}_i$ is the electrochemical potential. Γ_i is the surface excess concentration, defined as the amount of species i in the interface (denoted as n_i^{σ}; σ is used to represent the interface) per area A [9]:

$$\Gamma_i = \frac{n_i^{\sigma}}{A}$$

(2-11)

Surface excess can also be expressed as exchange equilibrium of i in the interface and the solution (in terms of their activities, a) with the equilibrium constant, K_{eq} [16]:

$$\Gamma_i = K_{eq} \frac{a_i^{sol'n}}{y_i^{\sigma}} \qquad K_{eq} = \frac{a_i^{\sigma}}{a_i^{sol'n}}$$

(2-12)

The term y_i^{σ} is the activity coefficient of the adsorbed species and accounts for the adsorbate-adsorbate interactions in the interface. The mode of adsorption can be described by the term y^{σ}, and it can be determined by fitting experimental data to the theoretical isotherms. For example, in the case of a Langmuir adsorption isotherm, where adsorbed particles of finite size are independent of one another, the adsorption isotherm becomes,

$$\frac{\Gamma_i}{\Gamma_{max} - \Gamma_i} = K_{eq} a_i^{sol'n}$$

(2-13)

where Γ_{max} is the maximum amount of i possibly adsorbed onto the surface per area (*i.e.,* saturation) [17]. Elucidation of adsorption isotherm in electrocatalysis is not straightforward as adsorbate-adsorbate interactions and/or the adsorption energy of molecules may be influenced

by the presence and the strength of electric field. On the other hand, understanding adsorption isotherms is critical for reaction mechanism studies, and this is still a challenge in fuel cell research.

2.5. Platinum

2.5.1. Low Miller index Pt single crystals

The crystal structure of bulk Pt is face centred cubic (fcc), but depending how the surface is made by exposing various Miller index planes, the surface energies will vary. **Figure 2-8** shows three different principle Pt crystal faces, namely (100), (110) and (111). Pt (111) surface is the most densely packed surface among the three single crystals, followed by (100) and (110). The surface energies of those surfaces are closely related to the packing density of the crystal faces [11] as shown in the previous section. A larger surface dipole is induced by a rougher surface (see **Figure 2-4**), which tends to lower the work function. Because catalytic processes require adsorption of molecules on the surface, and a rougher surface tends to offer more adsorption sites, it is generally true that catalytic activity is better on a rougher surface.

Polycrystalline Pt is a surface of Pt containing two or more single crystal faces separated by grain boundaries, thereby providing an average characteristics of those three low-index single crystals. For example, the charge due to the adsorption of hydrogen on Pt (111), (110), and (100) are 255 $\mu C/cm^2$, 220 $\mu C/cm^2$, and 205 $\mu C/cm^2$, respectively [18, 19], whereas the one for polycrystalline Pt is 210 $\mu C/cm^2$ [20]. Polycrystalline Pt is also commonly used to study catalysis.

The first reaction of interest on the Pt surface is ORR – the cathodic reaction in PEMFCs.
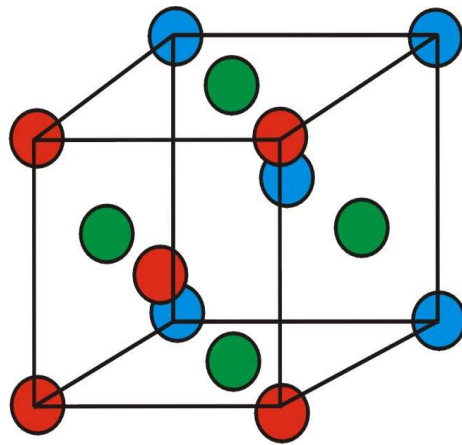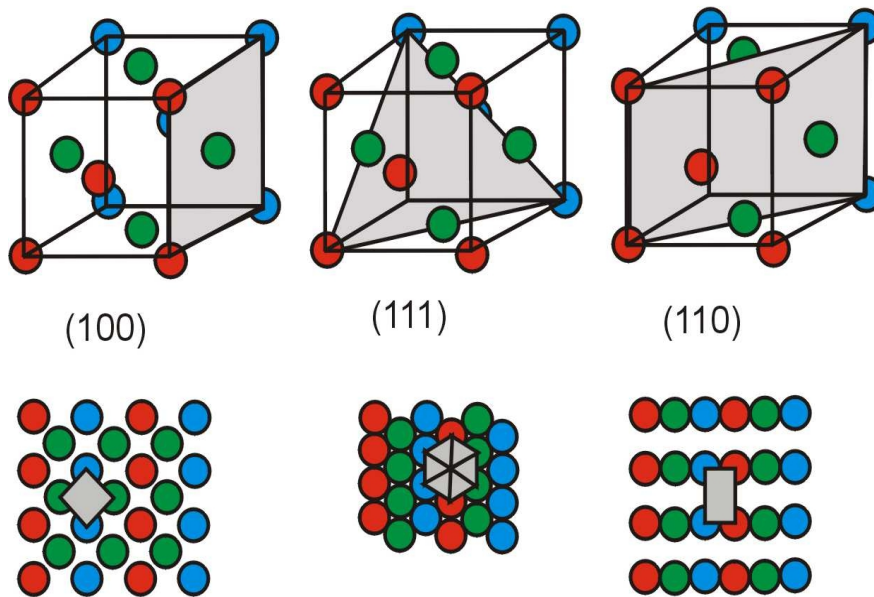
Figure 2-8 Face centrerd cube crystal (*e.g.,* Pt) cut in three low Miller index planes. Pt (111) is the most densely packed, followed by Pt (100) and Pt (110).

2.5.2. Oxygen reduction reaction

2.5.2.1. Mechanisms of oxygen reduction reaction on Pt

The ORR is a four-electron transfer electrocatalytic reaction where oxygen molecules are reduced to water. Because of its high cathodic standard potential (E^o = 1.229 V vs. SHE) and the formation of water as the reaction product, it is an ideal cathodic reaction for fuel cells. In an acidic medium, the ORR reaction is,

$$O_2 + 4e^- + 4H^+ \rightleftarrows 2H_2O \qquad E^o = 1.229 \text{ V vs. SHE} \qquad (2\text{-}14)$$
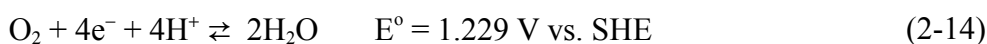
In a fuel cell, the ORR is coupled with *e.g.,* the hydrogen oxidation reaction on the anode side;

$$2H_2 \rightleftarrows 4e^- + 4H^+ \qquad E^o = 0.0 \text{ V vs. SHE} \qquad (2\text{-}15)$$
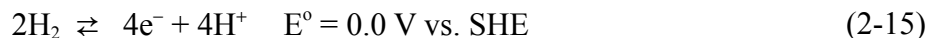
The challenge with these reactions is that both of them require the presence of catalyst because the reaction rates are slow. Pt is a good catalyst for both reactions; however, the exchange current densities of ORR and hydrogen oxidation on the Pt surface are quite different; 10^{-10} A/cm^2 and 10^{-3} A/cm^2, respectively, in an acidic condition at room temperature [2]. The potential loss by ORR is much more severe; therefore the catalytic research on ORR is much more actively pursued.

ORR catalysis involves adsorption of oxygen onto the surface of catalyst. Oxygen lone pair electrons interact with the partially filled Pt *d* orbital, and electrons from Pt 5*d* orbitals back-donate into oxygen π^* orbitals, which weakens the O-O bond. The adsorption process is sensitive to the surface structure and easily affected by the environment in which the reaction proceeds. It is currently accepted that the ORR proceeds via two pathways; a direct path (direct conversion of O_2 to H_2O involving four-electron transfer) or a series pathway (two-electron transfer forming hydrogen peroxide which may or may not be further reduced to water) [21]. It is also well-accepted that oxygen molecules are adsorbed onto the electrode, forming reaction intermediates on the electrode surface. Numerous possible reaction pathways occurring during ORR are shown in **Figure 2-9**. In a series pathway, the reaction proceeds as [22],

$$O_2 + 2e^- + 2H^+ \rightleftarrows H_2O_2 \qquad E^o = 0.67 \text{ V vs. SHE} \qquad\qquad (2\text{-}16)$$

$$H_2O_2 + 2e^- + 2H^+ \rightleftarrows 2H_2O \qquad E^o = 1.77 \text{ V vs. SHE} \qquad\qquad (2\text{-}17)$$

It has been proposed that different binding arrangements of oxygen molecules lead to either pathway. These arrangements are shown in **Figure 2-10**. The middle model (also known as Pauling model) is believed to go through both direct and parallel pathways [23]. Peroxide formation in fuel cells is undesirable for two reasons: 1) hydrogen peroxide generation involves only two electrons, providing less current than four electron transfer; and 2) hydrogen peroxide oxidizes the membrane electrolyte in a PEMFC, shortening the lifetime of the fuel cell. Usually, the direct-pathway dominates on a Pt surface [24, 25] at potentials above 0.2 V vs. standard hydrogen electrode, SHE, which is well below the operating potential of fuel cells. Indeed, the formation of H_2O_2 has been reported on a Pt surface, especially when the potential is below ~0.3 V vs. reversible hydrogen electrode, RHE [26, 27].
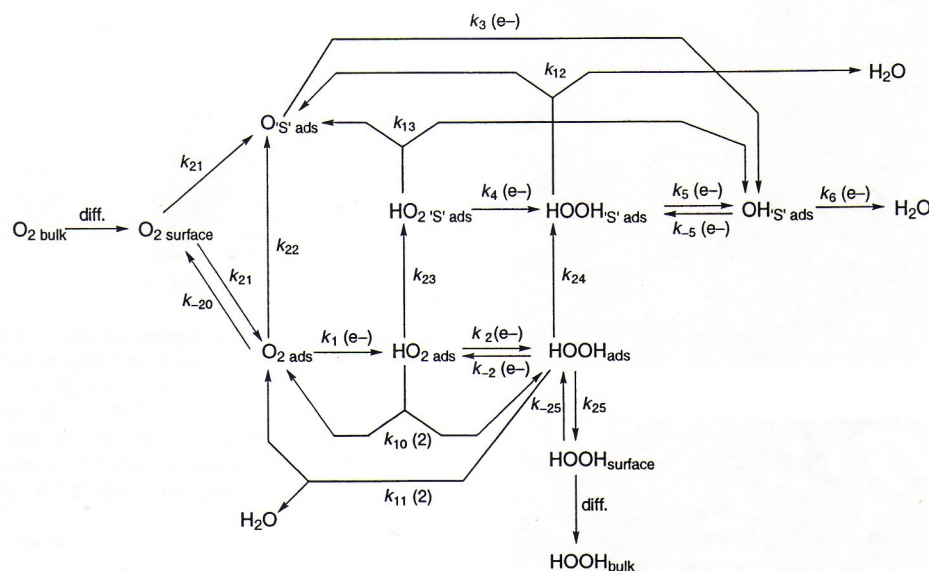
Figure 2-9 Possible reaction pathways for ORR. Final products are either water or hydrogen peroxide. Reprinted from [21]. Copyright 1987 with permission from Elsevier Sequoia S.A.
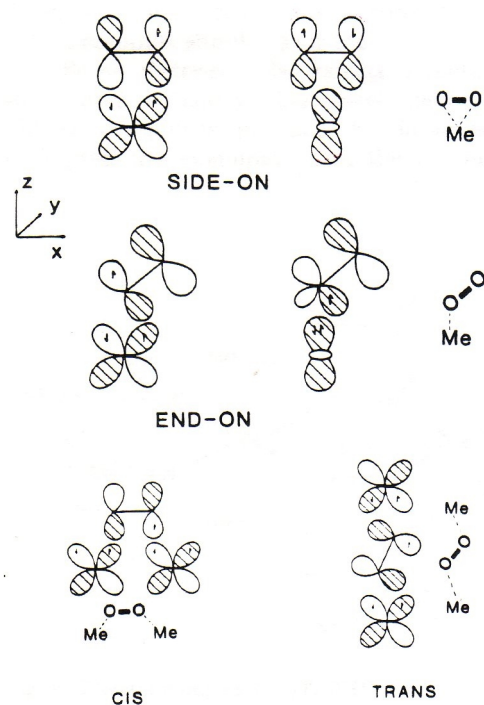
Figure 2-10 Three possible binding arrangements of molecular oxygen adsorbed onto a catalyst surface, Me. The end-on arrangement is believed to lead to the series pathway in ORR. The interactions between oxygen molecular orbitals and the Pt *d* orbitals are shown. Reprinted from [23]. Copyright 1986 with permission from Elsevier Sequoia.

The adsorption isotherm of oxygen on Pt was studied by Damjanovic *et. al.,* [28]. The authors found a Temkin type adsorption isotherm by fitting their experimental data to a theoretical model, which assumes a linear decrease in the adsorption enthalpy with total surface coverage, θ_T.

$$\Delta H_i = \Delta H_{0,i} - \chi_i \theta_T \qquad (2\text{-}18)$$

$\Delta H_{0,i}$ is the adsorption enthalpy of species *i* when the coverage is zero, and χ_i is the change in the enthalpy with respect to the coverage. The total coverage includes not only the species, *i*, but also the reaction intermediates formed in the course of the reaction. By further fitting their experimental data, the authors found the oxygen coverage was also linearly dependent on the applied potential and pH [22, 28]:

$$\frac{\Gamma}{\Gamma_{MAX}} = \theta = \frac{F}{\chi}\left(E + \frac{2.3\text{RT}}{F}pH - E^0\right) \qquad (2\text{-}19)$$

Also, the enthalpy of activation of oxygen dissociation on the Pt (111), (110), and (100) surfaces were found to be 42 kJ/mol in sulfuric acid, according to the Arrhenius equation [15]. Once oxygen dissociates on the metal surface and forms a substrate–O bond, protons can bind to the adsorbed oxygen. On Pt single crystal electrodes, ORR catalytic activity increases in the order (111) < (110) < (100) in sulfuric acid electrolyte [29]. The rate determining step for ORR is still controversial. The following steps have been reported as possibly rate determining for the ORR: adsorption of oxygen on the surface of Pt [30], adsorption of oxygen simultaneous with the first-electron transfer [31], adsorption of oxygen simultaneous with the first-proton transfer [32], simultaneous first-electron and first-proton transfer to oxygen [33, 34], and the first-electron transfer [24].

The origin of the slow ORR kinetics is unknown, and it is extremely challenging to pin point an exact cause. However, Nørskov *et al.,* have used density functional theory (DFT) to calculate the free energy of candidate intermediates during the course of the reaction. The authors found that, adsorbed oxygen and hydroxyl species are quite stable and the electron or proton transfer to the adsorbed oxygen or hydroxyl may be responsible for the sluggish kinetics at potentials close to the equilibrium [35].

Pre-adsorbed species can also affect the kinetics of ORR. Damajanovic *et al.,* found the

rate of ORR on the pre-reduced Pt surface is faster by a factor of 2 than the pre-oxidized Pt surface [36]. This is because the presence of oxide on the Pt surface can block the sites where molecular oxygen could adsorb [37]. Also, the specific adsorption of *e.g.,* (bi)sulfate anions can influence the reaction kinetics. Bisulfate adsorption is particularly severe on Pt(111) surface – it occurs potentials above 0.3 V vs. RHE [38]. (Bi)sulfate adsorption is less severe on Pt (100) surface although it surely occurs [39] when the potentials are above 0.6 V [38]. On the other hand, perchlorate anions do not significantly adsorb onto Pt surface. The rate of ORR determined in perchloric acid is therefore the fastest on Pt (111), followed by (110) > (100) surfaces; contrary to the rate measured in sulfuric acid [29]. The Tafel slope of ORR on the Pt (111) surface measured in sulfuric acid is reported as 120 mV/decade throughout the whole potential region, whereas the one measured in perchloric acid at higher current region was 77 mV/decade [15]. Despite the bisulfate adsorption and subsequent variation to the measured kinetics, sulfuric acid is commonly used for investigating ORR catalytic behavior because the most commonly available solid electrolyte, Nafion^{TM} , is a sulfonated ionomer, as shown in **Figure 2-1**. It has been reported that although specific adsorption of (bi)sulfate anions is definitely present, it is not strong enough to cause a change in the ORR mechanism, *i.e.*, change the direct pathway to the series pathway. Also water is believed to be co-adsorbed with the anion layer, which could relatively easily be displaced by incoming oxygen molecules [27].

2.5.2.2. ORR on rough Pt surface

Oxygen dissociation catalysis on a rough surface is significantly different compared to a smooth surface. (Rough surfaces are often represented by the "terrace (*i.e.,* flat) sites" and "step sites".) Adsorption and subsequent dissociation of oxygen molecules on Pt surfaces have been extensively studied [40, 41], showing that a Pt surface having steps and terraces exhibits more O$_2$ adsorption/dissociation at step sites due to the stabilization of the dissociated transition state. This is due to the higher coordination number for Pt atoms on terrace sites than those on step sites [42]. Work reported by Gee *et al.*, showed that the difference in the extent of oxygen dissociation process between Pt(111) (no step sites) and Pt(533) (with step sites) was governed by the presence of defects or steps [42]. Maciá *et al.*, also observed higher current on a Pt single

crystal electrode containing more steps and terraces than the one with a flatter surface [27]. Topography of the catalyst surface is therefore important information for the catalysis research.

2.5.3. CO oxidation reaction

CO oxidation reaction is known as a rate determining step of the methanol oxidation reaction, the anodic reaction in a direct methanol fuel cell (DMFC) [43]. Similar to the ORR, the rate of the CO oxidation is very slow, and the presence of a catalyst is essential. CO oxidation also involves dissociative chemisorption on a catalyst surface. The CO oxidation mechanism is still not fully understood. In this section, the current understanding of CO oxidation on Pt surfaces is presented.

2.5.3.1. Mechanisms of CO oxidation on Pt

The mechanisms of CO oxidation catalysis is still under debate, but the Langmuir-Hinshelwood mechanism [44] is generally accepted:

$$Pt + H_2O \rightarrow Pt\text{-}OH_{ads} + H^+ + e^- \tag{2-20}$$

$$Pt + CO \rightarrow Pt\text{-}CO_{ads} \tag{2-21}$$

$$Pt\text{-}CO_{ads} + Pt\text{-}OH_{ads} \rightarrow Pt\text{-}COOH_{ads} + Pt \tag{2-22}$$

$$Pt\text{-}COOH_{ads} \rightarrow CO_2 + H^+ + e^- + Pt \tag{2-23}$$

$$Pt + H_2O + CO \rightarrow CO_2 + 2H^+ + 2e^- + Pt \tag{2-24}$$
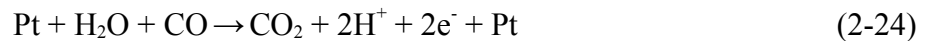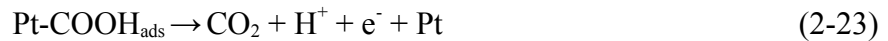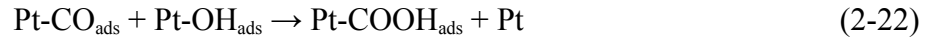
OH_{ads} indicates the oxygen-containing species, which is formed by the dissociation of adsorbed water on the Pt surface. The standard potential of the net CO oxidation should be approximately

0.1 V vs. SHE [45] but it requires 600 mV overpotential on the most effective catalysts known. The sluggish kinetics of CO oxidation arises from the dissociation of adsorbed water on the Pt surface to give -OH$_{ads}$ [46]. Relatively high anodic potential is required to "activate" water splitting. Alternatively, since CO and -OH are competitively adsorbed, there are many examples of the reaction rate being fit with the Langmuir-Hinshelwood mechanism [47].

$$Reaction\,rate = k_{CO}(N\,\theta_{CO})(N\,\theta_{OH}) = \frac{k_{CO}N^2 K_{CO}K_{OH}\,p_{CO}[OH_{ads}]}{(1+K_{CO}\,p_{CO}+K_{OH}[OH_{ads}])^2}$$ (2-25)

The term θ is the coverage of the corresponding molecules on the surface, K_{CO} and K_{OH} are the exchange equilibrium constants for CO and OH, respectively, k_{CO} is the rate constant of the CO oxidation, N is the total number of adsorption sites on the surface, and p_{CO} is the pressure of CO. The activation barrier for the reactions (equations) **2-22** and **2-23** together was determined to be ~100 kJ/mol [48, 44]. It should be noted that Equation **2-25** does not necessarily mean the rate determining step is the reaction between CO and OH. Rather, the reaction mechanism on CO oxidation is still not fully understood as pointed out earlier. The debate for this apparently simple reaction has been going for decades. For example, -OH$_{ads}$ appear in the reaction path may or may not be hydroxyl molecule [49]. Also there are at least three proposed mechanisms for removal of COOH$_{ads}$ at the last step [50].

CO oxidation is experimentally studied by anodic stripping voltammetry, which involves electrochemical preconcentration of adsorbed CO onto the electrode (catalyst) surface, followed by a potential sweep in an anodic direction, oxidizing the CO. The position (potential) of the stripping peak is examined and compared.

2.5.3.2. CO oxidation on low Miller index Pt surfaces

Although CO oxidation was studied on low Miller index Pt surfaces, the results differ among laboratories. Lamy *et al.,* showed CO stripping voltammograms recorded on Pt (100),

(110), and (111) surfaces in a CO saturated 0.1 M HClO$_4$ solution at room temperature at a sweeping rate of 50 mV/s [51]. The authors observed stripping potentials of 0.68 and 0.59 V vs. RHE on Pt (100) and (110) surfaces, respectively, and also observed two peaks at 0.694 and 0.95 V on Pt(111) surface. However, the results shown by Beden *et al.* [43], are different from Lamy's. They observed only a single peak on Pt (111) at potentials more negative than the peak recorded on Pt (100). The results reported by Herrero *et al.,* [52] only showed single peaks for all surfaces, and the stripping peaks for Pt (111) and Pt (100) were observed at 0.7 V and 0.73 V vs. RHE, respectively. In a 0.5 M sulfuric acid solution, the authors found the stripping peaks at much more positive potentials; 0.83 V and 0.77 V for Pt (111) and Pt (100), respectively.

Different shapes for the CO stripping voltammograms have been reported, just as Lamy found two peaks on the Pt (111) surface [51]. Two examples are given in **Figure 2-11a)** and **b)** which show multiple peaks and a single peak with a shoulder, respectively. The potential where the CO deposition was performed is shown as E$_{dep}$. These voltammograms were, at least in part, explained by Cuesta *et al.,* who identified the shoulder as the oxidation of bridge-bonded CO and the peak as the oxidation of linearly bonded CO using a polycrystalline Pt electrode [53]. (This is the indication that Lamy's Pt single crystal electrodes had some defects on the surface.) Different bonding arrangements are shown in **Figure 2-11b)** They also found the appearance of the shoulder only when the CO E$_{dep}$ was lower than 0.35 V vs. RHE, where high CO coverage was achieved. Surface enhanced IR spectroscopy results reported by Miki *et al.,* also indicated the slightly weaker bonding energy for bridge bonded CO [54], which is consistent with the findings by Cuesta.

Difficulties in understanding the CO oxidation electrocatalysis is, at least in part, due to the sensitive nature of adsorbate to its surroundings. It has been reported CO stripping potential is sensitive to temperature [52], specifically adsorbed anions present in electrolyte [43, 55], CO deposition potentials [53], scan rates [56], and deposition time [43] but the most complex factor is the surface structure of a catalyst [52, 51, 57, 58]. It is not only the type of crystal faces of catalysts, but also depends on the number of crystal defects. Even if a single crystal surface is prepared, defects are always present. Although CO oxidation appears as a very simple reaction, it is extremely sensitive to its environment, and controlling the experimental parameters is necessary.
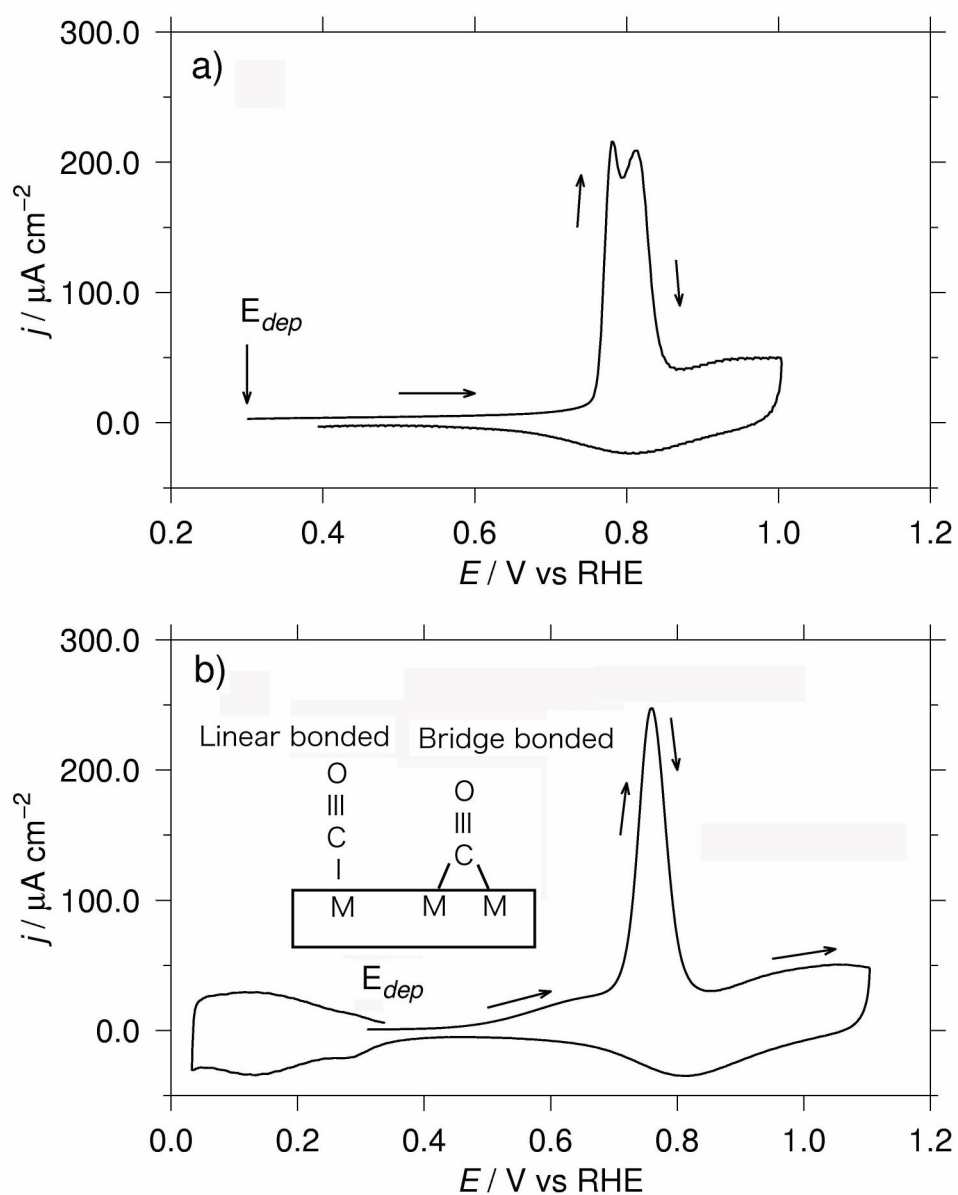
Figure 2-11 Examples of different CO stripping voltammograms recorded under identical conditions. a) Voltammogram with multiple peaks; b) A single peak with a shoulder. E_{dep} is the CO preconcentration potential applied to the electrode. The difference is probably due to the electrode surface characteristics which are dynamically changed. The shoulder in b) is possibly due to the oxidation of bridge bonded CO, whereas the main peak is due to the oxidation of linearly bonded CO [53].

2.5.3.3. CO oxidation on a rough Pt surface

As shown in the previous section, when a catalyst surface is rough, its work function is lower than a smooth surface due to the surface dipole contribution [59]. Again, rough surfaces are often represented by the "terrace (*i.e.,* flat) sites" and "step sites", but hydrocarbon adsorbates often exhibit 10-20 % stronger binding energy than on a terrace site [60]. Xu *et al.,* found that when CO and oxygen molecules are co-adsorbed on a surface containing both terrace and step sites, CO tends to be shifted to terrace sites, and oxygen tends to adsorb onto the step sites. They also found CO on terrace sites, oxidized to CO_2 more easily than on step sites. The possible reason is the difference in bond strength for CO on terrace or step sites; 96 kJ/mol or 151 kJ/mol, respectively [59]. The binding energy of oxygen on step sites is higher than that on terrace sites. It is possible the weaker bonding of CO, and/or stronger binding of oxygen on steps favour the oxidation process. The stronger binding energy on step sites must be a result of electronic effects. However, the authors also suggest a geometrical effect. The distance between CO (terrace) to O_2 (step) on Pt (335) (the surface containing both terraces and steps) is shorter than the distance between CO and O_2 both on step sites, which may also contribute to more efficient catalysis [59, 60]. An alternative explanation is the surface structure-dependent CO adsorption, recognized by Mikita *et. al* [58]. The authors realized CO adsorbs only on defect sites when the CO coverage is very low. This suggests the presence of crystal defects increases the surface concentration of CO, which would lead to more effective CO oxidation.

2.5.3.4. Adsorbate-induced surface restructuring in the Pt surface

When adsorbates are present on the surface, and if the interaction between the adsorbate and substrate is strong, it often breaks a metal-metal bond (in the substrate) to form a metal-adsorbate bond, leading to the shift in equilibrium positions in surface atoms [61]. When small molecules, such as hydrogen, CO and oxygen, are adsorbed onto a metal surface, and if the interaction between adsorbate and the surface atoms is stronger than the interaction between atoms in the metal, there may be a surface reordering [62]. For example, when oxygen is

adsorbed on the Ni(100) or Cu(100) surface, metal *d* and O *2p* orbitals interact very strongly and the orbitals hybridize to form bonding and antibonding orbitals. Subsequently, Cu or Ni surface atoms reconstruct, which shifts the antibonding orbitals up higher than the Fermi level of the metal. This takes shared electrons away from antibonding orbital, which subsequently lowers the energy of the oxygen-adsorbed metal surface [63]. A Pt surface does not encounter severe surface restructuring with oxygen adsorption during the ORR, but does with CO adsorption. Gritsch *et al.,* observed the reconstruction of Pt(110) surface transforming from (1×2) to (1×1) after CO was adsorbed onto the surface [64]. Behm *et al*., has observed the phase transformation from Pt (100) hexagonal structure (Pt-hex) to Pt (100)-(1×1) when CO was adsorbed onto Pt-hex sites. The structures of Pt-hex and Pt (100)-(1×1) are shown in **Figure 2-12**. Despite the CO-CO repulsive interactions, CO adsorbed onto Pt-hex sites formed small islands (~15 CO molecules/island) even at low coverage (θ<0.5). They also found that once hex-(1×1) transformation occurred, CO molecules are trapped at (1×1) sites [65]. The reverse process also occurs; surface reconstruction of Pt(1×1) to Pt-hex is achieved by desorption of CO from the Pt (1×1) surface. The thermodynamics of this process has been presented by Thiel *et al* [66]. An energy diagram of their findings is summarized in **Figure 2-13**. When a clean Pt (100) surface is present without CO adsorbed, Pt-hex is energetically more stable than (1×1) by "ΔE" (shown at the upper part of diagram). The activation energy (E*) of transformation of hex to (1×1) is 20~25 kcal/mol. However, when CO is adsorbed onto a Pt (100) surface, it lowers the energies of (1×1) and hex by $\theta_2 E_2$ and $\theta_1 E_1$, respectively, where E and θ correspond to the CO adsorption energy and CO coverage on each surface. δE in the diagram therefore represents the energy difference between CO-covered Pt (1×1) and Pt-hex structures, so the phase transition occurs when δE is negative and also smaller than ΔE; *i.e.*, $\theta_2 E_2 - \theta_1 E_1 < \Delta E$. In their contribution, they also found that the trigger for this transformation is purely the adsorption of CO, but because E_2 is greater than E_1, θ_1 must be greater than q_2 at equilibrium, thereby the energies required to transform the hex structure to (1×1) by CO adsorption or to transform (1×1) to the hex structure by CO desorption are different; *i.e.,* A hysteresis loop is observed [66]. Although this particular thermodynamic solution may not apply to all other phase transition phenomena, their findings do show the approach one may need to take in order to study the mechanisms and energetics of such transformations. This is important for electrocatalysis as many catalytic processes are dependent on the detailed surface structure.
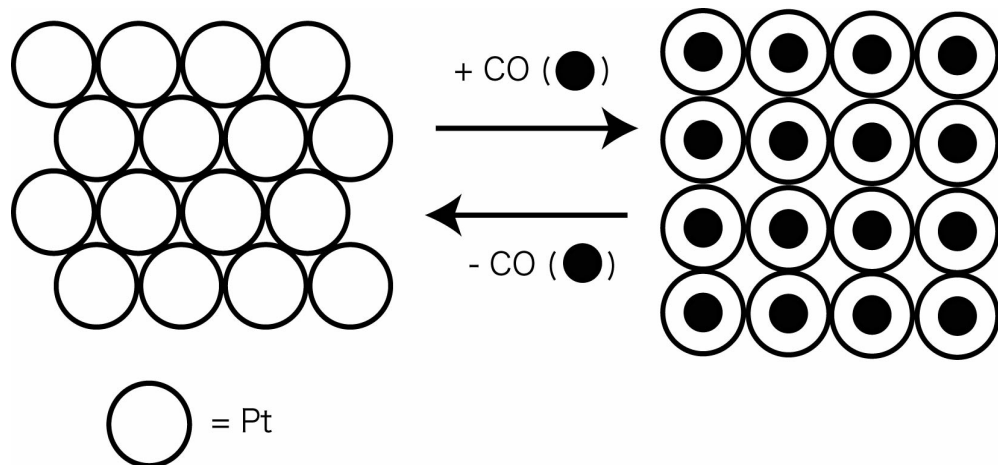
Figure 2-12 Atomic arrangements of Pt (100)-hex and Pt (100)-(1×1) structures. Pt (100)-hex is formed over Pt (100) to minimize the surface energy of the crystal; however, when CO is adsorbed onto the hex structure, surface reconstruction occurs, transforming the overlayer into (1×1) structure.
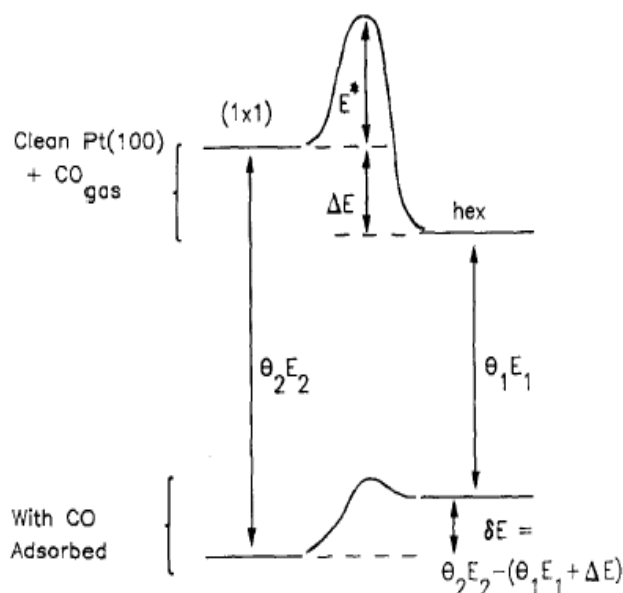
Figure 2-13 Energy diagram showing the surface reconstruction of Pt(1×1) ↔ Pt-hex structure with the CO adsorption. When a clean Pt (100) surface is present without CO adsorbed, Pt-hex is energetically more stable than (1×1) by "ΔE" and the transformation to Pt-hex requires the activation energy, E^*. However, when CO molecules are adsorbed onto the Pt (1×1) surface, its energy is lowered significantly that the Pt (1×1) exhibits a lower energy. Reprinted with permission from [66]. Copyright 1983 American Institute of Physics.

Understanding the CO oxidation mechanism is probably made more complicated by the adsorbate-induced surface reorganization. The surface always attempts to attain the minimum energy possible. In fact, it is suggested by Somorjai *et al.,* that adsorbate-induced restructuring may change the active sites of catalytic reactions (especially the rate determining steps) and therefore, it is crucial to study active sites in the presence of adsorbates, rather than on a clean catalyst surface [14].

2.6. Pt-based alloys

Assume the PEMFC is operated at E=0.6V with a current density of 500 mA/cm². The power output from the single cell, according to **Equation 2-3** gives 0.3 W/cm² (the power output calculated with a current density, j). Typical Pt loading of one catalyst layer is ~ 1 mg/cm²; therefore anode and cathode together, one single stack fuel cell contains 2 mg/cm² of Pt. If an automobile requires a minimum power of 50 kW, the price of Pt required (assuming Pt costs 992 USD/oz [4]) is [2],

$$\frac{50,000\,W}{0.3\,W/cm^2} \times \frac{2\,mg\,Pt}{cm^2} \times \frac{US\,\$992}{oz} \times \frac{1\,oz}{28,349\,mg} = US\,\$\,13,164 \qquad (2\text{-}26)$$

The price of platinum alone is too expensive for the cost of automobiles, and research seeking to reduce the usage of Pt (aiming for the Pt loading of 0.1 mg/cm²) has been actively pursued. Diluting Pt with other metals – the first row of transition metals in particular – is an excellent way to reduce the Pt loading in fuel cells and also the alloys are known to improve the kinetics of the fuel cell reactions as compared to Pt. This section reviews the current understanding of Pt-based alloys for fuel cell reactions.

2.6.1. Fuel cell reactions on Pt bimetallic alloy catalysts

Fuel cell reactions have also been extensively studied on Pt-based alloys. Numerous alloys of transition metals in the first row of the periodic table have shown more efficient catalysis on ORR compared to Pt. Fewer numbers of Pt-alloys have shown improved kinetics for CO oxidation. Nonetheless, the improvement appears to be due to the changes in the electronic structure and the geometrical parameters in either component of the alloy compared to its pure form. This section describes the ORR and CO oxidation catalysis measured on Pt-based alloys and summarizes the alloying effects and their influence to the fuel cell reaction catalysis. Adsorbate-induced surface reorganization observed on alloys is also briefly presented.

2.6.1.1. ORR on Pt bimetallic alloy catalyst

There are a number of Pt-transition metal alloys reported as more efficient catalysts than Pt itself. In this thesis, the focus is limited to bimetallic Pt alloys, although trimetallic Pt alloys have also been tested for fuel cell applications [67, 68]. Metals that have been alloyed with Pt and showed improvements in measured kinetics for ORR include Co [69, 26], Ni [26, 69], Cr [70], Au [71], Ru, Ti, V, Fe, and Ir [67]. PtRu, PtCo, PtCr, and PtNi have particularly shown excellent catalytic activities; 2~4 fold enhancement in kinetics of the reaction. There are two changes that alloying seem to induce in Pt: 1) increase in Pt $5d$ vacancies, and 2) decrease in Pt-Pt bond distance. An increase in the Pt $5d$ orbital vacancy concentration reduces $2\pi^*$ backdonation into O_2, modifying O-Pt or destabilizing O-O bonds, aiding oxygen dissociation. The shorter Pt-Pt bond may promote ORR by a geometrical effect. Compressive strain, caused by shortening Pt-Pt bond distance, is also said to be related to the increase in Pt d band vacancies; the d-orbital overlaps are increased, resulting in a broadening of the average d-band width and lowering the average energy [72].

Activation energies for the ORR on Pt-Ni, Pt-Cr, and Pt-Co in an actual fuel cell operation condition have been measured and compared to pure Pt [70, 73]. The activation energies of alloys were 1.5~3 times less than that of Pt, accounting for the enhanced ORR activities. H_2O_2 production on these alloys was also investigated [74], but no significant amount of H_2O_2 was detected. Also, the calculated Tafel slopes on Pt-alloys were similar to the one on Pt surface, indicating alloying did not influence the reaction mechanism [70]. The authors were also able to show an increase in the exchange current density on PtCo by a factor of 3 comparing to pure Pt in their fuel cell setup. Other Pt alloys such as -Ni or -Cr also showed 2~4-fold increase in the exchange current densities.

Figure 2-14 shows the activity of O_2 dissociation (*i.e.,* log-scaled rate constant for oxygen dissociation) with respect to oxygen binding energy [35]. Activity is also related to the occupancy of the Pt $5d$ orbital [75]. This plot is called a volcano plot, and the closer the element to the summit, the more efficient the catalyst. Pt is the best catalyst for oxygen dissociation for a single element on the plot shown. Xu *et al.*, showed that by alloying Pt with Co, Pt_3Co was placed at the higher position than Pt on the volcano plot [75].
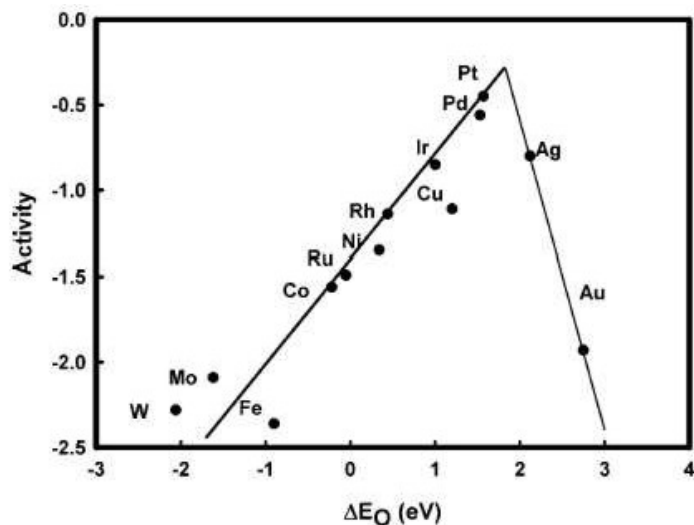
Figure 2-14 The volcano plot (theoretically determined) showing the ORR activity with respect to the oxygen binding energy. The ORR activity corresponds to the energy of activation barrier of the rate determining step calculated. The closer the element is to the summit of the plot, the more efficient the ORR catalysis is. Reproduced in part with permission from [35]. Copyright 2004 American Chemical Society.

2.6.1.2. Pt skin formation

Although Pt alloys have been formed, the very top layer of the alloy often consists of only pure Pt atoms [76, 26, 77, 64]. This enrichment of Pt on the surface is often called a "Pt skin" structure [26]. The second layer, on the other hand, becomes Pt deficient and therefore enriched with the other component of the alloy. Such phenomena are the result of dissolution of transition metal that was initially present on the surface, as well as three other factors: 1) Differences in surface energies between alloy components [78, 79]; 2) Differences in size between the alloy components; and 3) the energy of mixing [79]. Pt-skin can also be achieved by

annealing Pt-alloys, such as PtCo or PtNi [26, 80]. Bardi *et al.*, reported the formation of Pt-skin on Pt_3Co alloy, *i.e.*, the topmost layer of the alloy was covered only by Pt atoms, but also reported the electronic structure of the top Pt layer observed with the X-ray photoelectron spectroscopy (XPS) was not the same as that of pure Pt [76], suggesting the electronic disruption due to the underlying Co.

ORR catalytic activities have also been investigated on the Pt-skin. An example was shown with Pt_3Ni alloy compared to Pt [80]. The polarization curves comparing polycrystalline Pt and as-prepared-Pt_3Ni clearly showed the positive shift in onset potential of the ORR on the Pt_3Ni surface; however, annealed Pt_3Ni showed even more positive onset potential for the reaction. The reason for the further enhancement in the ORR catalysis by Pt-skin was the weak $Pt-OH_{ads}$ interaction due to a modification of the electronic structure of Pt by the underlayer Ni. Interestingly, though, the activation energy for the ORR on the Pt-skin was not significantly different from the one on the as-prepared-Pt_3Ni. The authors also detected no H_2O_2 formation [80].

2.6.1.3. CO-oxidation on Pt-alloy surfaces

There are a few Pt-alloys that enhance CO oxidation over pure Pt. These include PtRu [81-84, 20, 85] and PtSn [81, 86]. Other alloying metals, such as Mo [87, 88], Re [89], and Rh [90] have also been reported, although the Pt alloyed with these metals did not influence the kinetics of the reaction significantly.

There are two theories explaining the enhanced mechanism of CO oxidation on Pt-alloys: Bifunctional theory [85] and the ligand effect [91]. Bifunctional theory states that the alloying metal provides nucleation sites for OH_{ads} at more negative potential than on Pt, whereas Pt serves to adsorb CO. Fast formation of $-OH_{ads}$ leads to more facile CO oxidation process. The ligand effect arises when the electronic structure of Pt is altered due to the presence of alloying metals, which in turn modifies Pt-CO binding sites. Gasteiger and coworkers observed 2-3 fold increase in the CO oxidation kinetics on a PtRu alloy compared to the one measured on Pt [83].

The contribution from the ligand effect is under debate. Numerous reports have

suggested that it is less important than the bifunctional effect [92-95]. For example, placing Ru atoms in the vicinity of Pt atoms, instead of forming a PtRu alloy, also improved the CO oxidation kinetics [96]

In summary, Pt alloyed with the first row of transition metals increase Pt $5d$ vacancies and decrease the Pt-Pt bond distance. These electrical and geometrical changes enhance the catalytic activities of ORR on alloy surfaces, compared to Pt. Pt-skin formation on Pt-alloys further improve the catalytic activity by changing the Pt electronic structure, modifying the Pt-OH_{ads} bond energies. Pt alloys reported in the literature are usually Pt_1M_1 or Pt_3M, where M is one of the transition metals. The use of Pt-alloys, instead of pure Pt, replaces 30~50 % of Pt loading in fuel cells. However, Pt-alloys face a challenge, especially in the fuel cell's acidic condition – chemical stability [97, 26].

2.6.1.4. Stability of Pt-based alloys under a fuel cell operation conditions

The stability of catalysts is an important issue upon developing fuel cells. During the fuel cell operation, the non-precious metals of Pt-alloys leach out and contaminate the solid electrolyte, which may cause four unfavourable outcomes: 1) decrease in the ionic conductivity of membrane due to dehydration; 2) increase in the ionic resistivity in the cathode due to blocking the cation exchange sites; 3) decrease in oxygen transport to the catalyst layer; and 4) damaging the membrane if a certain type of metals, such as Ti or Fe, are released [97]. Research seeking more stable Pt-alloys is important, as this issue is strongly related to the fuel cell lifetime. In this section, however, only the chemical stabilities of alloys will be discussed.

There are two reasons why metal components of alloys leach out, *i.e.*, either incomplete alloying during the manufacture or insufficient enthalpies of mixing of Pt-alloys under fuel cell operating conditions [97]. Pt-alloys are vulnerable to acidic conditions. Stamenkovic *et al.,* prepared 3:1 PtCo and PtNi alloys to find their catalytic activity compared to pure Pt; however, they found the transition metals leached out in an anodic (oxidative) scans of cyclic voltammograms recorded in a 0.5 M acidic solution [26].

Colon-Mercado and Popov studied commercially available alloys, *i.e.*, Pt-Co, Pt-Ni, Pt-Fe, and Pt-V, and measured the loss of transition metals from the alloys. The authors immersed the alloys (dispersed on GDL) in an acidic liquid electrolyte, applied a constant potential at 0.8 V vs. NHE over a prolonged time, and tracked the metal dissolution by analyzing the solution by atomic absorption spectroscopy [69]. The results indicated the dissolution of a significant amount of metal. Though they studied for over 70 hours, most of the metal dissolved in the first couple of hours of polarization. The alloy that showed the least metal leaching was Pt_3Ni, but it still showed 5 % metal dissolution within the first ~3 hours. Considering this was 75% Pt, these alloys are not stable in an acidic environment. The worst alloy was 1:1 PtCo which showed 40% metal loss in the first 1 or 2 hours of polarization. Gasteiger has also found PtCo exhibits a high degree of leaching; 35 % Co loss after 24 hours of immersing the alloy into the alloy (no potential applied).

Multiple pre-leaching steps have been suggested by Mukerjee *et al.* [98]*,* to purposely dissolve any transition metals before incorporating the alloys (on MEAs) into a fuel cell assembly. In this way, only a few per cent of the transition metals leached out of the alloy during fuel cell testing, and the catalytic activity was still better than that on Pt. However, this is an extra step that industry must perform in the fabrication process, that can only increase the cost.

2.6.1.5. Adsorbate induced surface segregation

Adsorption of atoms or small molecules on alloy surfaces may induce a large change in the surface composition. When one component of multi-metallic alloys has a very different adsorption energy from the other component(s) of the alloy, atomic diffusion perpendicular to the surface may occur by breaking metal-metal bonds. Several examples are found in ref. [99]; for example, surface of Cu-Mn or Ag-Mn films become enriched with Mn upon adsorption of oxygen, or the surface of AgPd alloy becomes Pd-enriched upon CO adsorption. The authors explain such phenomena purely due to thermochemical effect.

2.7. PtZn

This section provides a general overview of the characteristics of the PtZn alloy. The PtZn alloy utilized in this thesis was facilitated by so called the underpotential deposition of Zn onto the Pt surface. Subsequent alloying effects are presented and compared to those observed in other alloys. Although the stability of a PtZn alloy in a fuel cell operating condition has never been reported prior to our work, theoretical and experimental data encompasses a reasonable chemical stability in an acidic condition, and this will also be reviewed in detail.

2.7.1. Pt, Zn, and bulk PtZn "alloy"

The crystal structures of pure Pt and Zn are *fcc* with the lattice parameter of 2.77 Å, and *hcp* with the lattice parameters of 2.6649 and 4.9468 Å at room temperatures, respectively [100]. When Pt and Zn are combined, they form compounds at various compositions. The phase diagram of PtZn (some regions are still in question) is shown in **Figure 2-15**. The regions where the compositions are known are intermetallic compounds (*i.e.,* Pt-Zn compounds at the given stoichiometry with ordered crystal structures). For example, Pt_1Zn_1 and Pt_3Zn_1 intermetallic compounds with $L1_0$ (AuCu) and $L1_2$ ($AuCu_3$) structures [101]. Pure Pt and Zn in the phase diagram and possibly some regions of the phase diagram (especially at higher temperatures) are solid solutions (*i.e.,* disordered crystal phases with various compositions).

An "*alloy*" is defined as either a solid solution or intermetallic compounds with some disorders in its lattice atomic arrangements. In the current fuel cell literature, the term, "alloy" is interchangeably used for a solid solution or for an intermetallic compound, although "intermetallic compounds" are, strictly speaking, not an alloy because they have definite stoichiometry and ordered lattice structures that exhibit a characteristic diffraction pattern. In **Chapter 4~6**, we will show an electrochemically prepared mixed metal containing Pt and Zn. This metal showed orbital mixing between Pt and Zn atoms; however, the crystal structure and the atomic arrangements of this metal are still in question. Also the metal surface structure is generally very different from the bulk structure. Therefore in this thesis, we call our mixed metal

an "alloy" which may be a solid solution or an ordered intermetallic compound.
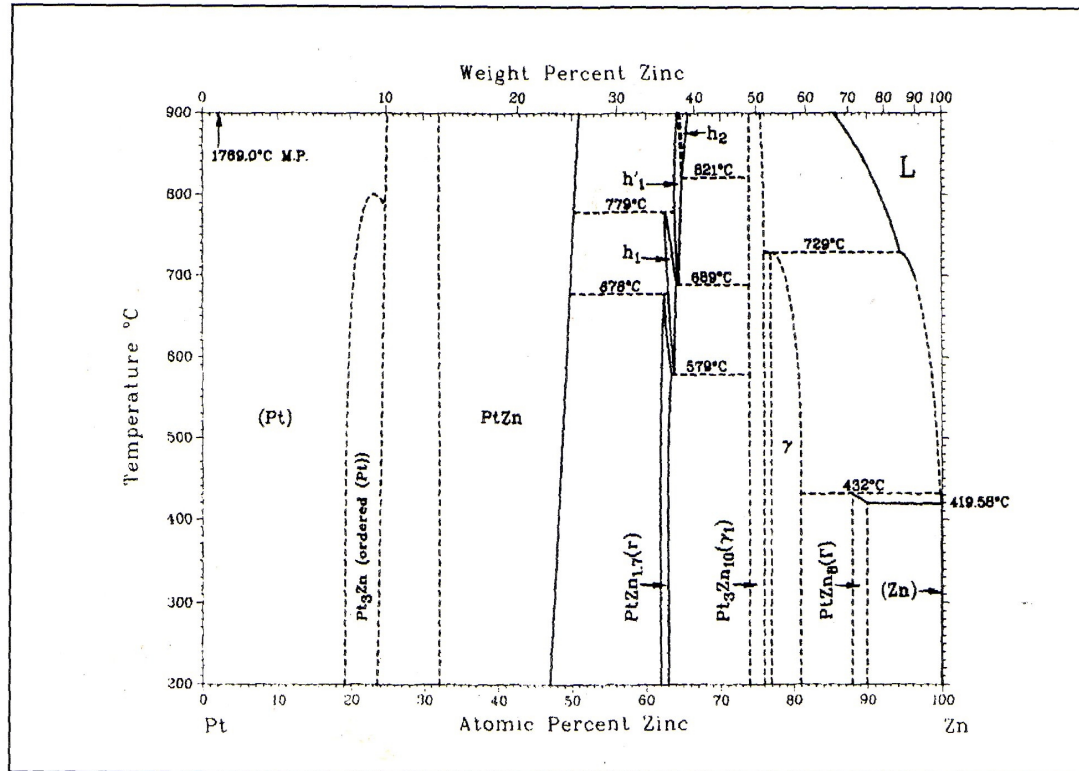
Figure 2-15 PtZn phase diagram. Reproduced in part from [102]. Copyright 1991 with kind permission of Springer Science and Business Media.

2.7.2. PtZn alloy formation

2.7.2.1. Zn underpotential deposition on Pt

Bulk metal deposition from a solution onto another metal can occur electrochemically, and the onset potential can be predicted by the Nernst equation. The standard potential of Zn^{2+} reduction (*i.e.,* $Zn^{2+} + 2e^- \rightleftarrows Zn(s)$) is -0.763 V vs. SHE [103]. Deposition of Zn on Pt in a highly acidic medium therefore is predicted not to occur as hydrogen evolution from Pt ($E^o = 0.0$ Vvs. SHE) at such a low potential prevents Zn^{2+} from approaching to the electrode surface. However, this is not the case, as Zn forms a so-called underpotential deposition (UPD) layer onto Pt before hydrogen evolution starts. UPD is an electrochemical phenomenon where deposition of metal occurs at a potential more positive than predicted by the Nernst equation [104]. UPD of electrodeposited metal thus formed grows epitaxially, *i.e.,* the growth is two-dimensional and the morphology of the film follows that of the substrate. There are two criteria for metal to form a UPD onto a substrate: 1) The metal-substrate interaction is stronger than metal-metal interaction, and 2) the sizes of atoms of deposited metal and substrate are similar (*i.e.,* small lattice mismatch) [104].

Experimentally, the formation of a Zn UPD layer was reported by Aramata, via cyclic voltammograms [105]. The epitaxial growth of Zn onto Pt has been confirmed [106], and Pt and Zn together satisfy both of the criteria for UPD [105, 107]. Zn UPD on a polycrystalline Pt in a H_2SO_4 solution occurs at potential 1.11 V more positive than bulk Zn deposition [108]. According to Kolb [104], the difference in the UPD and bulk deposition potentials represents the difference in chemical potentials due to the interaction among Zn atoms in bulk and the interaction between Zn and Pt. The potential of a UPD layer, E_{UPD}, relative to the Nernst potential is calculated by the following equation [109]:

$$E_{UPD} = E_{Nernst} - \frac{\theta \Delta H_{S-M}}{nF(CN_S)} \qquad (2\text{-}27)$$

In this equation, θ is the coverage of the UPD layer, ΔH_{S-M} is the enthalpy of bond formation between metal-substrate, and CN_S is the lattice coordination number of the substrate. A Zn UPD

layer at a potential negative of E_{UPD} is stable, and usually the difference between E_{UPD} and E_{Nernst} for the Pt-Zn system is ~1 V [105].

Guerra *et al.,* also calculated the 1:1 Pt/Zn lattice mismatch to be only 4% (using the interatomic bond distance of 2.775 Å for Pt, $d_{0,Pt}$; and of 2.665 Å for Zn, $d_{0,Zn}$) [107],

$$f = \frac{d_{0,Zn} - d_{0,Pt}}{d_{0,Pt}} = \frac{2.665 - 2.775}{2.775} = -0.04 \qquad (2\text{-}28)$$

Also the diffusion coefficient of Zn into Pt is relatively large; 107 times greater than for Zn into Cu at 100 ^{0}C [110]; indicating the possibility of the rapid alloy formation without significant distortion of the crystal lattice.

2.7.2.2. Transformation of Zn UPD into Pt-Zn alloy

Transformation of Zn UPD layer into a Pt-Zn alloy was first realized by Despic *et al.* [106]*,* and later well-characterized by Guerra *et al.* [107]. The cyclic voltammograms recorded by Despic *et al.,* in a 1.5 M ZnSO$_4$ solution (pH=3.5) on a Pt electrode is shown in **Figure 2-16**. Peak III' were identified as hydrogen desorption. Bulk Zn deposition (or overpotential deposition; OPD) occurs at the long tail at the end of cathodic scan, and peak I' was assigned as the stripping of the bulk Zn thus deposited. Zn UPD layer formation was assigned to region II which occurs before hydrogen adsorption, in agreement with another literature report [105]. The authors gradually extended the cathodic limits of voltammograms and observed dramatic changes in the reverse scan. Peak II' was identified also as stripping of Zn; that was more tightly bounded to the substrate than Zn in Peak I'. Two remarkable features are Peak IV' and V'. Peak IV' appears only when the potential limit was made very cathodic. The authors concluded this was the oxidation of PtZn alloy, which might have formed in the potential region of III. Peak V' was also assigned as stripping of Zn that had been so strongly bounded, and it could only be removed by the oxidation of the substrate. This experiment shows the rapid transformation of Zn UPD into an alloy.

Similar behavior was observed by Guerra *et al.* When the electrode was polarized in a

0.1M ZnSO₄ solution at the Zn UPD potential for a long time, an increase in measured current, just like Peak IV' and V' of Despic's, in the anodic scan was also observed. This increase was limited to the first 600 seconds of polarization. Once formed, PtZn alloy appears to be very stable as it could only be removed by oxidation of the substrate or by immersion into aqua regia [107].
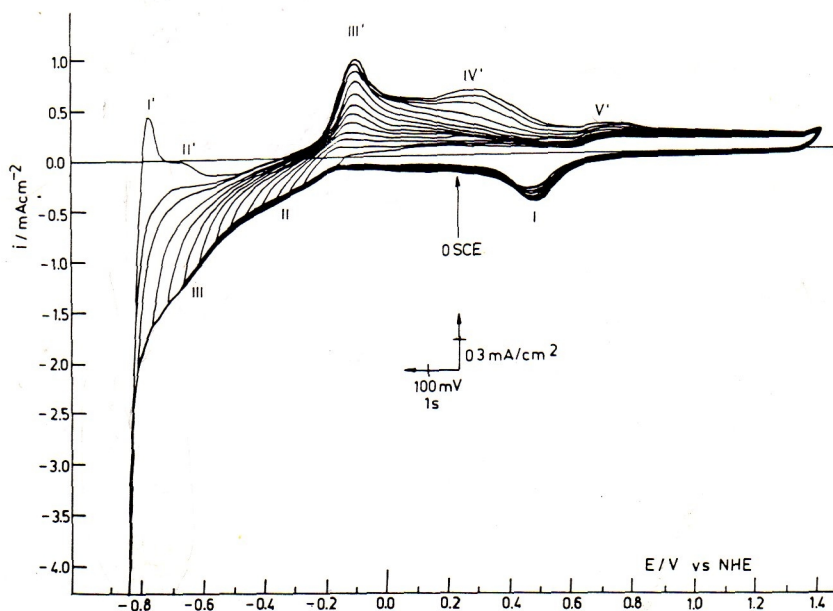
Figure 2-16 The cyclic voltammograms recorded by Despic *et al.,* in 1.5 M ZnSO₄ solution (pH=3.5) on a Pt electrode. Peak potential region assignments are as follows: Peak I – Pt oxide reduction; Region II – The Zn UPD formation on the Pt; Region III – Post-UPD potential region reflecting the Pt-Zn alloy formation; Peak I' – Zn stripping from the bulk Zn; Peak II' – UPD Zn stripping; Peak III' – hydrogen desorption; Peak IV' – Oxidation of PtZn alloy; Peak V' – Zn stripping from the PtZn alloy. The PtZn alloy was formed when the cathodic potential limit was extended in Region III while the CVs were recorded, indicating a rapid transformation of the UPD Zn. Reprinted from [106]. Copyright 1982 with permission from Elsevier (Pergamon Press Ltd).

Taguchi *et al.,* investigated Zn UPD in 0.1 M sulfuric acid solution onto Pt (111), Pt (110), and Pt (100) surfaces. They observed no significant difference between (111) and (100) surfaces with or without the presence of Zn^{2+} in the electrolyte, whereas they clearly observed

the formation of a Zn UPD layer on the Pt (110)-(1×2) surface [111]. This work suggests Zn preferentially deposits onto particular crystal faces of Pt, and therefore, polycrystalline PtZn surfaces, such as the one prepared by Guerra, may be heterogeneous.

2.7.2.3. Stability of PtZn – Theoretical point of view

The majority of work reviewed in this section was done by Rodriguez *et al.,* reported in 1990s. A lot of their work involved investigating metal-metal bonds in bimetallic alloy surfaces mostly by utilizing CO- thermal desorption spectroscopy (TDS), XPS, and density functional theory (DFT). When Pt and Zn form an alloy, electrons are delocalized extensively occurs, which in turn lowers the energy of Pt in the alloy relative to the pure metal. It is also intriguing that Pt acts as an electron acceptor and Zn acts as an electron donor in the alloy formation; contrary to other Pt-transition alloys. This in turn appears to give the PtZn alloy its chemical stability which is unique compared to other Pt-transition metal alloys. This section reviews the electronic and geometric structural changes observed in both Pt and Zn due to alloying that may account for the chemical stability of the alloy, which may be very useful for the applications in fuel cells.

2.7.2.4. Pt alloying effects

Theoretical calculations have predicted several electronic perturbations upon forming a bimetallic bond between Pt and Zn, which was also, to some extent, supported by experimental data.

As mentioned in the previous section, one of the changes due to alloying Pt with transition metals is a decrease in Pt $5d$ orbital population. Molecular oxygen is then assumed to be adsorbed more readily to Pt in the alloy, resulting in the enhancement of the ORR kinetics as compared to Pt. Prior to our work, transition metals on the right hand side of the periodic table relative to Pt had never been considered as alloying metals in the field of fuel cell

electrocatalysis. This was probably because many predicted that electron transfer from Pt $5d$ to the more-filled d-orbitals of metals, like Cu or Zn, was unlikely. However, according to the molecular orbital theory calculations by Rodriguez, *et al*., an increase in Pt $5d$ orbital vacancy was predicted and then further supported by experimented CO thermal desorption spectrometry [112]. The desorption temperatures for adsorbed CO from the PtZn surface were always less than that for pure Pt, indicating that CO is less tightly bonded compared to pure Pt. The ability of the metal to adsorb CO depends on its d-band structure. Alloying Pt with Zn creates more vacancies in the Pt $5d$ states, and the extent of $2\pi^*$ back-donation from the metal to the CO decreases. In their experimental results, the strength of Pt-CO bonding was reduced by approximately 2~6 kcal/mol [112]. This result clearly showed a decrease in Pt $5d$ electron density after PtZn alloy formation.

The decrease in Pt $5d$ electron density in PtZn is not due to a simple electron transfer from the Pt $5d$ to the Zn ($4s,p$) orbitals, but rather involves an extensive electron delocalization and Pt orbital rehybridization, which eventually moves Pt $5d$ electrons into the Pt-Zn bimetallic bonding orbitals. Rodriguez's prediction was further supported by Chen *et al*. [101] The separation between Pt-Pt and Zn-Zn in their pure forms are 2.77 (fcc structure) and 2.6649 Å (hcp structure), respectively. However, cluster calculations predict that after alloying, Pt-Pt and Zn-Zn bond distances increase to 2.818 and 2.890 Å, respectively, but Pt-Zn bond distance is 2.696 Å; much shorter than either Pt-Pt or Zn-Zn bonds. This indicates that there is a substantial electron transfer from both Pt and Zn orbitals into the bimetallic bonding orbitals, which is an indication of the strength of the PtZn bimetallic bond. This characteristic was observed by Despic; the stable Pt-Zn alloy could not be removed unless a high oxidative potential was applied in an acidic solution. This may mean PtZn alloys are very stable under fuel cell operating condition, which could contribute to an increase in PEMFC lifetime.

2.7.2.5. Comparison of PtZn to other alloys

2.7.2.5.1. Pt-transition metal alloys

The stabilities of alloys are very important in the fuel cells. This statement applies to all other Pt-based alloys, such as Pt_3Co and Pt_3Ni, reviewed earlier [26]. When oxygen interacts with a bimetallic surface, generally surface segregation occurs in order for one of the alloy constituents to form a stable oxide on the surface. Zn forms oxide films very easily with a large negative heat of oxide formation; ZnO heat of formation: -83.17 Kcal/g mol as opposed to the heat of oxide formation of *e.g.*, RuO_2: -52.5 Kcal/g mol [113]. This may be some of the reasoning that many avoid using Zn as an admetal [114]. However, alloying effects similar to the one just introduced in the previous section have also been observed with popular Pt-based alloys, such as Pt_3Co [76], Pt_3Ti [115], PtMo [116], PtRu, and PtW [117]. All showed an increase in Pt *d*-orbital vacancies and also showed the decrease in the desorption temperatures in CO-TDS studies. The difference between such Pt-based alloys and PtZn is that Pt acts as an electron donor when alloyed to most of the transition metals, whereas Pt acts as an electron acceptor when alloyed to Zn. This may explain the difference in the trend observed with the Pt-Pt bond distance; *i.e.*, Pt-Pt bond distance in PtZn runs counter to other Pt-transition metal alloys; it increases in PtZn, but decreases in other Pt alloys [112]. It has been suggested that the contraction of the Pt-Pt bond distance is the key to the improved catalytic activity [118]. However, the elongation of the Pt-Pt bonds in PtZn is the result of shifting electrons from Pt-*d* orbital into the bimetallic bonding, contributing to the strength of Pt-Zn bonds. Shorter Pt-Pt bonds may thus be responsible for the instability of Pt-based alloys in fuel cells.

2.7.2.5.2. RuZn

RuZn and PtZn show a number of similarities in their effects of alloying. When Ru (001) and Zn form an alloy, similar changes in the electronic structure of both Ru and Zn have been observed as compared to the changes resulted by the formation of the Pt/Zn alloy [119]. According to ref. [120], the desorption temperature of Zn from the Ru surface increased by 250

K after alloy formation, as compared to the desorption temperature of Zn from Zn surface. This is a clear indication that the interaction of Zn-Ru is stronger than the Zn-Zn interaction – analogous to the Zn UPD layer formation on Pt. The core orbitals of Zn, namely Zn (3d) and Zn (3s), have also shown negative shifts in the binding energies when alloyed with Ru; both orbitals showed ~0.5 eV shift towards lower binding energies [121]. A CO-TDS study, carried out in UHV conditions, has also been reported [119, 120]. A sharp peak was observed on CO-TDS at 150 K which does not appear if CO is desorbed from Ru (001) surface. (For Ru (001), two broad peaks appear around the desorption temperatures of 400 and 500 K.) The peak at 150 K corresponds to CO desorbed from Zn. It should be noted that pure Zn does not adsorb CO under UHV conditions [112, 119]. Also, the broad peaks of CO desorbing from Ru shifts to lower desorption temperatures when Ru is alloyed to Zn. Also evidence of Zn-O bonding was not observed using Zn TDS, XPS for Zn (2$p_{1/2}$), and AES when oxygen and Zn ($\leq$ 1 monolayer) are coadsorbed [119]. The authors carried out theoretical calculations and showed that when adatoms are present on Ru, it induces mixing of s and p orbitals in the adatoms (Zn (4s,p) or O (2s,p)), producing a hybrid orbital that are oriented towards Ru atoms. This rehybridization in turn prevents Zn-O interactions [119]. We indeed observed the same behavior on our PtZn alloy, which will be shown in **Chapter 4**.

This example shows bimetallic bonding may result in significantly different characteristics from those of the pure components, which is principally the result of achieving the minimum energy for the bimetallic system. Predicting such changes is not straightforward, making bimetallic alloy research very interesting and challenging.

2.8. Summary

This chapter reviewed the current understanding of fuel cell catalysis, ORR and CO oxidation reaction mechanisms on Pt and Pt-based alloys and their adsorbate-induced surface reorganization, and PtZn alloy characteristics.

Fuel cells convert chemical energy into electrical energy in the MEA. The fuel cell reactions are kinetically sluggish and therefore catalysts are essential for its efficient operation.

The best catalyst for PEMFCs is Pt, which reduces oxygen in a direct pathway or in a series pathway. CO oxidation occurs by adsorption of CO and water on the Pt surface.

Pt-alloys are often employed to enhance the catalytic activities of fuel cell reactions and also to reduce the usage of Pt in MEA. They improve the kinetics of ORR by creating more vacancies in Pt $5d$ orbitals and by shortening the Pt-Pt bond distance in the alloy. CO oxidation is also enhanced for Pt alloys via a bifunctional mechanism and/or ligand effects. Chemical stability of the Pt alloys in an acidic environment of fuel cells is, however, still a serious issue.

Adsorbates on metal surfaces often induce surface reorganization or segregation. The presence of adsorbate changes the surface energy, leading to restructuring of atoms to restore the lowest energy. Segregation of one component of the alloy may occur due to a thermochemical effect.

PtZn alloys are prepared after the formation of a Zn UPD layer onto Pt, followed by spontaneous transformation to an alloy. The alloy also showed an increase in Pt-$5d$ vacancy, but Pt-Pt bond distance increased. Instead, Pt-Zn bond distance is much shorter than the Pt-Pt or Zn-Zn bond, suggesting the strong bimetallic bonds. This may indicate good chemical stability in acidic conditions such as found in an operating fuel cell.

3.   Materials And Methods

3.1. Introduction

This chapter describes experimental methods and techniques employed in this thesis. Since fuel cells are electrochemical devices, and electrochemistry is a surface phenomena, voltammetry and instrumental surface analysis were the two major methods used to characterize the catalyst surface. Fundamental theories of the electrochemical double layer, electron transfer and adsorption isotherm have been described in **Chapter 2.** This chapter details the experimental methods used for the experiments. Analytical instruments used in the experiments are: Auger electron spectroscopy (AES), scanning electron microscopy (SEM), energy dispersive X-ray spectroscopy (EDX), and inductively-coupled plasma mass spectrometry (ICP-MS). The principles of operation for each of the instruments are briefly described.

3.2. Electrochemistry

In this section, the electrochemical technique and general instrumental setup are described. Voltammetry was extensively used. The method for the electrochemical formation of PtZn electrodes is outlined. They were made on bulk Pt substrates and used for kinetic data analysis. When polarization curves were recorded for kinetic analysis, rotating disc electrodes (RDEs) were used. The principle of the RDE operation is summarized, and the data analysis method is also presented.

3.2.1. Rotating disc electrodes

Rotating disc electrodes consist of a disk of metal Pt attached to a cylindrical conductive material (*e.g.,* stainless steel) shielded in an insulating material. A schematic view of the RDE is shown in **Figure 3-1**. The RDE is connected to a motor and rotates at a specific speed to actively transport reactants towards the surface of the electrode. Flow of the electrolyte caused by the rotation is shown in **Figure 3-2**. In this figure, r is the lateral axis and z is the longitudinal axis [122]. The rotation speed is often expressed in *rotations per minute* (rpm), which could be converted into the rotational frequency, ω (in sec^{-1}):

$$\omega = \frac{(rpm) \times 2\pi}{60 \, sec}$$

(3-1)

The thickness of the stagnant solution near the surface of the disc electrode is called the hydrodynamic boundary layer thickness, and when the electrode rotates at 2000 rpm in an aqueous solution, it is roughly 250 μm thick (in z direction) at 25 $^{\circ}$C. Therefore, the current is determined by the flux at the electrode surface due to the diffusion of reactant, *o*, to the metal/solution interface through the boundary layer:

$$i = nAFD_o \left(\frac{\partial C_o}{\partial z} \right)_{z=0}$$

(3-2)

where D$_o$ is the diffusion coefficient of species *o* in cm^2/s, A is the area of the electrode, and C$_o$ is the concentration of *o*. The partial derivative of C$_o$ with respect to z is the flux of species *o* very close to the electrode surface. When the current is limited by mass transfer, which will be denoted as i_l,

$$i_l = 0.62nFA \, D_o^{2/3} \omega^{1/2} v^{-1/6} C_o^*$$

(3-3)

known as the *Levich equation*. The term, v, is a kinematic viscosity (ratio between viscosity and density of a solution) [9].
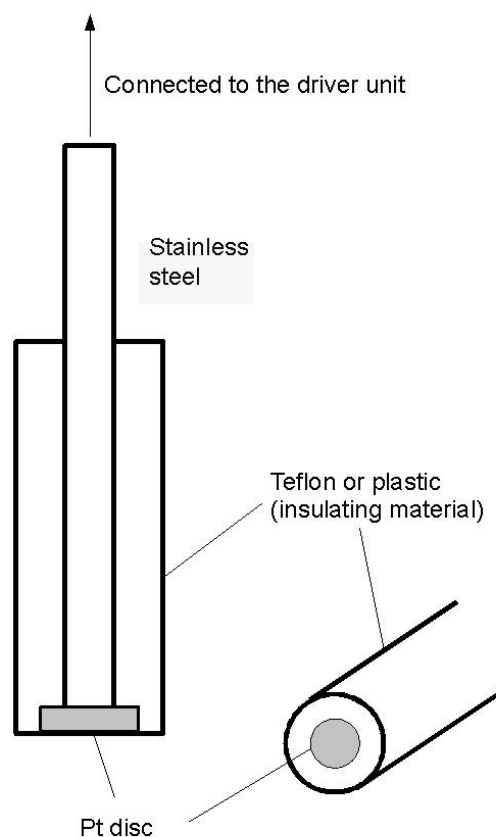
Figure 3-1 Schematic view of a rotating disk electrode (bottom view on the right and the cross section on the left). A disk of metal (*e.g.,* Pt) is connected to a stainless steel shaft and shielded in a Teflon or plastic insulating material. The RDEs employed in this thesis had the Pt disc diameter of 3 mm (total diameter of the electrode is 10 mm)
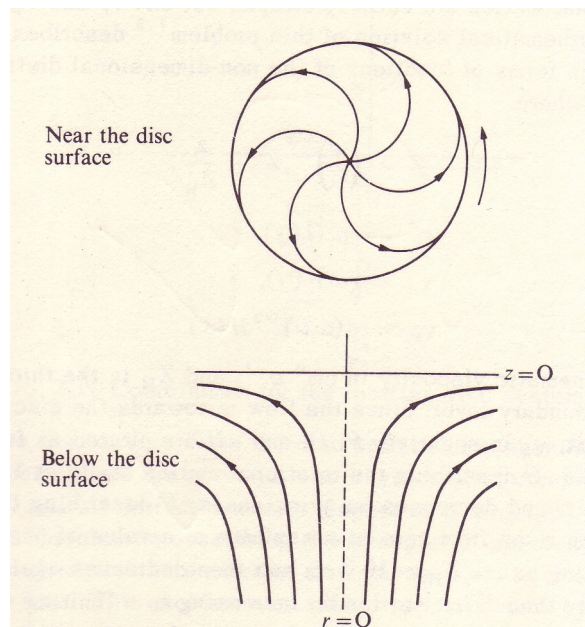
Figure 3-2 Hydrodynamics at the surface of an RDE. Reprinted in part with permission from [122]. Copyright 1971 Oxford University Press.

3.2.2. Kinetic and mass transport-limited current relationship for RDE

Current observed in polarization curves can be classified into two categories: kinetic current, i_k, and mass-transfer-limiting current, i_l. Kinetic current is the current determined by the kinetics of the reaction at the applied potential whereas the mass transfer-limiting current is the current determined by the flux of species to the electrode. The total current is obtained by,

$$\frac{1}{i} = \frac{1}{i_k} + \frac{1}{i_l} = \frac{1}{i_k} + \frac{1}{0.62 \text{nFAD}_o^{2/3} \omega^{1/2} \nu^{-1/6} C_o^*} \tag{3-4}$$

This equation is known as *Koutecky-Levich* equation. The limiting current is readily determined from experimental data, and the kinetic current is deduced by plotting i^{-1} vs. $\omega^{-0.5}$. Rearranging the equation, kinetic current can also be determined by,

$$i_k = i\ \frac{i_l}{i_l - i} \qquad\qquad (3\text{-}5)$$

With this equation, the kinetic current at a certain rotational speed is deduced [123]. In **Chapter 4,** we will use the kinetic current to construct the ORR Tafel plot. Kinetic current was calculated using in-house developed LabView program. In this calculation, the values of 1.97×10^{-5} cm^2/s and 0.01014 cm^2/s were used for the diffusion coefficient of oxygen in water at 25 $^{\circ}$C and the kinematic viscosity of the 0.1 M H_2SO_4 solution at 20 $^{\circ}$C [113]

3.2.3. Cyclic voltammetry

Cyclic voltammetry is an electrochemical technique where the potential of the electrode is linearly scanned between two fixed potentials at a certain sweep rate (in V/sec) while the current is continuously monitored. This is very commonly used to characterize the redox couple of an electrode/electrolyte system. Current measured with respect to the applied potential is plotted, and this graph is called cyclic voltammogram (CV).

3.2.4. Anodic stripping voltammetry

Anodic stripping voltammetry (ASV) is an electrochemical technique involving preconcentration of substance in electrolyte by applying a reductive potential to the electrolyte, followed by stripping (or re-dissolution) of the substance by sweeping the potential to the anodic (oxidative) direction. The scheme of anodic stripping voltammetry is shown in **Figure 3-3**. In the figure, i_p denotes the peak current where the preconcentrated substances are oxidized and E_p denotes the corresponding potential. E_p could be predicted by the Nernst equation if the redox couple is reversible, and this potential is unique to each substance. It is also possible to

determine the concentration of the corresponding substance in solution by constructing a calibration curve. In this work, ASV will be used in **Chapter 5** in order to investigate the carbon monoxide (CO) oxidation catalysis. E_p of CO stripping voltammetry is greatly affected by the type of catalyst (electrode material), and the characteristics of the surface, thereby the efficiency of the catalyst is compared by measuring the peak potential, E_p [9]. In **Chapter 6** ASV was also used to determine the concentration of Zn in the solution where prolonged polarization of PtZn was performed.

3.2.5. Differential pulse voltammetry

The differential pulse method is commonly used with anodic stripping voltammetry where a trace amount of analyte metal ions is present in the test solution (typically sub-micro molar level). The potential profile with respect to time is shown in **Figure 3-4**. A deposition potential is applied to the working electrode, and after the species of interest is concentrated on the surface of the electrode, the potential pulse (modulation amplitude) is applied as shown in the diagram. The current is recorded at S_1 and S_2. The difference between the two is recorded as a function of the average applied potential. If both potentials are far from the reversible potential, E_{Nernst}, the currents measured are similar, giving the difference in measured current at S_1 and S_2 approximately zero. Only when the potential approaches E_{Nernst}, the difference between the faradaic current at the two points becomes significant which results in a peak in the voltammogram ($[i(S_2)-i(S_1)]$ vs. applied potential). This technique is more sensitive and useful in trace elemental analysis compared to linear sweep voltammetry [9].

The differential pulse method, together with ASV, is used in **Chapter 6** to determine the concentration of Zn in an acidic solution.
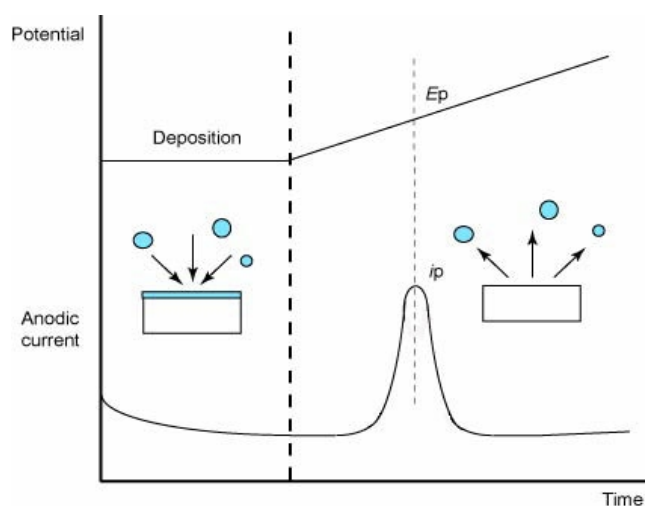
Figure 3-3 Potential and current profiles with respect to time in anodic stripping voltammetry. Analyte in a solution is first preconcentrated at a deposition potential, followed by stripping (oxidation) of the deposited film by scanning the potential in the anodic direction, resulting in a peak in a voltammogram. The peak potential, E_p can be calculated by the Nernst equation, and the current, i_p is measured. Because of the preconcentration step, the sensitivity of detection is enhanced, making this method suitable for trace metal analysis (< 1 μM).
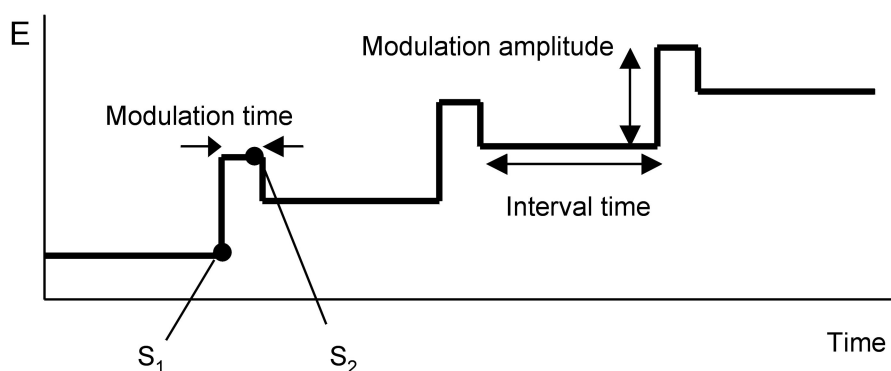
Figure 3-4 Potential profile with respect to the time in differential pulse method. Potential is applied to the electrode for a certain period ("*interval time*"; typically 0.5~4 seconds), a potential step ("*modulation* amplitude"; typically 10~100 mV) is applied to the electrode and fixed at the stepped potential for some period of time ("*modulation time*"; typically 5-100 milliseconds). Current is measured just before the step and just before the potential is stepped back to the base (at S_1 and S_2, respectively), and the difference is plotted as a function of potential.

3.2.6. Electrochemistry – experimental consensus

Electrochemistry generally requires stringent experimental conditions. This section explains the general aspects of electrochemical setups that apply to all electrochemical experiments performed in this thesis. Cleanliness of the experimental systems was very important, and ensuring no organic or inorganic contaminants was crucial for meaningful results. Glassware used in all the experiments throughout this thesis were first soaked in a warm 1:1 (by volume) concentrated sulfuric acid and nitric acid for at least 2 hours, followed by rigorous rinsing with Milli-Q water (Millipore, Billerica, MA). The Milli-Q system uses reverse osmosis and ion exchange cartridges to deionize the water, followed by UV light exposure to photolyze organic contaminants, providing clean water with high resistivity (>18.2 MΩ cm), low total oxidizable carbon (< 1 ppb), and pH of 5. The quality of water was ensured by following the set schedule for replacing filters provided by Millipore.

There are mainly two types of electrolyte used in this thesis: 0.1 M sulfuric acid (SeaStar Baseline® 93-98% purity with impurities in ppt levels) and 0.1 M zinc sulfate solution (Fluka, puriss p.a. ACS grade, low Cl), both made with Milli-Q water. The reference electrode (RE) was a home-made reversible hydrogen electrode (RHE; 0 V vs. standard hydrogen electrode, SHE), unless otherwise stated. Potentials reported in this thesis are measured with respect to RHE. A drawing of the RHE is shown in **Figure 3-5**. A small compartment at the bottom of the electrode contains a coiled Pt wire which is soldered to an extended tungsten wire. The compartment is filled with an acidic solution from the opening at the tip of the electrode. The tip is then immersed into an acid solution together with a gold wire. The electrode and the wire can then be connected to a 9 V alkaline battery to evolve hydrogen at the Pt wire in the compartment to create a bubble of hydrogen gas, which establishes equilibrium between protons and H$_2$ (g) around the Pt wire, acting essentially like a standard hydrogen electrode. The top of the compartment is well-sealed to avoid a hydrogen gas leakage. Hydrogen gas bubble was freshly formed at the beginning of every experiment, but the electrode was usually stable for 2 to 3 days once generated. RHE was connected to an electrochemical cell through a salt bridge. The counter electrode (CE) was a coiled Pt wire, cleaned by heating in a butane-air flame for 1 minute followed by rinsing with water. The working electrode (WE) was either an RDE or a Pt bead. A diagram of the electrochemical cell is shown in **Figure 3-6**. The RDEs employed in this

work had the disk diameter of 3 mm (geometrical area of 0.071 cm^2), with the electrode diameter of 10 mm. The RDEs were cleaned in a mixture of diluted HNO_3 and 30 % H_2O_2, and the Pt bead was cleaned by heating it in a butane-air flame, followed by rinsing with Milli-Q water.

Approximately 70 to 80 mL of electrolyte was placed in an electrochemical cell, and the solution was first deaerated using Ar gas (99.9995 % purity; Praxair). Solution cleanliness in the sulfuric acid solution was assessed by recording a CV with a Pt electrode between potentials of 0.03 and 1.3 V at sweep rate of 50 mV/s, which is shown in **Figure 3-7**. Hereafter, CVs recorded in this manner is designated as "Ar saturated CV" or CV, unless otherwise stated. Hydrogen adsorption and desorption peaks (the potential region of 0~0.3 V) are particularly sensitive to the presence of contaminants. CVs would appear distorted or show diminished or extra peaks if they are present. The characteristic shape of a clean Pt CV was always ensured before proceeding, otherwise the cell was brought back to the acid bath for a complete cleaning.
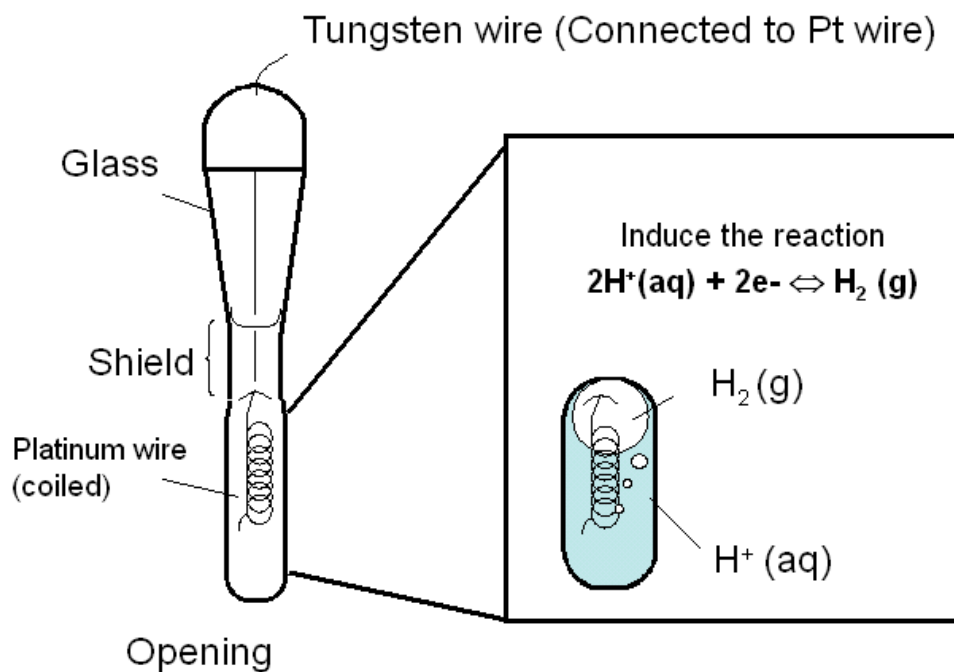
Figure 3-5 Home-made reversible hydrogen electrode (RHE). A small compartment at the bottom of the electrode contains a coiled Pt wire which is connected to the extended tungsten wire. The compartment is filled with an acid solution from the opening at the tip of the electrode. Hydrogen gas is evolved in the compartment, resulting in the Pt wire in equilibrium with hydrogen gas and protons in solution. This acts as a hydrogen electrode.
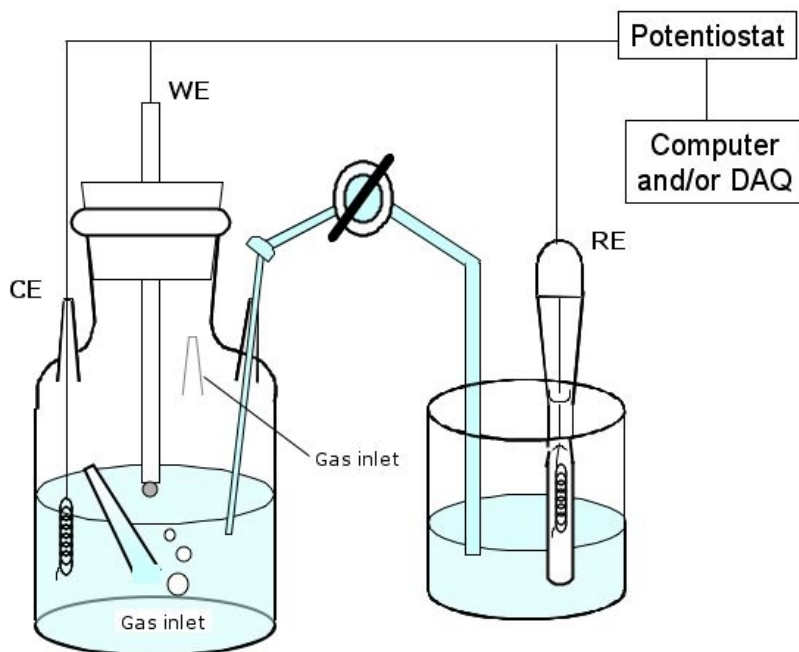
Figure 3-6 Schematic view of electrochemical cell. The counter electrode (CE) was a coiled Pt wire and the reference electrode (RE) was typically the RHE. The working electrode (WE) and other electrodes were connected to potentiostat which was computer controlled.
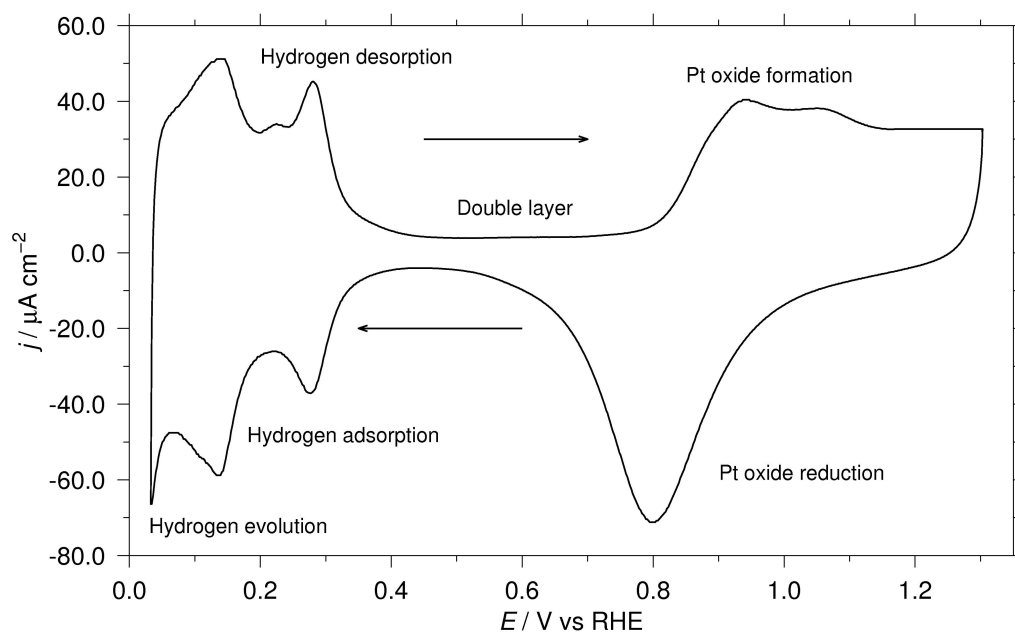
Figure 3-7 A cyclic voltammogram of polycrystalline Pt recorded in 0.1 M H$_2$SO$_4$ deaerated solution at the scan rate of 50 mV/s is presented. Integration of hydrogen adsorption or desorption peaks give approximately 210 μC/cm^2 of charge density. This is used as a benchmark CV recorded in a clean H$_2$SO$_4$ solution.

3.2.7. PtZn alloy formation

PtZn electrodes were prepared by electrochemically depositing bulk Zn onto interchangeable Pt RDE or Pt bead electrodes. As mentioned in **Chapter 2**, Zn-modified Pt can quickly transform into a PtZn alloy at a room temperature without a rigorous treatment. The formation of PtZn on a bulk Pt substrate (*i.e.,* a Pt rotating disc or a Pt bead electrode) is described in this section.

3.2.7.1. Zn deposition and PtZn alloy formation

The Zn electrodeposition (0.1 M $ZnSO_4 \cdot 7H_2O$) was carried out in an electrochemical cell on a Pt RDE (Metrohm, Switzerland) or on Pt bead electrodes (99.99 % GoodFellow). The Pt beads were prepared by melting one end of a Pt rod with an acetylene torch, then polishing, starting with 1200 grit sandpaper, then successive grades of diamond slurry ending with 1 μm diamond slurry (Leco, MI). The electrodes were connected to a potentiostat (μAutolab, EcoChemie), and electrochemical measurements were performed at room temperature (22 ± 2 ^{o}C). Initially, a CV of the Pt electrode in the $ZnSO_4$ electrolyte was recorded and the bulk Zn desorption potential was determined (*i.e.,* the equilibrium potential for Zn reduction). The potential of the Pt electrode was set 50 mV negative of the onset of the Zn deposition, and bulk Zn was deposited, during which the current transient was recorded. The electrode was removed from the electrolyte after 300 seconds of Zn deposition, and the Pt/Zn alloy was allowed to form under Ar atmosphere at room temperature for 1 hour. Excess (nonalloyed) Zn was stripped off the Pt electrode by immersing the electrode back into the Zn electrolyte and polarizing to a potential positive of the Zn stripping potential measured in the initial CV. The electrode was then dipped into a diluted HNO_3/H_2SO_4 solution to ensure all unalloyed Zn (in either metallic or hydroxide form) was removed. However, when the amount of charge passed during the stripping process was not measured, unalloyed Zn was simply removed by immersing into a concentrated 1:1 acid mixture of HNO_3 and H_2SO_4. An Ar saturated CV for PtZn was then recorded between 0.03 V and 1.0 V at 50 mV/s and compared to that for Pt. The kinetic current analysis was then performed and compared to the pure Pt.

It is important to note that the PtZn electrode was used as prepared without polishing the surface as the alloy formed is in the surface region, therefore polishing would likely remove it. However, the deposition of Zn and subsequent alloy formation substantially roughens the surface of the Pt substrate. As shown in **Chapter 2**, roughness of the catalyst surface influences the measured activity. Surface roughness of the both the Pt and PtZn electrode was determined for comparison of the electrochemical activity in **Chapter 5**.

3.3. Analytical instrumentation

Several analytical instruments were used for surface characterization of selected electrode surfaces or for the determination of trace metal concentration in a solution to supplement the electrochemical observations. Surface and/or elemental analysis instrumentation used were Auger electron spectroscopy, scanning electron microscopy, and energy dispersive X-ray spectroscopy. Trace metal analysis was performed on inductively coupled plasma – mass spectroscopy. The principle of operation for each instrument is briefly described in this section.

3.3.1. Auger electron spectroscopy

3.3.1.1. Operation principles

Auger electron spectroscopy (AES) is a powerful surface analytical technique based on the Auger process discovered by Pierre Auger in 1923 [124]. It probes the first 2~10 atomic layers (*i.e.*, up to 10 Å) of conducting samples in a ultra high vacuum (UHV; typical pressure of $10^{-9} \sim 10^{-11}$ mbar) environment. The sampling depth of the Auger process into the surface is depicted in **Figure 3-8** [124]. AES is used in this thesis to identify the surface chemical composition of electrode surfaces. The Auger process is shown schematically in **Figure 3-9**. The core electron of an atom is first ejected by the incoming electron beam (Process 1; the typical energies of the incident beam is 3~30 keV), which creates a hole in the inner orbital of energy, E_W. This hole is filled by an electron in an upper orbital with energy, E_X. This process can transfer the energy to valence electrons, whose energy is E_Y, which can then be emitted from the atom. This electron is called a secondary electron or an Auger electron. The kinetic energy of the Auger electron (generally from 50~3000 eV) is therefore determined by,

$$E_{WXY} = E_W - E_X - E_Y - \Phi_e \tag{3-6}$$

where Φ_e is the work function of the sampled atoms. The energies of E_X and E_Y may be a little

more negative than their original values as removing electrons takes place after a core electron has been ejected. Since E_{WXY} measured is unique to each element, an Auger spectrum provides a fingerprint of atoms present on the sample surface.

Quantitative analysis of relative atomic composition of surfaces is also possible by integrating the Auger spectral peaks. The intensity contribution (*I*) for Auger electrons emitted from the sample is,

$$I = m \, f \, \sigma \, \lambda \, A_{eject} \, T_{inst}$$
(3-7)

where m is the number of atoms per unit volume of the sample, f is the flux of the incident electrons, σ is the cross section of the Auger process, λ is the inelastic mean free path (*i.e.,* the distance an electron can travel without losing its energy), A_{eject} is the area of the sample where the electrons are ejected, and T_{inst} is the instrumental constant describing transmission efficiency of the electron analyzer. Contributions from f, σ, A_{eject}, and T_{inst} can be grouped into an instrumental coefficient, B, for given instrumental conditions and a given peak. This term is called a *sensitivity factor.* Atomic ratio for two elements in the sample (*i.e.,* m_1/m_2) is determined by,

$$\frac{m_1}{m_2} = \left[\frac{(I_1/B_1)}{(I_2/B_2)} \right] \left(\frac{\lambda_2}{\lambda_1} \right)$$
(3-8)

The ratio of the inelastic mean free paths is often assumed to be unity, therefore the atomic ratio of two elements can be estimated by the intensities of Auger peaks and the sensitivity factors [125]. Elemental sensitivity factors are often measured relative to clean Ag, but the method often introduces instrumental uncertainties to the measured quantities [124]. However, we were fortunate to measure our own sensitivity factor for Zn relative to Pt ($B_{Zn}=3.625$, $B_{Pt}=1$). We obtained clean Pt and Zn metals present on the same sample substrate. This will be detailed in **Chapter 4**.
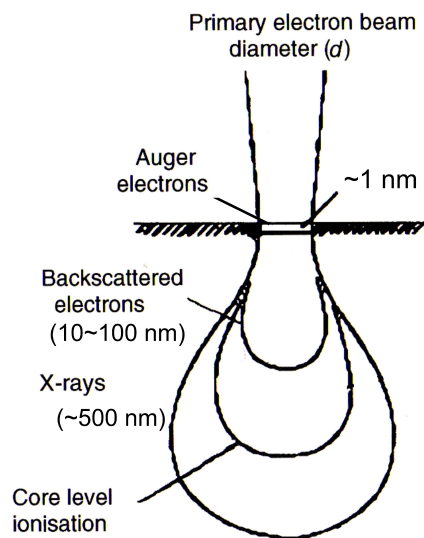
Figure 3-8 Distribution of electrons in various analytical techniques. Auger electrons, backscattered electrons, X-ray (fluorescence in EDX) were analyzed in this thesis. Adapted from [124]. Incident electrons (beam diameter of ~ 10 nm) impinge on the solid surface and penetrate causing various types of excitation of the atoms in the sample. Typical path lengths for the excitation phenomena are shown in the figure.
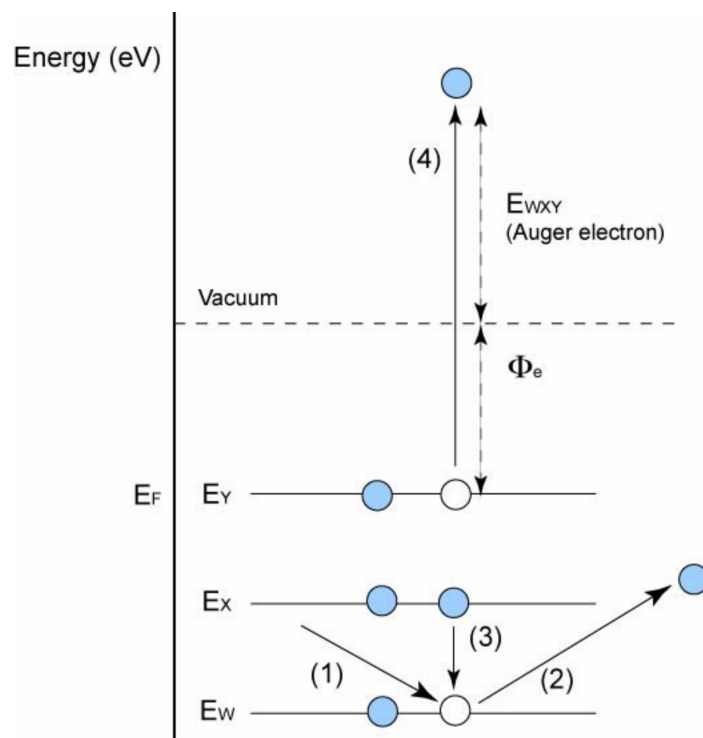
Figure 3-9 Auger electron transition. Incident beam hits the core electron in E_w in (1 and 2) followed by the relaxation of an electron in the upper orbital, E_x (3). This relaxation provides enough energy to the electron in E_Y to be ejected as an Auger electron. Φ_e is the work function and E_{WXY} is the energy of Auger electron, which is typically 50~3000 eV.

3.3.1.2. Nomenclature of Auger transition

Auger transitions and the corresponding peaks in the spectrum are expressed as, *e.g.,* "KLL" or "LM$_2$". These notations are often used in X-ray spectroscopy, and each letter corresponds to an electronic state of the atom. The first of three letters in the former example denotes the core level, the middle one corresponds to the orbital from where an electron falls to fill the core hole, and the last describes the orbital from where the Auger electron is emitted. The notations are correlated to quantum numbers, *i.e.,* principal quantum number, *n*, orbital, *l*, spin, *s*, and spin-orbit coupling, *j*. Examples of *j-j* coupling notations in X-ray spectroscopy is given in **Table 2-1** [126]. The middle energy level is often dropped, and the orbital where Auger electron is ejected is specified (the latter example).

Table 2-1 Auger notations. Different electronic states are expressed in terms of their quantum numbers, *n*, *l*, and *j* [126].

Quantum numbers			Suffix	X-ray level	Spectroscopic level
n	*l*	*j*			
1	0	1/2	1	K	$1s_{1/2}$
2	0	1/2	1	L$_1$	$2s_{1/2}$
2	1	1/2	2	L$_2$	$2p_{1/2}$
2	1	3/2	3	L$_3$	$2p_{3/2}$
3	0	1/2	1	M$_1$	$3s_{1/2}$
3	1	1/2	2	M$_2$	$3p_{1/2}$
3	1	3/2	3	M$_3$	$3p_{3/2}$
3	2	3/2	4	M$_4$	$3d_{3/2}$
3	2	5/2	5	M$_5$	$3d_{5/2}$
4	0	1/2	1	N$_1$	$4s_{1/2}$
4	1	1/2	2	N$_2$	$4p_{1/2}$
					...etc.

3.3.2. Secondary (Scanning) electron microscopy

3.3.2.1. Scanning electron microscopy (SEM)

Often surface analytical instruments are equipped with a secondary electron detector which detects the electrons with kinetic energy less than 50 eV. Because these low-energy electrons emerge from the surface, they are used to form a micrograph (known as secondary or scanning electron micrograph; SEM) to give morphological images of the sample. Secondary electrons are collected in the photomultiplier detector as the incident electron beam scans the sample surface. The brightness of the image depends on the nature of the atoms on the surface; if the sample is grounded properly, a steeper surface gives brighter contrast than a flat surface. Also, heavier atoms emit secondary electrons more readily than lighter ones. The advantage of having SEM together with AES or EDX is the ability of obtaining Auger spectra from regions of different morphologies. This technique was particularly useful as shown in **Chapter 4** when we found three distinguishable regions on our Zn-modified Pt electrode [127].

3.3.2.2. Backscattered electron (BSE) imaging

When an incident electron beam hits a sample surface, some of electrons are backscattered without losing significant amount of energy. The number of such electrons varies with atomic number of the atoms near the surface, as well as topography. The penetration depth of backscattered electrons is much deeper relative to the Auger electrons, according to **Figure 3-8**. Heavier atoms on the surface backscatters more electrons, hence the resultant image appears brighter, and vice versa. Backscattered electrons travel with high velocities to the four quadrants (solid-state silicon-based detectors) that are located above the sample. Electrons collected at two quadrant pairs, A and B, can either be processed as an A+B mode or an A-B mode. The former sums all signals collected in A and B to generate an image based on the atomic number contrast present on the surface. The latter mode subtracts the signals in B from A to generate a topographical contrast of the surface where contour features are better enhanced [127].

BSE was useful in **Chapter 5** where the distribution of Zn in the Pt substrate was examined. The presented image was recorded using the A+B mode.

AES used in this thesis was Microlab 350 (Thermo Electron Co.), equipped with secondary electron detector, concentric hemispherical analyzer (separate electrons by their kinetic energies), and a backscattered electron detector. All Auger spectra, some SEM images, and all BSE images presented in this thesis were recorded in this instrument. Incoming electron beam was 10 keV with the primary electron beam diameter less than 10 nm. The detection limit of the instrument is 0.2 atomic %. Resolution factor (constant retardation rate) of 4 was used, unless otherwise stated. This instrument was operated by Dr. Philip Wong in Department of Chemistry, University of British Columbia.

3.3.3. Energy dispersive X-ray spectroscopy

When the process (3) in **Figure 3-9** occurs, atoms can also lose energy by emitting a photon in a process called X-ray fluorescence, and observing these photons provides the basis of another chemical analysis technique, known as energy dispersive X-ray spectroscopy (EDX). Because the inelastic mean free path (*i.e.,* the distance electrons or photons can travel before losing their energies) is relatively long (typically ~0.5 μm), EDX is used for the bulk elemental analysis. Auger electron emission and X-ray fluorescence are competing processes; the former dominates when the initial vacancy created by the incoming electron beam has a binding energy of less than 2000 eV, which is often the case for lighter atoms. The latter dominates otherwise. We also used EDX for PtZn compositional analysis.

Quantitative analysis is also possible. This is done by determining the area under the spectral peaks after correcting for a non-linear background. Compositions of elements in the analyzed metal were reported relative to one another [128].

EDX employed in this thesis was a S3000N SEM (Hitachi; available in Department of

Materials Engineering at University of British Columbia). The instrument was equipped with a tungsten hairpin source that produces electrons by thermoionic emission. Incident electron beam was 20 keV. All EDX spectra and some SEM images were recorded on this instrument. The detection limit of the instrument is 0.1 weight %.

3.3.4. Inductively coupled plasma – Mass spectrometry

Inductively-coupled plasma (ICP) is a commonly used ionization source, generated by passing noble gases, typically Ar, through a high frequency electromagnetic field. When a spark is introduced to the stream of Ar gas, electrons are stripped from some of the atoms. The electrons collide with other Ar atoms producing further ionization. The energetic collisions are also responsible for the high temperature of the plasma (6000 ~ 10,000 K). The sample solution is injected into the flow of plasma where it can be desolvated, vaporized, atomized, and partially ionized. Charged elements are readily analyzed in a mass spectrometer with the detection limit of sub-ppb level. The first ionization energies of Pt and Zn are 9.0 and 9.391 eV, respectively [113] which can be partially (40~60 %) achieved by Ar plasma [129, 130].

In **Chapter 6**, we created PtZn nanoparticles on a glassy carbon substrate. To determine the bulk composition of the particles, we dissolved them into aqua regia (1:3 HNO_3 : HCl), and the solution was analyzed in the ICP – mass spectrometry (ICP-MS) available in the Department of Chemistry undergraduate physical/analytical teaching lab at University of British Columbia (Elan model 6000; mass range of 3-270 amu with resolution of 0.05 amu). The stoichiometric ratio between Zn to Pt was obtained. The instrument employed in this thesis consists of a quartz ICP torch with three-stage pumping system coupled to a quadrupole mass analyzer and electron multiplier tube as a detector. The instrument is controlled by the commercial software.

3.4. Single fuel cell

The PtZn alloy was tested both in an electrochemical setup and in an actual fuel cell setup in **Chapter 4**. PtZn membrane electrode assembly (MEA) was created just as PtZn RDEs were formed; by electrochemical Zn deposition over Pt-dispersed MEA. This is a rather unique method to create Pt-alloy MEAs and is also readily performed in a laboratory. This section describes the experimental method of preparing a PtZn MEA and hot-pressing the MEA into a single stack fuel cell.

3.4.1. MEA fabrication

The MEA consists of solid electrolyte (50~175 μm) in the middle, sandwiched by two catalyst layers (5~50 μm) which are applied onto gas diffusion layer (GDL) backings (100~300 μm) [2]. Catalyst layers usually consist of nanoparticles of catalyst, typically Pt, supported on carbon particles, which are often denoted as Pt/C. Schematics of the MEA are shown in **Figure 3-10**. At both ends of the GDLs, flow field plates are attached to complete the unit. Flow field plates have numerous grooves, called flow channels, where gases (either a fuel or an oxidant) flow and reach to the electrode surfaces. The solid electrolyte and catalyst layers and/or catalyst layers with the GDLs are often hot pressed at elevated temperature and pressure (typical values of 120-160 $^{\circ}$C at 5000~15000 kPa, respectively [131]). Hot pressing is another important process that impacts fuel cell performance as forming poor bonds between the catalyst layer and a membrane electrolyte or GDL backings lead to high contact resistance which would act to increase any type of polarization. In **Chapter 4**, we describe the preparation of an MEA by hot pressing commercially available carbon supported Pt already attached to a GDL with Nafion^{TM} membrane. Although MEA fabrication methods are not the focus of this thesis, different preparation modes of MEA significantly alters the performance of PEMFCs [132, 131]. In that chapter, we used Nafion^{TM} solution sprayed between GDL and electrolyte membrane before hot pressing to ensure good bonding and ionic conductivity. This would create a thin layer of membrane over Pt/C which has shown better performance than *e.g.,* Pt/C directly attached to

membrane without the coating layer [2]. The cross-section of the MEA thus fabricated is shown in **Figure 3-11** [133].

In **Chapter 4**, the MEAs were prepared with and without the Zn treatment of the dispersed Pt cathode. The gas diffusion cathode consisted of a 5 cm^2 ELAT carbon cloth backing layer (Electrochem Inc.) with 1 mg cm^{-2} Pt supported on Vulcan XC-72 (*i.e.*, 20 wt % Pt on the carbon support). The Zn treatment of the gas diffusion cathode was similar to the procedure employed for the Pt RDE described previously. Zinc modification of the cathode layer was accomplished by immersion of the cathode in 0.1 M $ZnSO_4$ in the main compartment of a two-compartment glass cell along with the stainless steel counter electrode and a Hg/Hg_2SO_4 reference electrode (-0.64 V vs. RHE in saturated KCl). A CV was performed measuring the Zn deposition and stripping currents. The picture showing the electrochemical Zn deposition on the GDL is shown in **Figure 3-12**. The potential of the gas diffusion cathode was set to -0.95 V vs. RHE for 5 min and the current transient recorded. The cell was turned off and the alloy was allowed to form for 20 min. The cell potential was then set to -0.3 V and the bulk Zn was stripped off as indicated by the anodic current recorded. The modified cathode was rinsed with Milli-Q water and was stored in air until the MEA was pressed.
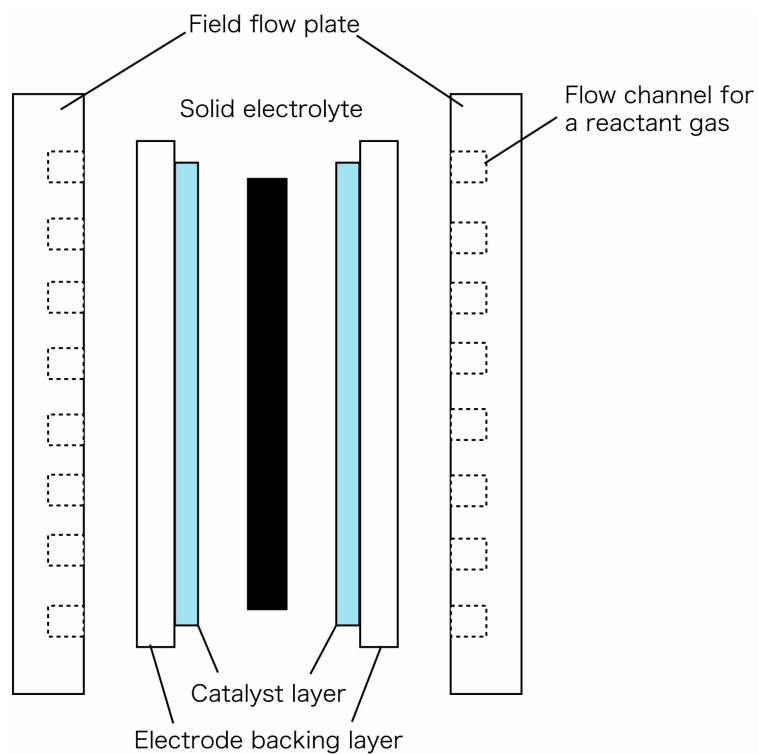
Figure 3-10 The components of MEA are shown. Solid electrolyte is sandwiched between two catalyst layers that are attached to GDLs. These units are hot pressed to form a MEA. It is further sandwiched by field flow plates which are responsible for delivering reactant gases to the catalyst layers.
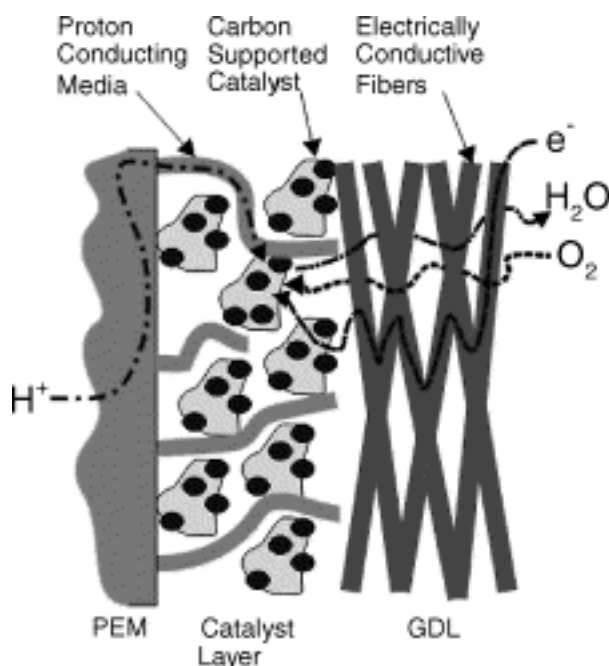
Figure 3-11 Cross section of solid electrolyte, catalyst layer, and GDL hot pressed together with Nafion™ bonding ("proton conducting media" in the figure). Better ionic conduction and electron transfer are achieved by having the conducting media supporting the catalyst layer. Cross section of solid electrolyte, catalyst layer, and GDL hot pressed together with Nafion™ bonding ("proton conducting media" in the figure). Better ionic conduction and electron transfer are achieved by having the conducting media supporting the catalyst layer. Reprinted from [133]. Copyright 2004 with permission from Elsevier Ltd.
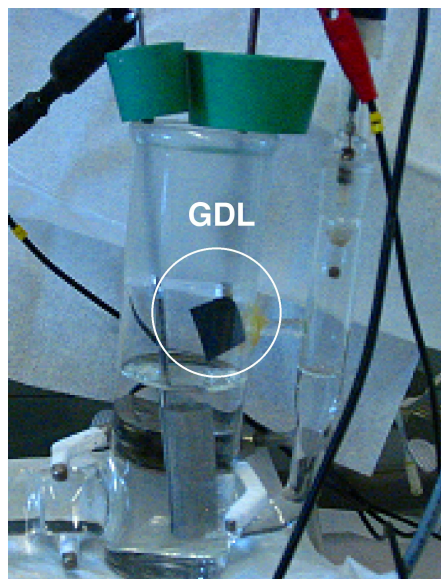
Figure 3-12 Electrochemical setup to perform Zn modification onto a catalyst-attached GDL. GDL was connected to potentiostat and immersed into a $ZnSO_4$ solution. The counter electrode was stainless steel mesh and the reference electrode was Hg/Hg_2SO_4.

Following the Zn modification of the cathode, the full MEA was assembled by hot pressing the gas diffusion cathode to the Nafion™ 115 membrane (127 μm dry thickness). The anode, consists of 5 cm^2 ELAT carbon cloth with 1 mg cm^{-2} Pt supported on Vulcan XC-72, was commercially available with a pre-pressed membrane on one side (Electrochem Inc.).

To ensure good bonding between the cathode and the membrane and to impart ionic conductivity to the cathode catalyst layer, a few drops of Nafion™ solution (5 wt % in lower alcohols, Aldrich Inc.) were uniformly dispersed on the side of the cathode facing the membrane, giving a cathode Nafion™ load of about 1 mg cm^{-2}. The hot pressing of the cathode to the half-MEA was performed at 115 ^{o}C, under a weight of 800 lbs applied for 60 sec.

Single cells were assembled using Au-coated end plates (9 cm × 9 cm) with serpentine

flow field pattern (Electrochem Inc.). Fuel cell tests were carried out employing the Greenlight test station at the Institute for Fuel Cell Innovation of the National Research Council of Canada, located in Vancouver, BC.

3.5. Summary

This chapter describes the method and materials used to carry out the experiments and to process the data thus acquired. Electrochemistry of RDEs was reviewed. Most of the electrochemical work presented in this thesis depends on voltammetry, and the techniques used were described. Also the method to form PtZn electrodes are presented. Bulk Zn layers were deposited over Pt electrode surface, and the alloy was spontaneously formed.

Analytical instruments, namely AES, SEM, EDX, and ICP-MS, were also extensively used for elemental analysis and the quantification in order to supplement the electrochemical data. The principle of operation in each technique was also presented.

Finally, the method to create a single-stack fuel cell was described. PtZn MEAs were formed in the same manner as PtZn electrodes were prepared. The resultant MEAs are hot-pressed into a complete fuel cell unit.

4.   Oxygen Reduction Reactions on Pt and PtZn

4.1. Introduction

The oxygen reduction reaction (ORR) occurs on the cathode in a proton exchange membrane fuel cell (PEMFC). Its sluggish kinetics is the source of a large fraction of the loss of power in fuel cell operation. Significant research efforts are actively pursuing a better catalyst for the ORR, or trying to reduce the amount of Pt catalyst needed for fuel cell operation. The biggest challenges that face the fuel cell industry are to increase the activity per mass of the dispersed Pt in current state of the art fuel cells by an order of magnitude through improved utilization of the dispersed Pt, or by improving the kinetics of the ORR. Increasing the kinetic rate of ORR is observed through alloying of the Pt metal with various transition metals, which borrows from the experience with alkaline fuel cells. The modification of the Pt catalyst through alloying has met with varying degrees of success in terms of decreasing the ORR overpotential as introduced in **Chapter 2**. Many transition metals have been alloyed with Pt, and the kinetics of the ORR has been measured using the rotating disk electrode (RDE) method or through the comparison of fuel cell polarization curves. As pointed out in Gasteiger's review [97], a lack of standard testing procedures has created difficulties in comparing various published data. It was suggested that all the data be compared using a set benchmark. The authors suggest that a good practice for all measurements (with an RDE and a fuel cell) is to report the kinetic current measured at 0.9 V vs. reversible hydrogen electrode (RHE), albeit biased by a requirement for a high cell voltage, making this benchmark appropriate for comparing Pt-based catalysts.

In general, the various Pt alloy catalysts (*e.g.*, alloyed with Fe, Co, Cr, Ni, Mn, Ir, Ti, or combinations thereof (reviewed in ref. [134]) have been observed to decrease the overpotential for the ORR by 20 to 40 mV. The creation of a bimetallic surface that is more reactive toward ORR has been explained through changes in the electronic nature of the surface, inhibited adsorption of species that block the surface, or changes in the structure of the surface atoms. As summarized in Gasteiger's review, [97] these possible explanations have not been conclusively

proven. Fundamental studies using an RDE is a method that allows for precise modification of the Pt metal as well as accurate area determination. Of the various combinations, PtCr, PtCo, and PtNi are the best performing of the alloys. This group displays a 3-4-fold increase in the ORR rate (measured at 0.8 V vs. RHE), and the alloys have been tested in fuel cells with similar results. The electrochemical behavior of these alloys was very similar to that of pure Pt. The current understanding is that the Pt atoms segregate to the surface through exchange with the Co and form a Pt skin over the surface. The modification of the electronic character of this "Pt skin" due to the underlying transition metals resulted in the increased ORR kinetics. In addition, dilution of the Pt with the alloying element increases the mass activity of the Pt. As Gasteiger points out, the application of bulk alloy results to a high area catalyst environment is difficult, so fuel cell testing is an important component of the evaluation process.

Also important, but not explicitly stated in the review, is the ease of creation of the modified catalyst. In many cases, the alloy is created through high temperature alloying and the fine dispersion needed can be difficult to realize [135]. Another issue is the change in the hydrophilic nature of the catalyst particles, making them more susceptible to flooding due to the increased hydroxide content on the surface. It is certainly true that the move toward Pt alloys as the catalyst for ORR is necessary, but many issues still need to be resolved.

Prior to the start of our project, Zn modified Pt alloy had never been investigated as a candidate for ORR in literature, presumably because people have predicted electron transfer from Pt $5d$ to Zn $3d$ is not possible as the Zn $3d$ orbital is already full. Also, Fernandez *et al.,* [114] has considered Zn as a possible alloying material for Pt, but concluded Zn-alloy is not favorable for catalyzing ORR as Zn would form stable Zn-O bonds rather than aid breaking O-O bonds. However, Rodriguez's PtZn work described in **Chapter 2** contradicts with these predictions.

In this chapter, we will describe the characterization of an electrodeposited layer of Zn on Pt and the resulting surface alloy formation as demonstrated by surface analytical measurements. The analysis was performed by Dr. Ed Guerra and Mr. Yanguo Yang (under the supervision of Dr. Dan Bizzotto). Through this analytical effort, the realization of the ease which the Zn/Pt alloy interacts with oxygen led us to investigate its catalytic properties for ORR. The ORR electrochemistry for Pt and the electrochemistry for Zn-modified Pt surfaces are explored

using RDE electrochemical measurements. The method for creating the Zn-modified Pt surface and the resulting improvement in the ORR overpotential will be described, and comments will be made on the stability of the Zn/Pt alloy. The results from these fundamental studies are used in the creation of a modified cathode gas diffusion electrode (GDE), which is tested in a single fuel cell. This section was performed by Mr. Winton Li in the Department of Chemical Engineering (under supervision of Dr. Elod Gyenge and Dr. Dan Bizzotto) as a 4th year project. Comparison of the polarization curves for a single membrane electrode assembly (MEA) composed of either a Pt or a Zn-modified Pt cathode GDE will be presented.

4.2. Experimental section

4.2.1. General electrochemistry and the PtZn alloy preparation

Electrochemical setups, as well as Zn deposition and subsequent alloy formation was performed in a same manner described in **Chapter 3**. Briefly, Zn was electrodeposited on Pt RDE from a $ZnSO_4$ solution, followed by a spontaneous alloy formation at the room temperature under Ar atmosphere. Unalloyed Zn was stripped off electrochemically and the electrode surface was washed with a dilute H_2SO_4 acid solution. Potentials reported are referenced to the reversible hydrogen electrode (RHE).

4.2.2. Oxygen reduction reaction and the data processing

After the solution cleanliness was assessed using the Pt Ar saturated CV, the electrolyte (0.1 M H_2SO_4) was saturated with oxygen (Praxair) and the ORR measurements were performed using a smooth Pt and PtZn electrodes at 22 °C. While the ORR CVs were recorded, oxygen flow was kept on the electrolyte surface. The kinetic current was calculated using two approaches. The anodic and cathodic polarization curves were recorded at 10 mV/s with rotation

speeds varying from 500 to 3000 rpm. The potential range was restricted to 0~1.00 V. The CV for 2000 rpm rotation rate was used to calculate the kinetic current using **Equation 3-5**. This data analysis was limited to potentials where the measured current was less than half the limiting current, typically above 0.8 V. The Koutecky-Levich (KL) analysis (**Equation 3-4**) was also performed using the data obtained at all rotation frequencies. In-house built LabView software was used to perform the calculation. The program first reads the ORR curves recorded at different frequencies on a particular electrode. The intercept of the KL plot (j^{-1} vs. $\omega^{-1/2}$) over a restricted potential range was used to calculate the kinetic region, which leads into the Tafel analysis (E vs. log i_k). Regression analysis on the Tafel plot is also the part of the program, and the potential region can be manually controlled to optimize for the R^2-value as close to 1 as possible. These kinetic currents were plotted as a function of potential in the usual Tafel plot.

4.2.3. Auger electron spectroscopy on Zn modified electrode

Auger electron spectrometry (AES) analysis was carried out in a MICROLAB 350 Auger electron spectrometer (ThermoElectron Corp.) with a field emission electron gun (10 keV, 3 nA) under vacuum (~10^{-10} mbar). This instrument also allowed simultaneous measurements of scanning electron microscopy (SEM) images. Survey Auger electron spectra were acquired using the hemispherical energy analyzer for a constant resolution of 4, while the higher energy resolution spectra, to show Auger fine structure, were measured with the resolution at 40 (corresponding to approximately 0.5% energy resolution).

4.2.4. Membrane electrode assembly preparation and testing

The preparation method of the PtZn or Pt MEA is detailed in **Chapter 3**. All fuel cell experiments were performed by Mr. Winton Li. Briefly, the Zn modification onto the 20 wt% Pt/C (5 cm^2) was performed electrochemically, using a 0.1 M $ZnSO_4$ solution. Zn was deposited to Pt/C at -0.95 V for 5 minutes, followed by the 20 minutes of a spontaneous alloy formation and

the stripping of unreacted in the $ZnSO_4$ solution at -0.3 V. The full MEA was then assembled by hot pressing the Zn-modified gas diffusion layer (GDL) with a Nafion™ membrane at 115 °C under a weight of 800 lbs for 60 seconds. Single cells were then assembled using Au-coated end plates (9 cm × 9 cm) with serpentine flow field pattern (Electrochem Inc.). Typical fuel cell operating parameters were as follows: cell temperature 74 °C, anode and cathode gas stream humidity characterized by a dew point of 75 °C, hydrogen and oxygen flow rates 500 and 400 mL min⁻¹ respectively, and stoichiometric coefficients equal to 1.1 for hydrogen and 1.2 for oxygen. The absolute pressure on the cathode side was kept constant at 350 kPa, while the anode side pressure was either 350 or 101 kPa.

Before recording the polarization curves, all MEAs were conditioned in an identical fashion ensuring proper and stable membrane hydration. Conditioning was performed using three different constant-voltage steps, starting with 0.5 V for 3-4 h, until the superficial current density reached about 400 mA cm⁻², followed by operation at 0.3 V and finally 0.1 V for 1 h each. At the end of the conditioning stage, the polarization curve was recorded by applying successive constant-current steps between 0.1 and 3 A for 5 min duration at each step.

4.3. Results and discussion

The Zn-modified Pt electrode was prepared electrochemically relying on previously reported work dealing with the underpotential deposition (UPD) of Zn onto Pt for the study of the kinetics of Zn electrodeposition in highly acidic electrolyte [107]. In that paper, we confirmed the creation of a UPD Zn layer on Pt and its eventual transformation into an alloy originally reported in ref [110]. The deposition of a monolayer of Zn onto the Pt electrode was recognized through its influence on the electrochemical response where the overpotential for H_2 evolution increased, a new peak was generated in the double-layer region, and the CV showed a change in the Pt oxide region. These changes were all thought to be due to the presence of Zn. The existence of a PtZn alloy was indirectly shown through electrochemical investigations which agreed with other reports in the literature [106]. It was important to confirm the presence of Zn on the Pt electrode and if possible to show the presence of the PtZn alloy. Initial surface

analytical measurements were performed on a Pt wire since introduction of the polymer sheathed RDE electrodes into the vacuum chamber was prohibited due to outgassing and space constraints.

4.3.1. Formation of surface PtZn alloy characterized by AES

A Pt wire was electrochemically modified with an electrodeposited layer of Zn and introduced into the ultrahigh vacuum (UHV) chamber for analysis by Auger electron spectroscopy (AES). A significant amount of oxygen was detected, suggesting that the electrode surface was oxidized. In an attempt to protect the UPD layer from air oxidation, a thick layer of bulk Zn was electrochemically deposited onto the Pt surface. The thick Zn coated electrode was then carefully etched by Ar^+ sputtering in the UHV environment until oxygen was no longer detected. **Figure 4-1** shows the overall SEM image taken from the Ar^+ etched electrode surface. The image indicates three distinguishable regions, labeled "I", "II", and "III" in **Figure 4-1** with more detailed secondary electron images of these regions shown in **Figure 4-2**. Region I has a plateau-like topography; in contrast, region II is composed of conelike structures, whereas region III has a rugged topography. Low-energy-resolution survey-scan Auger spectra were measured for each region (**Figure 4-3**). These spectra clearly establish that regions I and II are pure metallic Pt and Zn, respectively, whereas region III has characteristic Auger peaks of both Zn and Pt.
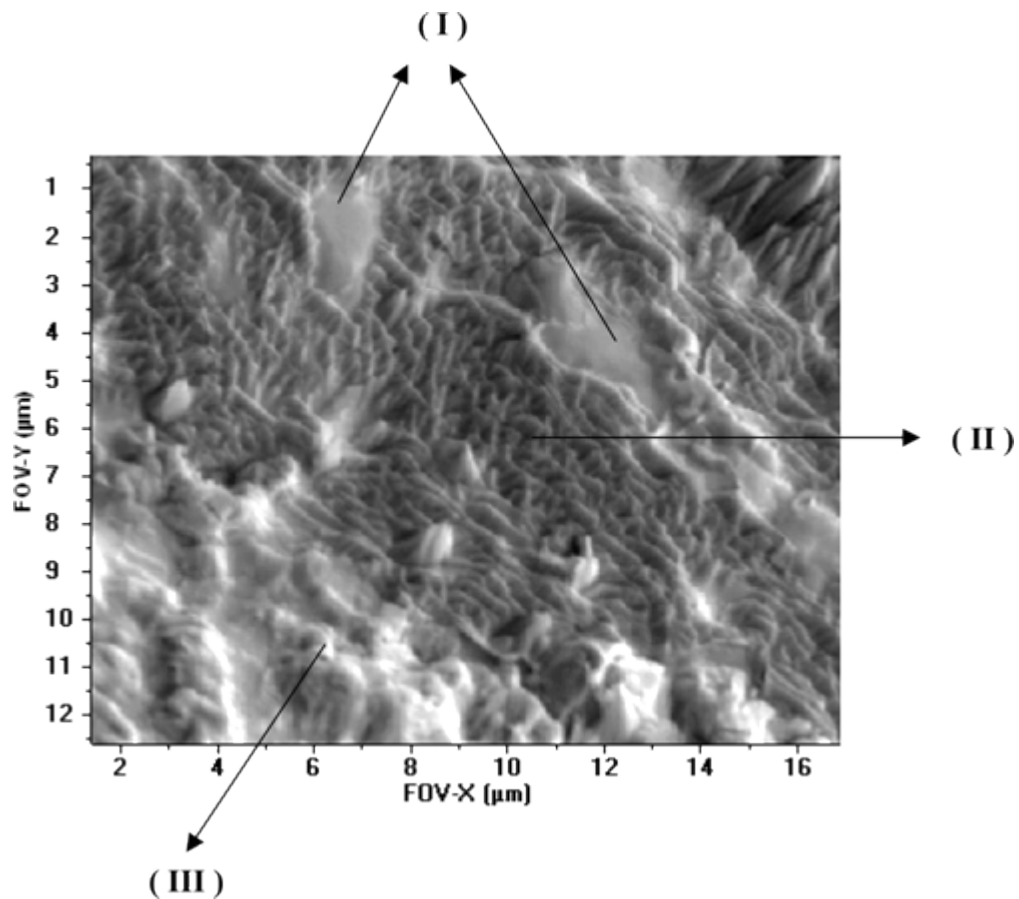
Figure 4-1 SEM micrograph after Ar$^+$ etching of a thick electrodeposited Zn layer on a Pt electrode. Three regions are indicated on the SEM which correspond to Pt (I), Zn (II), and Zn/Pt alloy (III). Reproduced with permission from [7]. Copyright 2006 American Chemical Society.
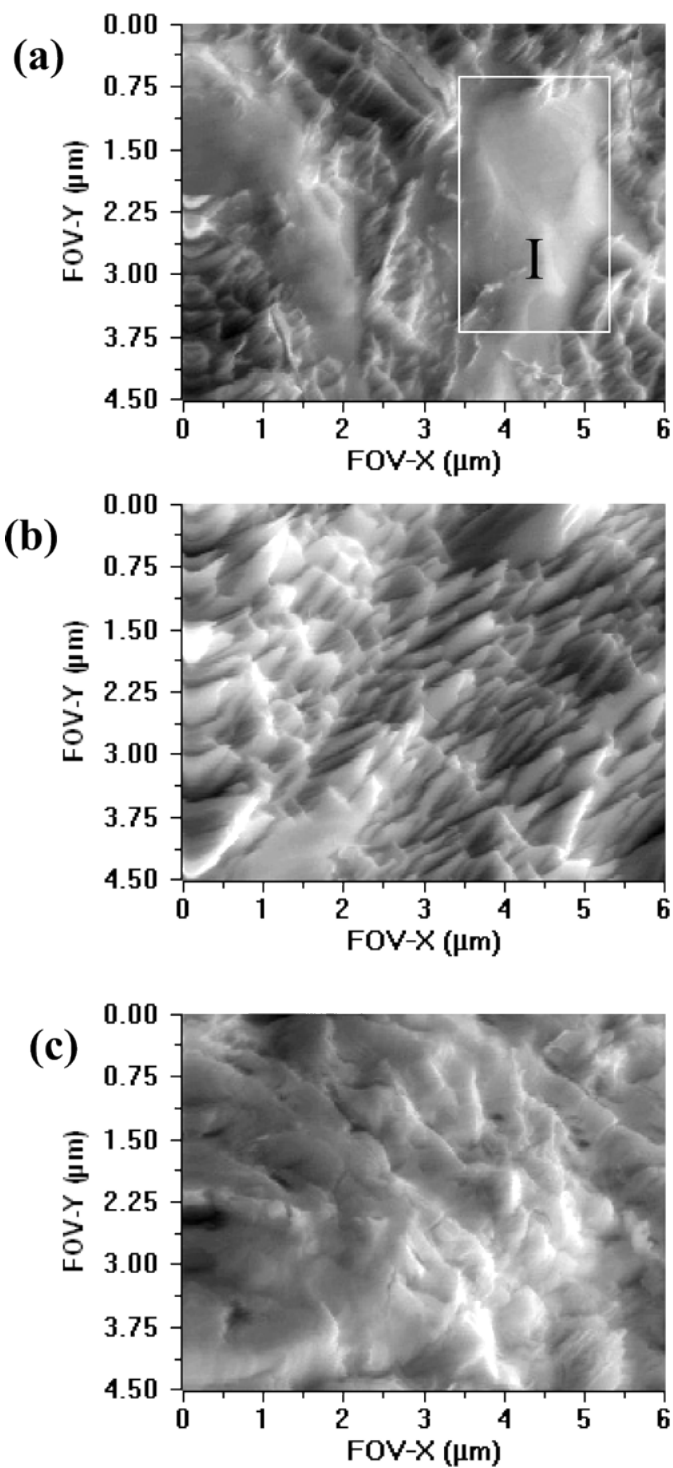
Figure 4-2 Higher magnification SEM images of (a) region I (Pt), (b) region II (Zn), and (c) region III (Zn/Pt alloy) identified in **Figure 4-1**. Reproduced with permission from [7]. Copyright 2006 American Chemical Society.
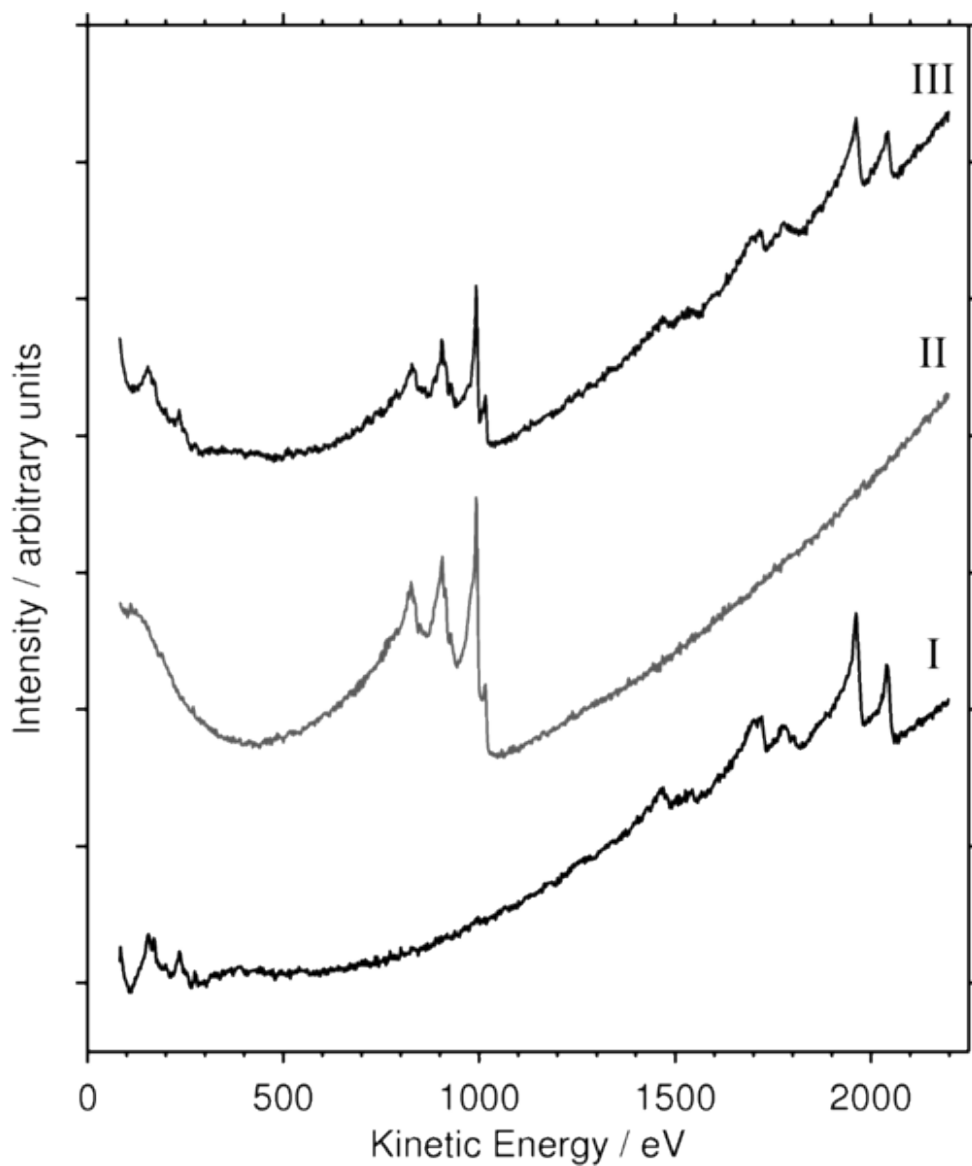
Figure 4-3 Auger electron survey spectra for the regions I (Pt), II (Zn), and III (Zn/Pt alloy) (bottom, middle, top, respectively) identified in **Figure 4-1**. Reproduced with permission from [7]. Copyright 2006 American Chemical Society.

Changes in both structure and composition of surface alloys may alter their Auger line shape [136, 137] implying that Auger line shape analysis may provide further evidence for identifying whether the deposited zinc interacts chemically with the platinum to form a Pt/Zn surface alloy. **Figure 4-4a** compares the high-resolution Auger electron spectra for Pt in region III with that from pure Pt (region I). Auger line shape analysis indicates that Pt AES peaks at 1960.5 (MN_3) and 2040.8 eV (MN_2) from region I give an area ratio of 1.86, whereas region III has a peak area ratio of 1.14. This change appears to result from interactions between Zn and Pt altering the Pt MNN Auger transition probability. Changes are also seen in the Zn Auger spectra (**Figure 4-4b**), where the shoulder at about 980.6 eV decreases markedly. This evidence shows that both the Pt and Zn Auger electron spectra obtained from region III differ from those of pure metallic Pt and Zn. Therefore, it appears reasonable to assign region III as a Zn/Pt alloy region. Comparison of Auger peak areas for region III reveals the alloy has a chemical composition close to $Zn_{0.73}Pt$ (42 at. % Zn), where the relative sensitivity factors for Pt and Zn used in the quantitative analysis of the Auger spectra were self-generated from **Figure 4-1** measured for the pure Pt and Zn regions. This approach should minimize most of the uncertainties involved in routine quantitative Auger analysis. The possibility is still open that Zn may have been removed preferentially during the Ar^+ sputtering, but considering the prolonged sputtering did not change the spectral features, we concluded that the composition of region III is satisfactorily close to the 1:1 Pt:Zn alloy, which has a large stability region in the bulk Pt-Zn phase diagram [102].

The top panel in **Figure 4-5** shows AES spectra measured from the electrode surface after sputtering and leaving in 2.5×10^{-9} mbar UHV environment for 2 h. The spectra show the presence of more oxygen (peak at 509 eV) at the PtZn alloy (region III) than at pure Zn in region II, whereas no oxygen was found at the Pt region. This observation suggests that the PtZn alloy interacts more readily with oxygen than does pure Zn. Interestingly, however, Zn atoms in the alloy do not interact strongly with oxygen. Zn Auger spectra for both metallic Zn and the PtZn, before and after the oxidation of the surface, are shown in **Figure 4-6a** and **b**, respectively. When oxygen binds to metallic Zn, the Auger transitions (peaks at 990 eV and 1020 eV) shifts to lower kinetic energy by ~10 eV. The negative shift is even observed for the secondary electrons ejected from the inner level (*i.e.* the peak at 1200 eV), indicating the formation of stable ZnO. On the other hand, alloyed Zn did not show such shifts after oxidation, which suggests alloyed Zn does not interact with oxygen strongly. Such behavior has also been

observed with Zn in Ru(001)/Zn alloy as mentioned in **Chapter 2** [119]. As shown earlier, PtZn exhibited stronger affinity for oxygen than pure Zn, but this indicates the interaction of oxygen may only occur on Pt atoms in the alloy, or only with the outer most orbitals of Zn. The latter may be a likely case, as the relative Auger transition probabilities of Zn LM_2 and LM_3 before and after oxidation change.

After exposing the surface to the same UHV conditions for further 10 h, the amount of oxygen detected increased in both the Zn/Pt and Zn regions (**Figure 4-5**, bottom panel) whereas the Pt region was still not oxidized. Interestingly, a trace amount of Zn is now detectable in the Pt region. In this case some Zn/Pt alloy may be formed via zinc migration across the surface. The room temperature diffusion of Zn into Pt is well-known and is characterized by a very large diffusion coefficient [110]. This apparently results from a small crystallographic misfit so that Zn atoms can occupy the Pt atom positions with little change in the lattice parameter [107].
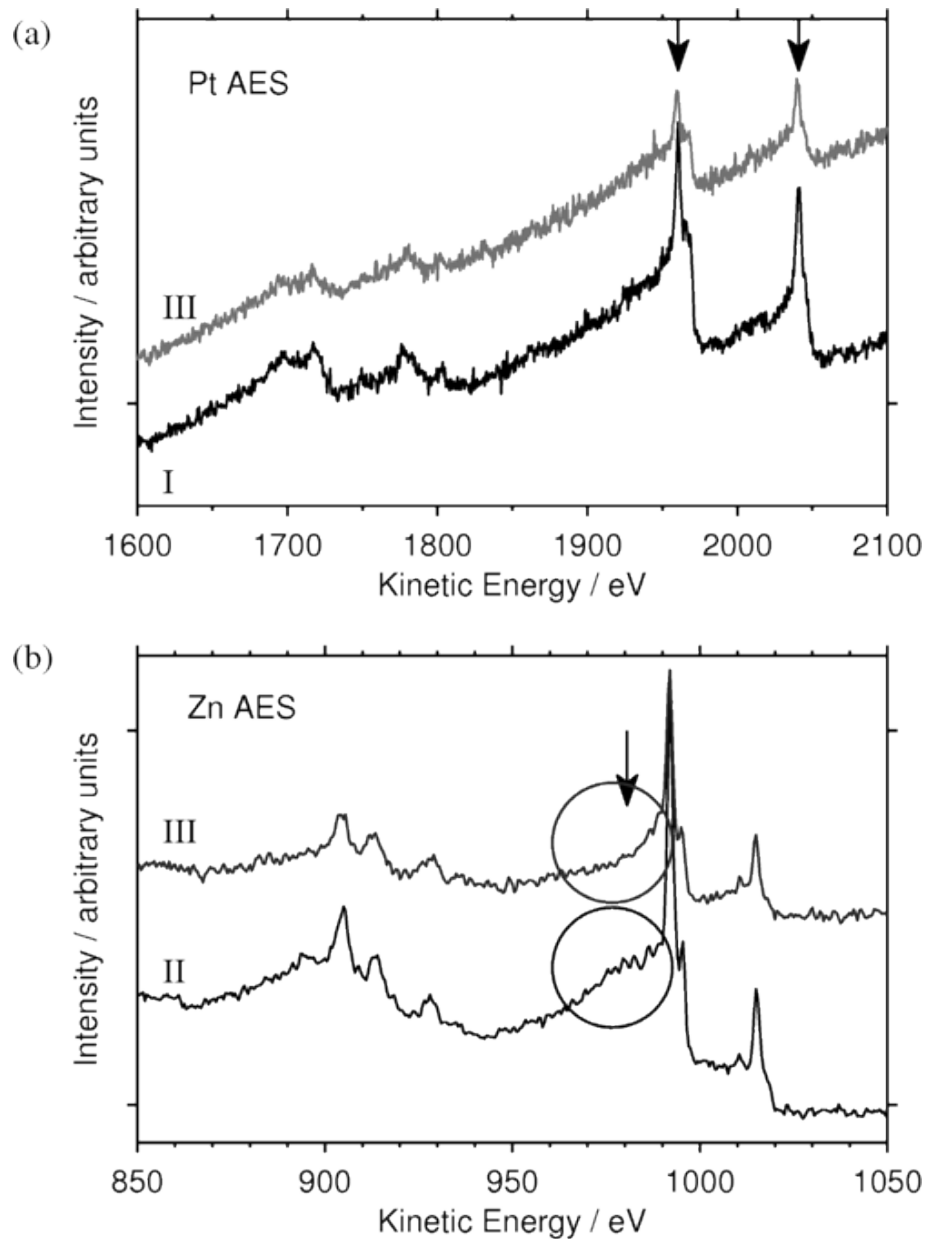
Figure 4-4 High-resolution Auger electron spectra of (a) Pt from regions I and III and (b) Zn from regions II and III. Pt Auger transition peak heights at 1960.5 and at 2040.8 eV from region I give an area ratio of 1.86, whereas region III has a peak area ratio of 1.14. The metallic Zn Auger transition spectrum shows a shoulder by the peak at 980.6 eV but the shoulder diminished when Pt was modified by Zn. Reproduced with permission from [7]. Copyright 2006 American Chemical Society.
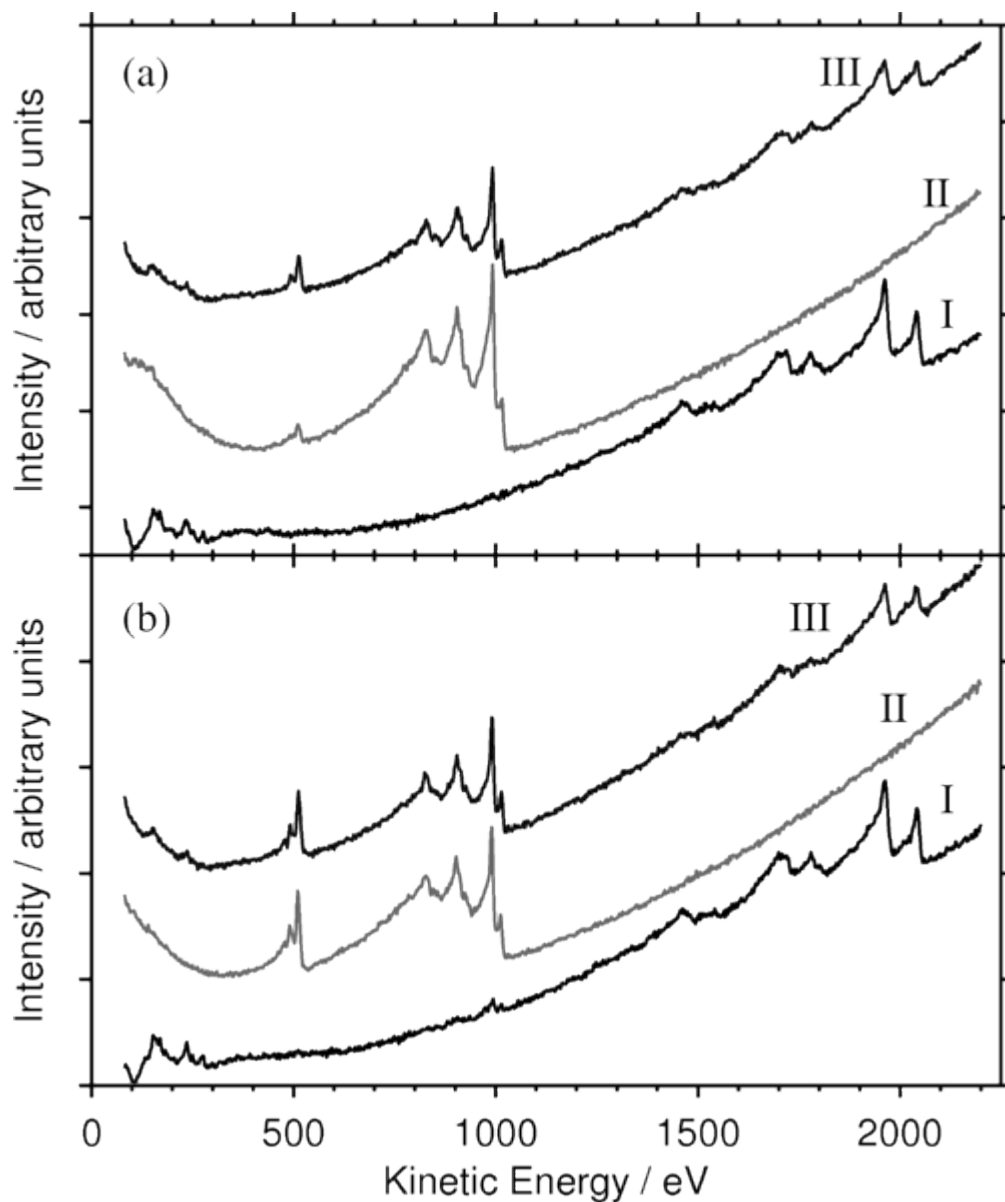
Figure 4-5 Auger electron survey spectra of regions I (Pt), II (Zn), and III (PtZn) after leaving in a vacuum (2.5×10^{-9} mbar) for (a) 2 and (b) 10 h. After 2 hours, the amount of oxygen on the PtZn surface was greater than the amount on the Pt surface. Reproduced with permission from [7]. Copyright 2006 American Chemical Society.
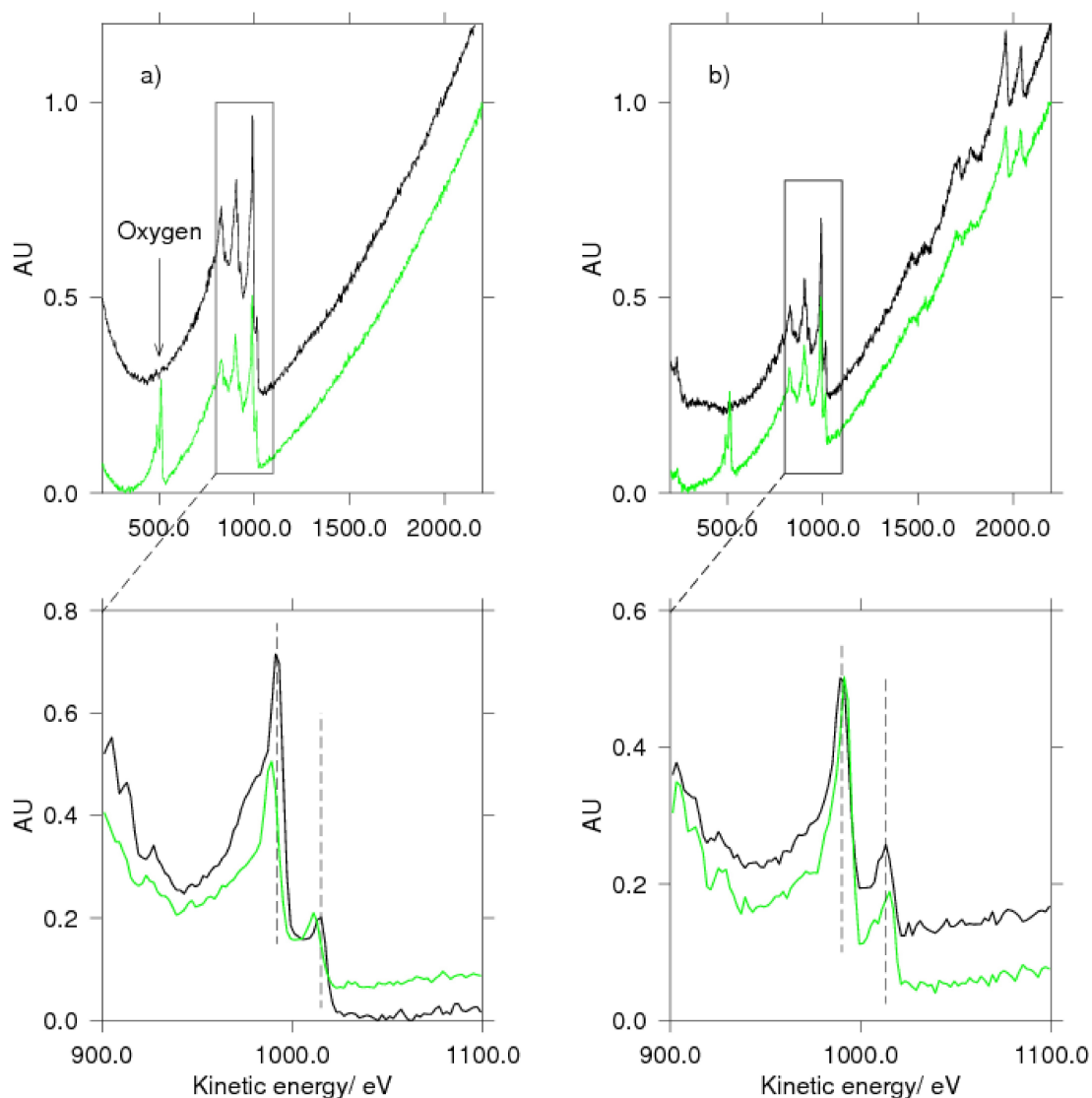
Figure 4-6 Auger electron spectra of a) metallic Zn and b) PtZn; before and after the surfaces interact with oxygen in the UHV chamber. The peaks observed at 500 eV on the spectra in the top panels are the indication of the presence of oxygen. Auger transition peaks of Zn in 900 ~ 1100 eV region are shown in the bottom. The peak positions shift to lower kinetic energy with the presence of oxygen on the metallic Zn, indicating oxygen is strongly interacting with the Zn surface. On the other hand, the signals from the PtZn surface were not affected by the presence of oxygen, indicating very weak or no interaction between Zn in PtZn and oxygen.

4.3.2. Preparation of the Zn-modified Pt RDE.

The Zn-modified Pt RDE was prepared via electrodeposition from $ZnSO_4$ solution at 22 $^\circ$C. The Pt CV in this solution is shown in **Figure 4-7a**. The potential is referenced to Hg/Hg_2SO_4 in the plot. Bulk deposition of Zn begins at -0.85 V, although the first monolayer of Zn is deposited at potentials *ca.* 1 V more positive. Zn was electrodeposited onto the Pt electrode by setting the Pt potential to -1.06 V for 300 seconds. A significant quantity of Zn was deposited onto the Pt surface (2.43 C cm^{-2}). The electrode with deposited Zn was removed from solution, and the alloy was allowed to form for 60 min in an Ar atmosphere. The modified surface was then placed back into the electrolyte solution at a potential where Zn oxidation/stripping occurs (-0.3 V), showing a characteristic current transient that indicates a limited amount of Zn was removed (2.27 C cm^{-2}). The deposition and stripping currents are shown in **Figure 4-7b**. Ignoring the contribution from residual oxygen reduction that is present in both curves, the difference between the two charges would be equivalent to the amount left on the surface, or alloyed with the Pt. The difference accounted to 0.167 C cm^{-2}. Approximately 300 μC cm^{-2} has been reported for a UPD layer of Zn on Pt single crystal surface [138, 139] giving a net deposition of ~500 monolayers of Zn in the present case, but our own studies showed only 4% of Zn deposited was alloyed to Pt (determined by gravimetry which will be shown in **Chapter 6**), which leads to the formation of a 1:1 surface alloy in the first ~40 layers. In addition, it is important to note that the Zn stripping potential was not made very anodic so as to avoid oxidation of the Pt surface which would remove the Zn/Pt alloy. As demonstrated previously [107] the alloy formed in this way is stable at all potentials below 1.2 V. In fact, the Ar saturated CVs and ORR curves discussed next can be reproducibly obtained from the modified electrode surface many days afterward. In addition, because the diffusion of Zn into the bulk of the Pt electrode occurs very quickly, one Pt RDE has irreversibly changed into the Zn/Pt alloy form after many deposition/alloying cycles. The same ORR results can be also obtained from this now permanent Zn/Pt electrode as those reported.
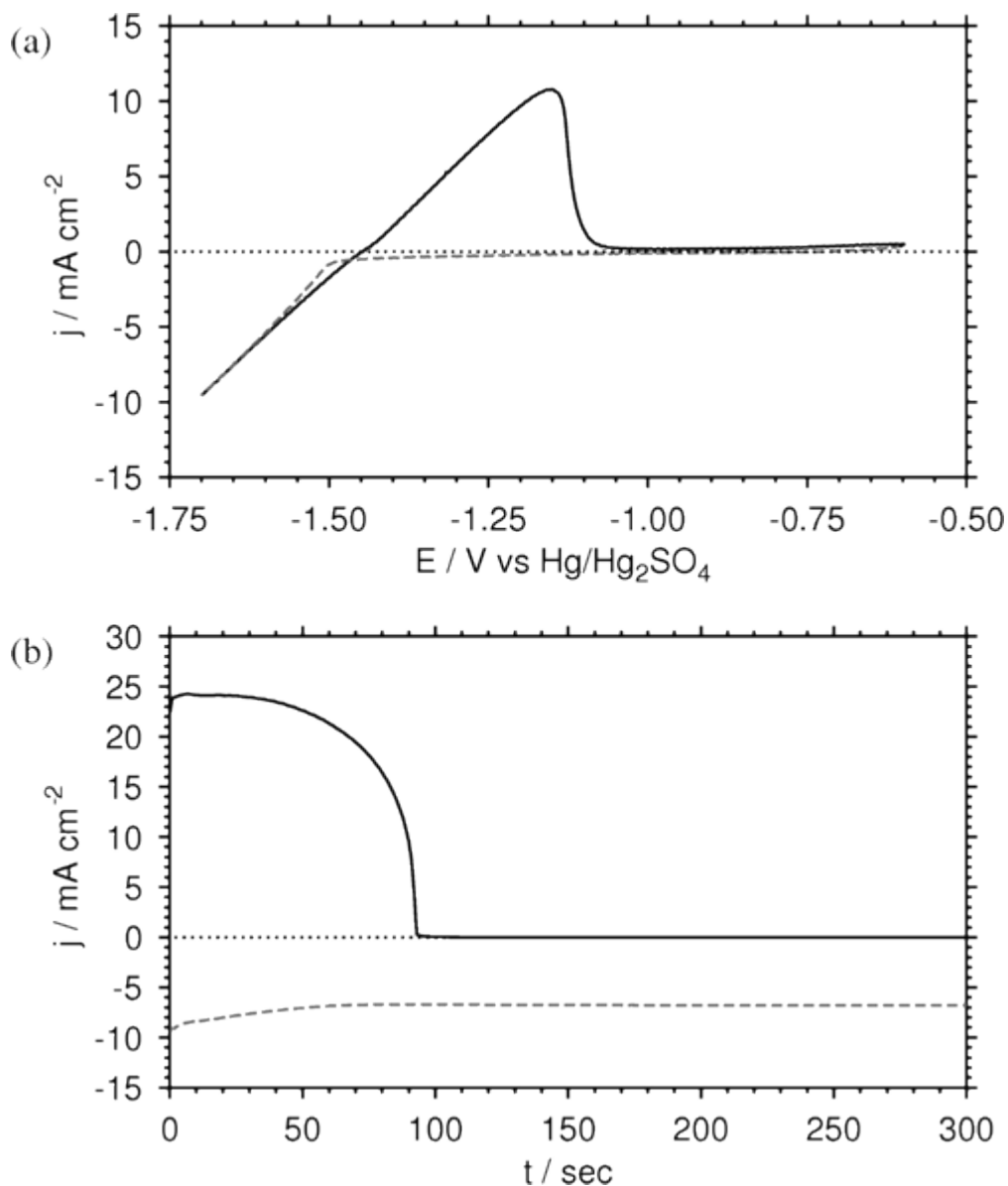
Figure 4-7 (a) Cyclic voltammetry (100 mV/s, 22 C) of Pt in 0.1 M ZnSO$_4$ showing deposition and stripping processes. (b) Current transients for the deposition (dashed line) of Zn onto the Pt electrode and the resulting current transient for the stripping (solid line) of the Zn remaining on the Pt electrode after allowing the formation of the Pt/Zn alloy. Reproduced with permission from [7]. Copyright 2006 American Chemical Society.

4.3.2.1. Ar saturated CVs of Pt and PtZn

Ar saturated CVs recorded on Pt and PtZn (*i.e.,* in an Ar saturated 0.1 M H_2SO_4 solution between 0.03 and 1.3 V or between 0.03 V and 1.0 V, respectively, at the sweep rate of 50 mV/s; 22 °C) are compared in **Figure 4-8**. Hydrogen adsorption/desorption peaks, as well as hydrogen evolution, on PtZn are diminished compared to Pt, which is consistent with the literature [90, 107]. Solution cleanliness was assessed by the Pt CV before and after the PtZn CV was recorded, indicating the difference between the Pt and PtZn CV's was due to the presence of Zn, rather than solution contamination. The PtZn-oxide formation is also shifted anodically by ~80 mV at 20 $\mu A/cm^2$ which indicates the oxide layer formed on PtZn is more weakly adsorbed than on Pt. Such a layer is readily reducible, thereby improving the ORR catalysis [69, 140]. The kinetics of ORR catalysis on Pt and PtZn is compared next.
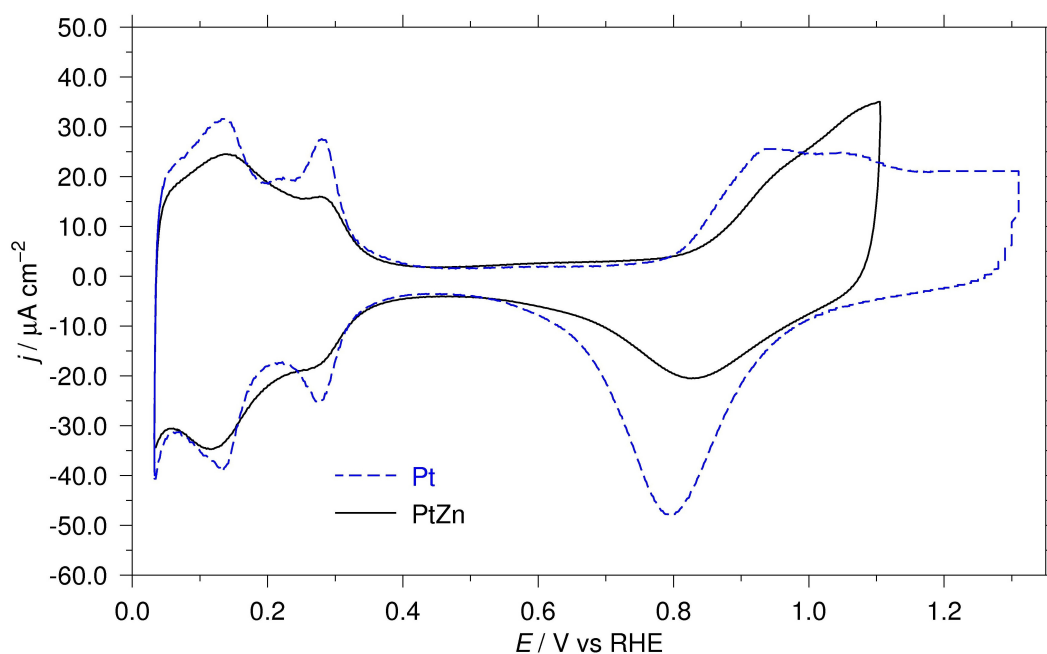
Figure 4-8 Comparison of Ar saturated CVs recorded on the Pt (dashed line) and the PtZn (solid line) electrodes at 22 °C. Hydrogen adsorption/ desorption peaks are disappeared in the PtZn CV, and the Pt (or PtZn) oxide formation is shifted anodically. Reprinted from [8]. Copyright 2009 with permission from Elsevier Ltd.

4.3.2.2. ORR kinetics for Pt and Zn-modified Pt electrodes

An anodic voltammogram of the smooth Pt RDE in a solution of 0.1 M H_2SO_4 (22 ^{o}C)saturated with O_2 rotating at 2000 rpm is shown in **Figure 4-9**. The ORR kinetics were measured using the Koutecky-Levich (KL) methodology (**Equation 3-4)**. The mass transfer corrected current was determined using the rotating disk electrodes from the anodic sweep direction. A Tafel plot generated from this voltammogram properly corrected for mass transport is shown in **Figure 4-10** compared to a KL analysis of a series of these voltammograms measured at various rotation rates (500-3000 rpm). The kinetic current calculated from the KL analysis (**Equation 3-4**) and the mass transport corrected current (**Equation 3-5**) are very similar. The slope of the lines in the KL plot is 3.7 cm^2 $s^{-1/2}$ mA^{-1} for the ORR on smooth Pt, consistent with values reported in the literature [27]. The Tafel slope in the potential region around 0.80 V was calculated to be 98.4 $\pm$ 5.9 mV/decade for the anodic scan direction as expected for ORR in H_2SO_4.

The ORR performance of the Pt/Zn electrode is compared to that of the smooth Pt RDE through a voltammogram measured in the same electrolyte (0.1 M H_2SO_4 saturated with O_2; 22 ^{o}C) at the same rotation rate (2000 rpm); both are shown in **Figure 4-9**. A shift in the potential (approximately +30 mV) of ORR is observed for the Pt/Zn electrode. It is important to note the ORR curve on PtZn was recorded without polishing the surface, *i.e.,* the electrode surface is rough comparing to the starting Pt. As shown in **Chapter 2**, this has a significant impact on catalysis. However, the positive shift for PtZn in the recorded voltammogram was reproducible. This topic will be discussed in detail in **Chapter 5.3.4**. The KL analysis for the Zn-modified Pt RDE gave slopes that were similar to that measured for the smooth Pt RDE, about 3.8 cm^2 $s^{-1/2}$ mA^{-1}.

The kinetic currents are plotted with respect to potential in **Figure 4-10** for both electrodes using the two methods of determining kinetic currents. Both methods give similar curves, though the KL analysis is slightly shifted to larger currents when the kinetic current is calculated via **Equation 3-5**. The shift is consistent within both sets of analyses, which suggests a slight underrepresentation of the kinetic current determined by **Equation 3-5**. The shift in potential (~30 mV) due to Zn modification is demonstrated in these Tafel plots. For example, at 1 mA cm^{-2}, the Pt electrode is at 0.890 V/RHE while at the same current the Zn-modified

electrode is at 0.920 V/RHE. The Tafel slope at 0.8 V for the Zn-modified Pt RDE (96.3 ± 4.1 mV/decade) is slightly smaller than for smooth Pt. The number of electrons exchanged during the reaction was calculated using *Levich equation* (*i.e.,* **Equation 3-3**). The kinematic viscosity of 0.1 M H_2SO_4 at 20 ^oC is 0.01014 cm^2/s [113], and the concentration of oxygen was (8.35 ± 1.97) × 10^{-4} mol/L, the number of electrons was calculated to be 3.97. Our Tafel plot data suggests a possible modification in the mechanism for the ORR on the modified surface, yet maintaining the direct pathway rather than a parallel pathway (*i.e.,* water as a product rather than hydrogen peroxide).

PEM fuel cells are usually operated at 70~80 ^oC, and it would have been appropriate to conduct the RDE experiments at elevated temperatures. However, the RDE shaft is made of Teflon, which expands upon heating, but does not contract to the same extent upon cooling. This could cause leakage of electrolyte into the interior of the RDE. Therefore we limited our ORR investigation only at the temperature of 22 ^oC, which may not represent a fuel cell operating conditions, but should be sufficient for the comparative studies.

The ORR results shown above were observed under ideal conditions in an electrochemical cell, but it is important to test these results in a fuel cell. The modification of commercially available gas diffusion electrodes with electrodeposited Zn is described next along with creation of a modified MEA and testing under fuel cell conditions. The conventional method to prepare the carbon-supported Pt-alloy catalyst layers is to deposit a transition metal onto a preformed Pt/C by chemical vapor deposition, followed by a heat treatment at 700-1000 ^oC under an inert or reducing condition [69, 134, 141, 26, 140]. The method we used was the electrochemical deposition of Zn onto the Pt/C, which is unique to this work.
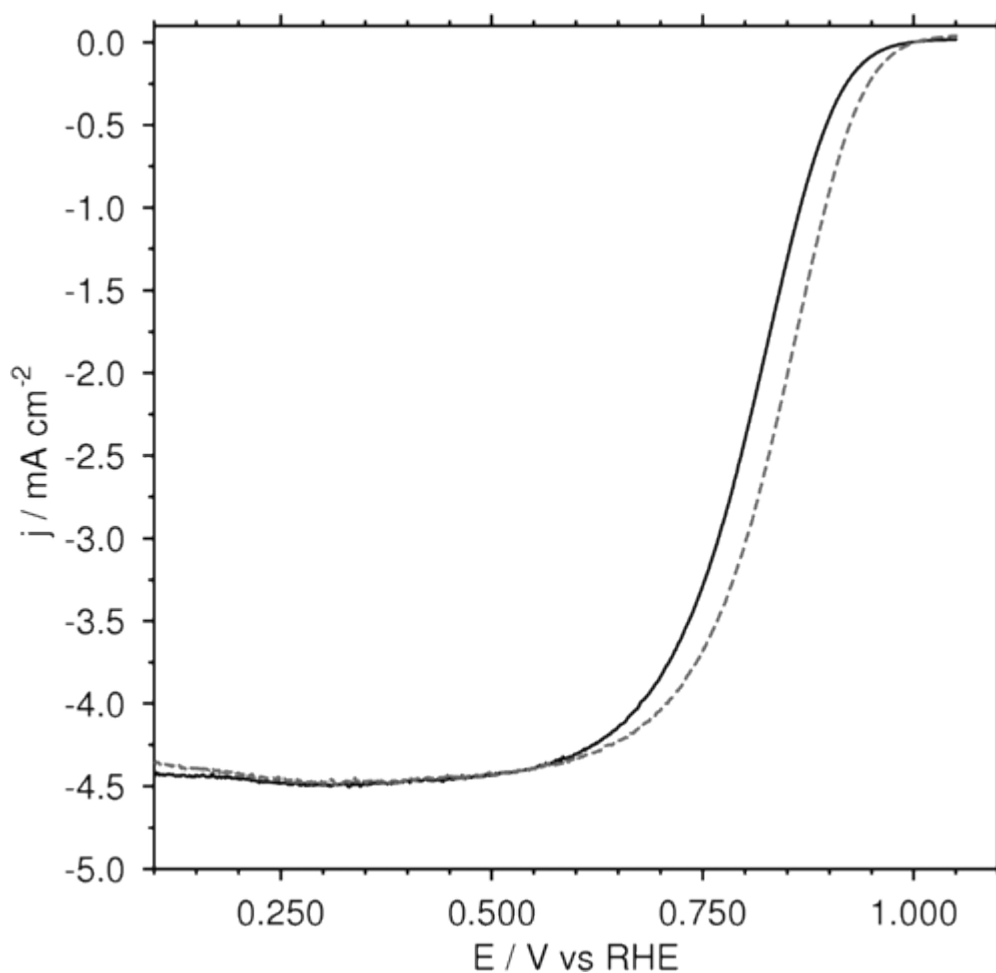
Figure 4-9 Comparison of the ORR activity measured at 2000 rpm (22 C) with an anodic voltage sweep rate of 10 mV/s for a smooth Pt RDE (solid line) and a Zn-modified Pt RDE (dashed line). Approximately 30 mV improvement in the overpotential with the PtZn alloy compared to with the Pt. Reproduced with permission from [7]. Copyright 2006 American Chemical Society.
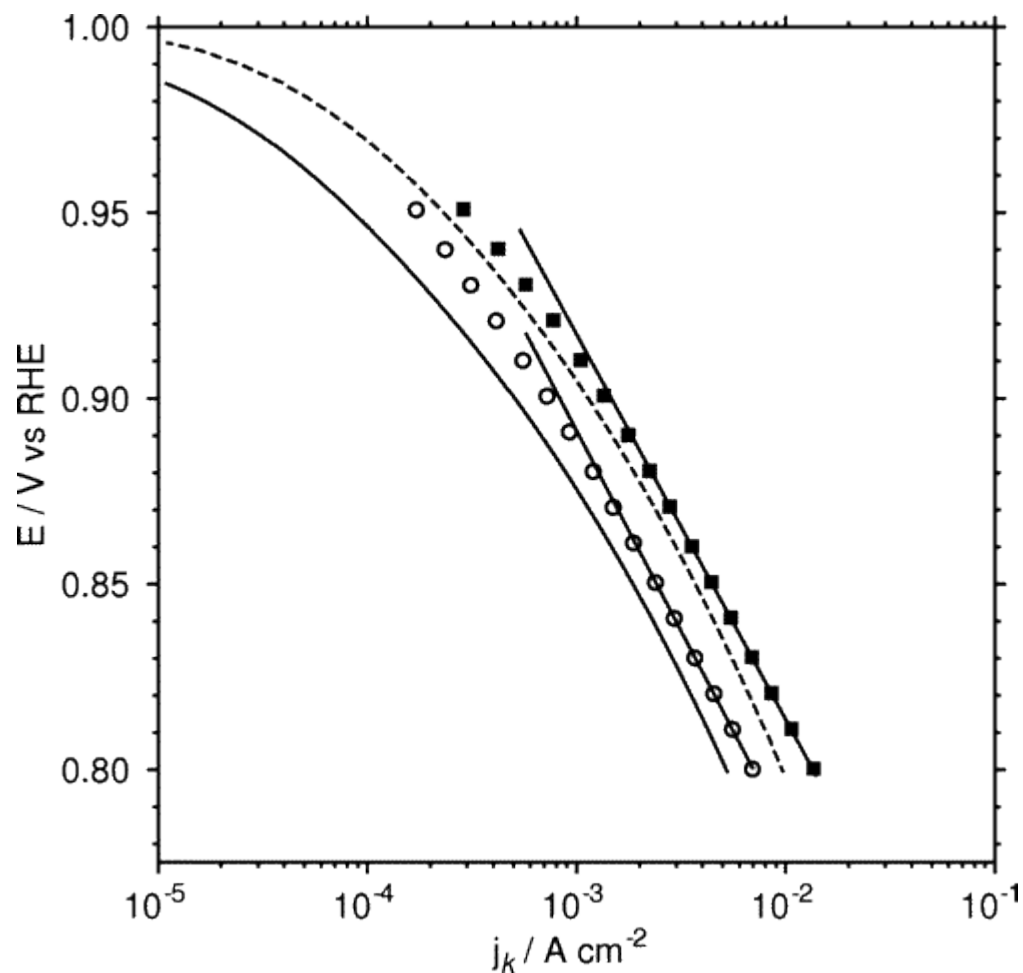
Figure 4-10 Calculated kinetic currents for the ORR on smooth Pt (solid line, o) and on Zn-modified Pt surface (dashed line, ■) for an anodic scan (22 °C). The data points were determined from the Koutecky-Levich analysis. The solid and dashed lines were mass transport corrected currents measured at 2000 rpm shown in **Figure 4-9**. Reproduced with permission from [7]. Copyright 2006 American Chemical Society.

4.3.3. Zn modification of a gas diffusion electrode

Commercially available gas diffusion electrodes (GDEs) were modified with Zn as described in the Experimental Section. These GDEs gave deposition and stripping curves (**Figure 4-11**) very similar to those seen for the Pt RDE. We assumed that only the Pt catalyst particles were modified with the electrochemically deposited Zn since this metal does not alloy to a significant extent with the carbon support and Zn is easily removed from the carbon surface [106]. The cyclic voltammogram of the GDE in $ZnSO_4$ shows the characteristic deposition and stripping regions at the same potentials as observed for the Pt RDE. Deposition of Zn was accomplished potentiostatically (-1.0 V for 5 min). The cell was disconnected and the alloy was allowed to form *ex-situ*. The potential was stepped to -0.3 V to strip the unalloyed Zn from the GDE. The difference between the deposition and stripping charge shows that 0.135 C cm^{-2} (~0.1 mg cm^{-2}) Zn remained, in the GDE. The Pt loading of this GDE was 1 mg cm^{-2}, suggesting that a 10 % loading of Zn on Pt was realized. This is a small modification, but alloying behavior may be significantly different on bulk Pt or on Pt nanoparticles on carbon (3~5 nm in size). This issue will be revisited in **Chapter 6**. This simple electrochemical deposition of Zn onto a commercially available GDE was sufficient to change the nature of the ORR kinetics, which suggests that such a process should be cost-effective and industrially feasible.

The Zn-modified GDEs were used as cathodes and pressed with an unmodified GDE as the anode. The resulting Zn-modified MEA was tested under two different fuel cell operating conditions and compared to a similarly prepared MEA that did not undergo the Zn treatment of the cathode. The treated and untreated fuel cells were tested at equal anode and cathode pressures (350 kPa), and the measured polarization curves are shown in **Figure 4-12a**. The open circuit voltage of the fuel cell containing the Zn-modified MEA (0.98 V) was slightly higher when compared to that of untreated Pt cathode (0.95 V), which is in good agreement with the RDE results. This shift to higher potentials was also observed in the kinetic region of the polarization curve (**Figure 4-12a**, inset) and at the higher superficial current densities.

The influence of Zn treatment of the cathode was also tested under operating conditions that maintained a pressure difference between the cathode and the anode inlet gas streams, *i.e.*, 350 and 101 kPa, respectively (**Figure 4-12b**). Operating at a higher cathode pressure increased

the superficial current density range of the fuel cells for both the Zn-treated and untreated MEAs. This effect is most likely due to the improved membrane humidification as a result of water back flow created by the 249 kPa pressure difference between the cathode and anode. The open circuit voltage for the Zn-treated MEA was higher by 30 mV. This shift was also evident in the kinetic region of the polarization curve shown in the inset. The increase in potential was ~70 mV at 200 mA cm^{-2} under these operating conditions as compared to the polarization curve measured for similar anode and cathode inlet pressures. Interestingly, for superficial current densities higher than 200 mA cm^{-2} the voltage differential between the treated and untreated MEAs diminished to about 30 mV, which was maintained up to 600 mA cm^{-2}. This was likely due to the larger ohmic drop observed in the case of the Zn-treated MEA which could arise in two ways. First, the Zn-treated cathode was hot pressed and bonded in-house to the cathode side of the MEA. Therefore, it is likely that the ionomer content and proton-conductive network of the cathode catalyst layer might be different as compared to the unmodified MEA, which could affect its performance. Second, tests have not yet been done to rule out the possibility of Zn^{2+} leaching from the catalyst, although the Zn/Pt alloy is stable in acidic environments as long as the cathode potential never exceeds 1.2 V (which did not occur in these tests [106]). The presence of Zn^{2+} in the ionomer would increase the ohmic drop. The stability of PtZn alloy will be discussed in **Chapter 6**. However, the improvement in the polarization curve is clear. The measured curves do not show optimal performance for potentials in the ohmic drop region (E = 0.6-0.2 V). It has been our experience that the performance of the untreated, commercial MEA from Electrochem Inc. is somewhat inferior to MEAs produced by other manufacturers when tested under similar conditions [142]. Nevertheless, it is important to emphasize that over the entire range of superficial current densities, the MEA with the Zn-modified Pt cathode gave a cell voltage between 30 and 70 mV greater than for the commercial MEA.

When comparing polarization curves, reproducibility is important. This issue was tested using in-house pressed unmodified MEAs. The conditioning method used in this work produced MEAs that gave reproducible polarization curves over an extended period of testing. The variability was found to be roughly ±20 mV throughout the polarization curve. The observed reproducibility of the polarization curves following the conditioning procedure helps substantiate the new conclusion that modification of the Pt MEA through Zn deposition leads to an improved activity for ORR compared to the current Pt cathode.
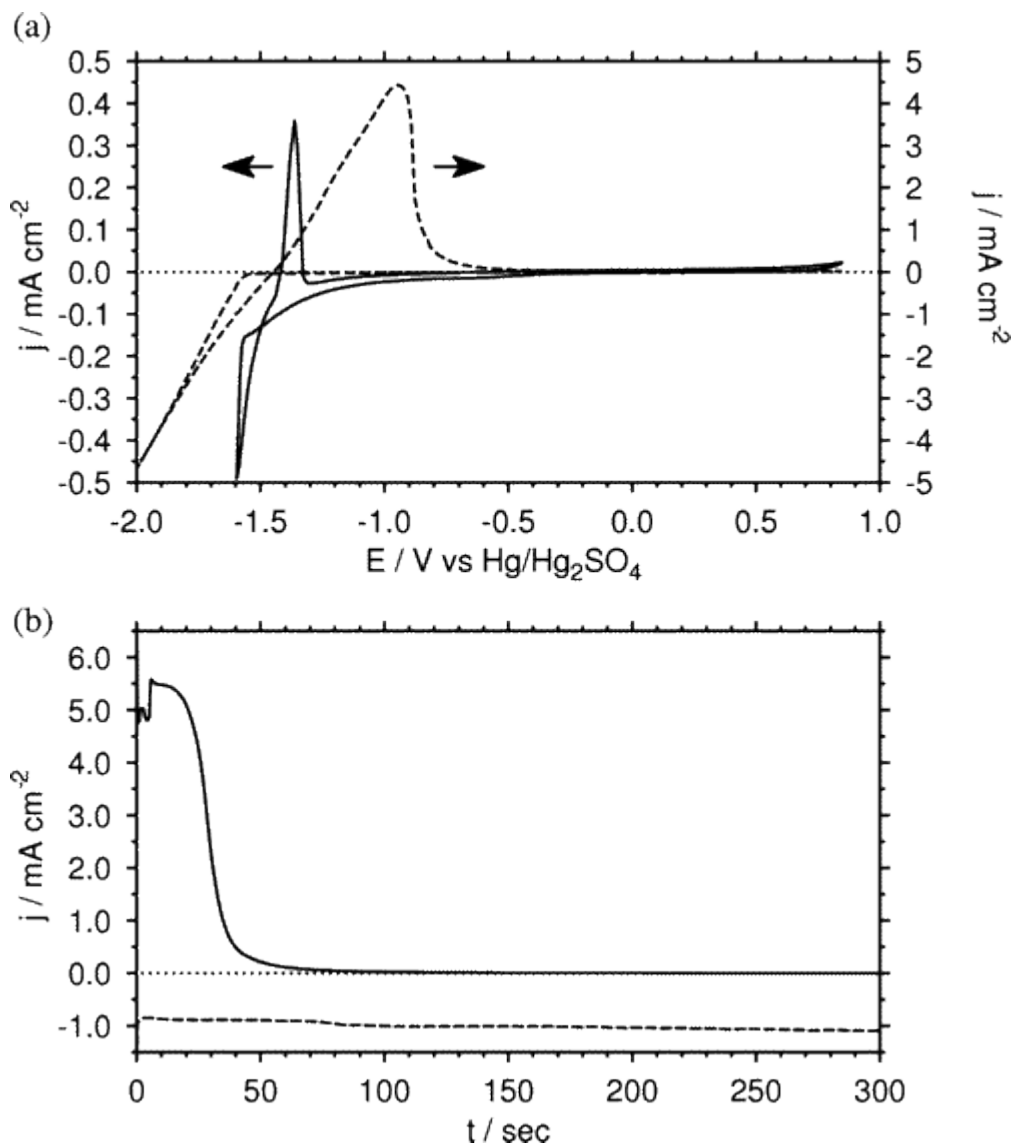
Figure 4-11 (a) Cyclic voltammogram (100 mV/s, 22 °C) of a 1 mg cm^{-2} Pt GDE in 0.1 M ZnSO$_4$ demonstrating the deposition and oxidation of the deposited Zn (solid line, cathodic limit of -1.6 V/Hg/Hg$_2$SO$_4$; dashed line, cathodic limit of -2.0 V/Hg/Hg$_2$SO$_4$). (b) The deposition and stripping current transients following a step to - 1.6 and -1.0 V vs Hg/Hg$_2$SO$_4$, respectively. Reproduced with permission from [7]. Copyright 2006 American Chemical Society.
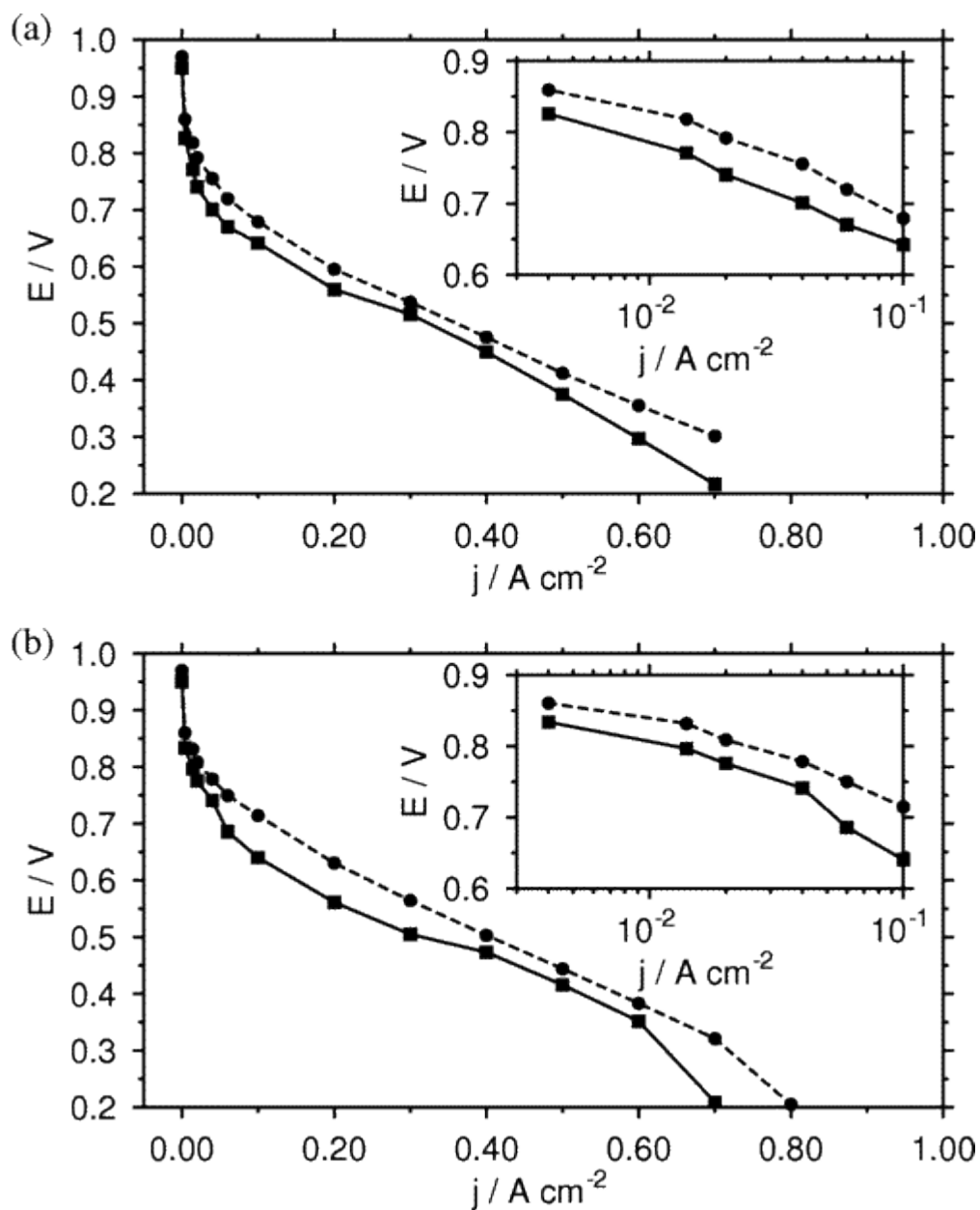
Figure 4-12 MEA polarization curves (74 °C) for Zn-modified (●) and unmodified (■) cathodes: (a) measured using the same inlet gas pressures for the anode and cathode; (b) measured using the higher cathode inlet gas pressure (350 kPa for the cathode and 101 kPa for the anode). In each case, the inset shows the low current kinetic region of the polarization curve. Reproduced with permission from [7]. Copyright 2006 American Chemical Society.

4.3.4. Effect on the electronic nature of the surface due to alloying Zn with Pt

The decrease in the ORR overpotential on the PtZn alloy surface as compared to Pt suggests a change in the manner in which O_2 interacts with the PtZn alloy. This implies a change in the electronic nature of the catalyst surface as a result of alloying with Zn. The inclusion of Zn as an alloy component with Pt for use as an ORR catalyst has not been reported prior to our finding. However, Zn is used as an alloying component in transition metal surfaces resulting in catalysts that are more selective or specific in their activity [112, 143, 144]. These changes in the surface properties have been related to a ligand effect, which changes the electronic properties of the surface, or to an ensemble effect, which modifies the number of active sites [145]. The addition of Zn to Rh, Ni, Pt, and Pd shifted the valence d band toward higher binding energies (thereby creating d-band vacancies) along with a shift to lower binding energies for the Zn $2p$ core level and Zn $3d$ band. For Pt, these changes result from a rehybridization that shifts electron density from the Pt $5d$ band toward the bimetallic bond with Zn which involves Pt $6(s, p)$ orbitals. These differences in the electronic structure of the PtZn compared to Pt will affect the surface-molecule interaction, which is important when considering the decrease in the ORR overpotential measured experimentally.

Further insight into these surface-molecular interactions and the chemical nature of the surface can be realized through the thermal desorption studies of adsorbed CO [144, 143]. The addition of Zn to Pt decreases the CO desorption temperature, suggesting a reduction in the ability of Pt to back-bond, which decreases the strength of the Pt-CO interaction [143] resulting from the Pt $5d$ to $6(s, p)$ rehybridization. A recent density functional theory (DFT) analysis of the bonding in a PtZn alloy [101] (L1$_0$, tetragonal lattice) described the changes in the band structure due to alloying with Zn.

As mentioned in **Chapter 1**, a significant amount of research has focused on the improvement of ORR kinetics by alloying Pt with various transition metals. A systematic study using *in situ* extended X-ray absorption fine structure of dispersed binary Pt alloy catalysts in a fuel cell MEA arrangement [117, 70] indicated specific changes in bond distances and in electronic structure due to the presence of the transition metal. The alloys were primarily of the Pt_3M_1 structure. A decrease in the Pt-Pt bond distance which, correlated with an increase in Pt

5d orbital vacancies, was indicated as the alloying metal was systematically changed from Mn to Ni. These changes were apparently related to the effect of the bulk electronegativity of the alloying metal, where an increase in electronegativity leads to an increase in Pt *d*-band vacancy. However, the use of bulk electronegativity for predicting or interpreting the characteristics of a bimetallic surface alloy has been criticized by Rodriguez [121, 120] with experimental results suggesting that orbital rehybridization at the surface can change the effective electronegativity of the alloying metal as compared to the bulk. The rate of ORR, measured at 0.9 V/SHE, was found to be dependent upon the Pt-Pt bond distance and Pt *d*-band vacancies, exhibiting a maximum for the Pt/Cr alloy. A similar explanation can be invoked for the current Pt/Zn alloy studies. The formation of a Pt-Zn alloy results in orbital rehybridization which creates *d*-band vacancies, resulting in an improvement in ORR kinetics similar to that seen for transition metal-Pt alloys which are currently used. Moreover, the strength of the Pt-Zn bond may result in enhanced stability for the Pt-Zn alloy under operating fuel cell conditions which may mitigate the leaching problem present in many of the Pt alloys currently under study.

An alternative explanation for the improved ORR kinetics on the PtZn surface is by borrowing the ORR mechanisms proposed by Fernandez *et al* [114]. The authors suggested that the adsorption of oxygen molecules occurs on the transition metal component of the alloys, followed by transferring the oxygen to the neighboring Pt sites. This is shown schematically in **Figure 4-13**. Considering 1) the PtZn attracts oxygen more than Zn, but the Zn atoms in the PtZn do not bind to oxygen too strongly, and 2) Zn modification of Pt increases the catalytic activity of the ORR, Fernandez's model may be the explanation for the ORR mechanism on our PtZn surface.
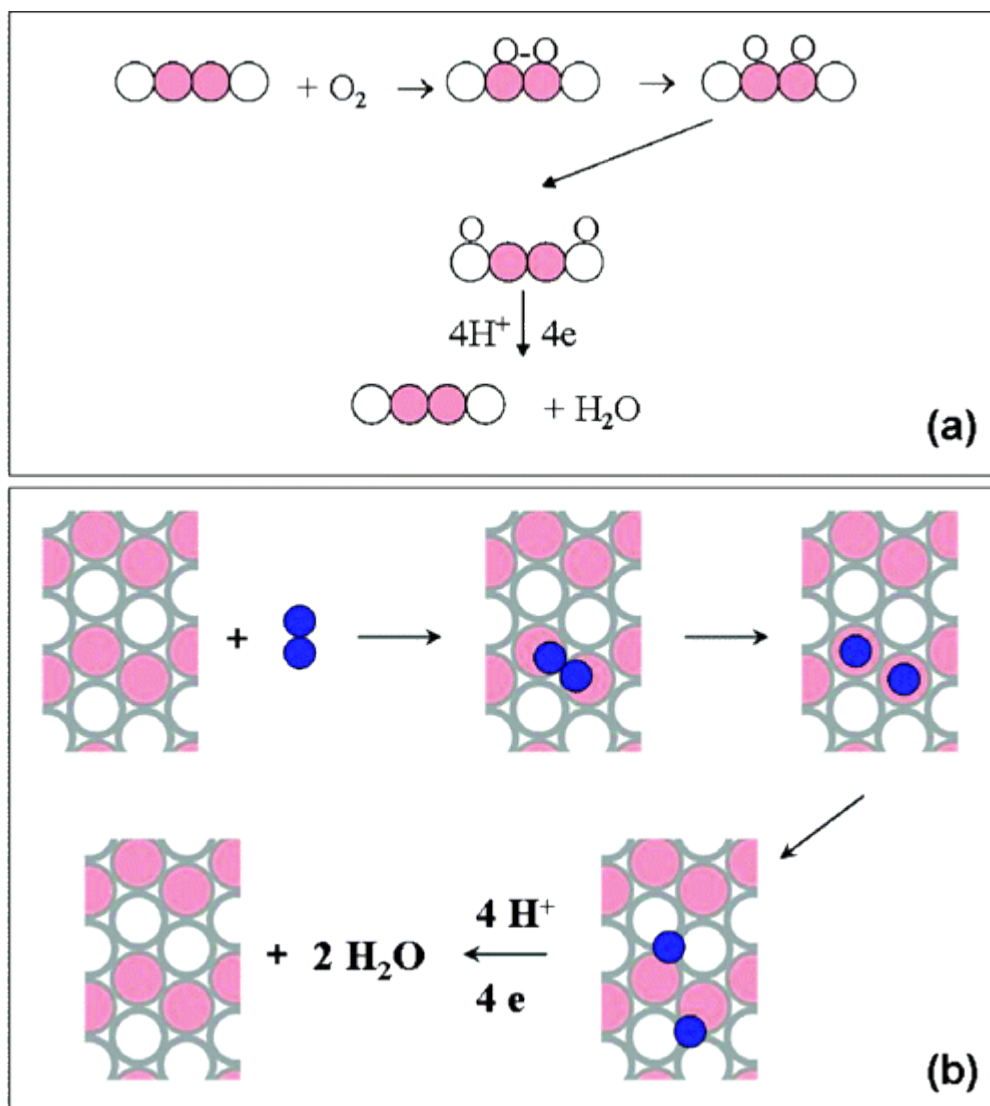
Figure 4-13 ORR mechanisms suggested by Fernandez, *et al.* The oxygen is first adsorbed onto transition metal sites on the surface, followed by a rapid transferring of the oxygen. The gray circles in lattice represent the transition metals, and the dark circles in (b) represent oxygen atoms. The reaction of ORR is believed to improve. Reprinted in part with permission from [114]. Copyright 2005 American Chemical Society.

4.4. Summary and conclusions

This chapter investigated the ORR catalysis on the electrochemically prepared PtZn alloy. The electrochemical deposition of Zn onto a Pt substrate results in the formation of a PtZn alloy. This was confirmed through a combination of electrochemical and AES analytical studies. Interestingly, the oxygen uptake on the PtZn region appeared more efficient than on the pure Zn region. The ORR catalytic activities were measured on both smooth Pt and PtZn surfaces at 22 $^{\circ}$C, and the PtZn showed 30 mV improvement in the onset potential of the reaction. The resulting analysis showed that the Tafel slope was slightly smaller than that measured for smooth Pt. This alloy was also studied in a single fuel cell, where the PtZn GDE was also prepared by the electrochemical deposition of Zn onto a Pt-dispersed GDE. It was found that the MEAs with the Zn-treated cathode gave a 30-70 mV higher cell voltage over the entire range of explored superficial current densities up to 800 mA cm^{-2}.

A possible explanation was presented that changes in the metal's electronic structure through alloying may account for the improved performance. Specifically, addition of Zn may cause a decrease in Pt 5*d*-band occupancy with a 5*d* to 6 (*s,p*) rehybridization and an increase in electron density at the heteronuclear Zn-Pt bond [112]. Our assumption is that this enables an enhanced stability in acidic environments. In fact, the alloy could only be removed through oxidation of the Pt substrate. Such effects may provide a great potential benefit for fuel cell applications.

5.   CO Oxidation Catalysis, Surface Roughness And Restructuring on PtZn

5.1. Introduction

The previous chapter showed that electrochemically prepared PtZn is a promising catalyst candidate for the oxygen reduction reaction (ORR). The ORR catalysis requires adsorption of oxygen onto the catalyst surface as does CO oxidation; an anodic reaction known as a rate determining step for methanol oxidation which is employed in a direct methanol fuel cell (DMFC) [43]. Currently PtRu catalyst is employed in a DMFC which is also an effective catalyst for CO oxidation. PtRu has some similarities to PtZn. According to the work done by Buatier *et al*. [146], PtRu also showed a decrease of Pt ($5d$) electron density and a decrease in CO desorption temperature in a UHV environment; similar to what Rodriguez showed for PtZn [143, 112].

This chapter first describes CO oxidation electrocatalysis on the PtZn. Using an as-prepared PtZn electrode, we observed a significant improvement in the CO oxidation catalysis. However, as shown in **Chapter 2**, surface structures and roughness impact catalytic activity in general. We noticed that the formation of the PtZn alloy significantly roughens the electrode surface compared to the original substrate. Also in the previous chapter, the measured overpotential on PtZn was 30 mV less than on the polished Pt surface, but again, the PtZn surface was much rougher. This roughness has to be compensated. Because we were not able to polish PtZn to a smooth finish as it would remove the surface alloy (approximately 40 layers on the surface; estimated in **Chapter 4**), we deposited Pt particles on a smooth Pt electrode to create an equivalently rough surface to that of PtZn. The comparison between the rough and smooth electrodes is presented.

Also shown is the adsorbate-induced surface restructuring which was electrochemically realized. In **Chapter 2**, the literature review describing the surface atoms rearranging

themselves according to the surface energy changes before and after the adsorption of small molecules, such as CO or oxygen, was reviewed. The evolution of the characteristics of the PtZn surface (roughness, composition) during the various electrochemical treatments (*i.e.*, CO oxidation and ORR) is also presented in this chapter.

5.2. Experimental

5.2.1. Electrochemistry and PtZn alloy formation

Electrochemistry was carried out in a regular three-electrode cell setup similar to that described in **Chapter 3**. The potentiostat (HEKA PG 590) was connected to a data acquisition board (National Instrument; PCI-6052E), and data recorded using LabView in-house written program (National Instrument). The electrolyte was 0.1 M H_2SO_4 prepared with the Milli-Q water. All the potentials are reported with respect to RHE, and the electrochemical data presented in this chapter was recorded at the room temperature (22 $^{\circ}$C).

The working electrodes were either Pt rotating disc electrodes (RDEs) or Pt beads. One set of electrodes was used without Zn modification resulting in Pt electrodes for baseline comparison. For the polished Pt (designated as a "smooth Pt" hereafter), the areas of electrodes were determined by integrating the area under hydrogen adsorption region of CV, assuming the monolayer adsorption charge of 210 $\mu C/cm^2$ [147]. For PtZn, the area was determined by comparing the double layer capacitance of its CVs to double layer capacitance determined from the smooth Pt CVs for which the area is determined using the hydrogen adsorption (H_{ads}) charge (as shown in the example using a smooth Pt and a rough Pt surfaces in **Figure 5-1**). This was required since as we will show, the area under the H_{ads} region is strongly modified by PtZn alloy formation. The CVs for the PtZn alloy were recorded between 0.03 and 1.0 V at 50 mV/s. The upper limit for PtZn electrode was restricted so as to protect the alloy from oxidation which occurs above 1.2 V vs. RHE [106]. Pt and PtZn samples were analyzed in EDX-equipped SEM. SEM images were analyzed using ImageJ (National Institute of Health). Backscattered electron images were obtained in a Microlab 350 using a field emission source of 10 keV, 3 nA, and a

hemispherical analyzer.
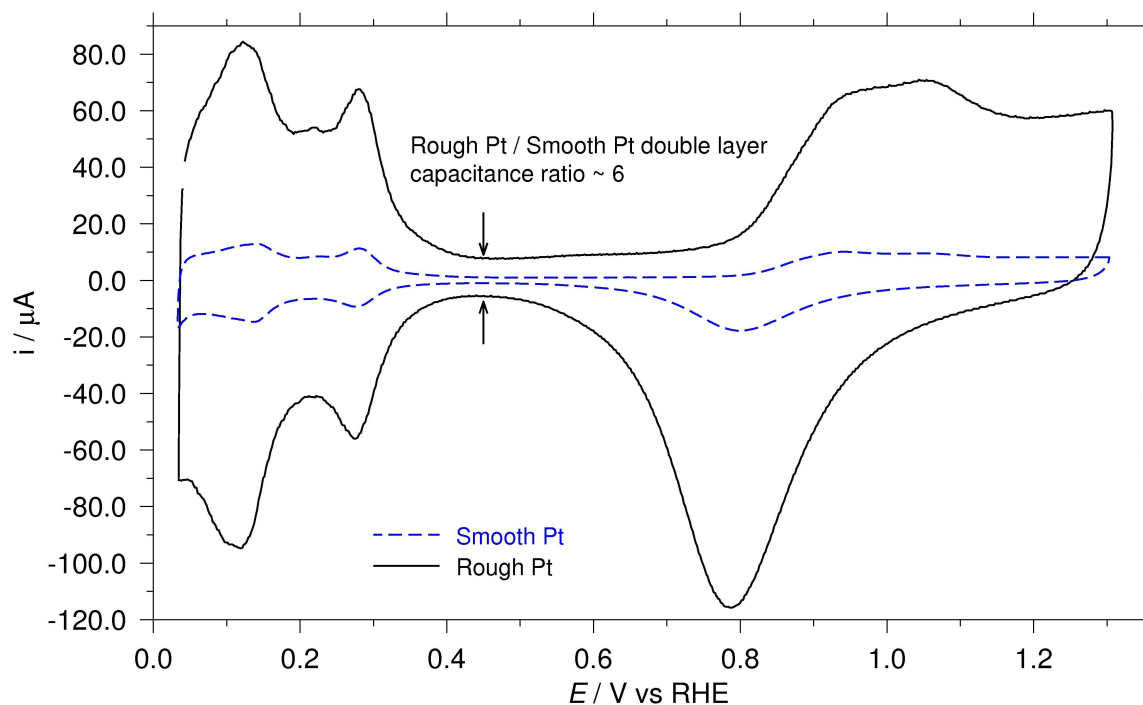
Figure 5-1 The electrode surface area can be determined by measuring the double layer capacitance and comparing it to the one with the known area. The electrode area on the smooth Pt was determined by integrating H_{ads} peaks.

5.2.2. CO stripping voltammetry

The electrochemistry of CO oxidation on both smooth Pt and PtZn surfaces was studied. The 0.1 M H_2SO_4 electrolyte was bubbled with carbon monoxide (Praxair) for approximately 20 minutes after measuring a CV in an Ar saturated solution. This was sufficient time to saturate the solution with CO. Over the electrolyte, Ar flow was always maintained to avoid any oxygen

ingress, important as a trace amount of oxygen will react with CO to form CO_2 [83]. While the experiments were carried out, CO was constantly bubbled into the solution to ensure CO saturation. The smooth Pt or PtZn electrode was then immersed into the solution and polarized at 0.3 V for 1 minute to create a CO saturated surface. The potential was scanned from 0.3 to 1.1 V at 50 mV/s to record the CO stripping voltammograms. All the processes were done under the ambient conditions (Temperature = 22 $^{\circ}$C).

5.2.3. Oxygen reduction reaction

ORR was performed using smooth and rough Pt and PtZn RDEs at 2000 rpm at 22 $^{\circ}$C. The solution was 0.1 M H_2SO_4 saturated with oxygen (Praxair; bubbling for approximately 20 minutes with oxygen surface flow). The electrode potential was swept from 0.3 to 1.05 V at 20 mV/s for both Pt and PtZn. Analysis was performed on anodic scans of ORR curves. Current densities were calculated using the electrochemical surface area, rather than the geometrical areas of electrodes.

5.2.4. Pt electrodeposition

A solution of 0.1 M H_2SO_4 containing 1 mM of H_2PtCl_6 (Aldrich) was prepared with Millipore water. For this section of experiments, the potentiostat used was a USB-interfaced μAutolab (Metrohm, Switzerland). Deposition potential of 0.5 V was first applied for 15 minutes to the Pt RDE electrode and then the surface was further roughened by a second deposition for 30 minutes. The solution was previously deaerated with Ar to reduce the current due to reduction of oxygen. For consistency, we express the roughness of these Pt electrodes based on the capacitance determined in the double layer region (assuming that the capacitance is similar for a rough Pt and the Zn modified Pt surfaces) as compared to that measured for the smooth Pt electrode. Pt electrodeposition was carried out at 22 $^{\circ}$C.

5.3. Results and discussion

5.3.1. The nature of the PtZn surface after electrodeposition

Pt and Zn-modified Pt surfaces were studied using SEM as shown in **Figure 5-2a** and **b**, respectively. It is worth mentioning the samples were left in an ambient condition at least for one week before the measurements. It is obvious from the figure that the Zn-modified Pt surface is covered with white particles, whereas such particles are not seen on the Pt surface. EDX analysis was performed on the Zn-modified surface. On the surface of the particles, we found both Pt and Zn (Zn:Pt atomic ratio of 5:100). A Zn depleted surface indicates that Zn diffuses into the bulk. This issue will be revisited in **Chapter 6** but it appears Zn migrates into Pt with time under ambient conditions. On flat regions of the surface only Pt was detected; Zn was not detected above the instrumental detection limit (0.2 wt %). Also we did not detect oxygen above our detection limit from any part of the surface, indicating ZnO is not present on the surface. On the particles, Zn was present before and after electrochemical analysis at a similar concentration, therefore the electrochemical data recorded on the PtZn electrode presented in this article, whether directly or indirectly, shows a contribution from Zn.

It is very interesting to examine the left hand side of the **Figure 5-2b**. There are three regions covered with different particle densities. On average, the PtZn particle coverage is about 30 %, but on regions i) and ii), the coverages were approximately 80 % and 40 %, respectively. However, Zn was not detected in the bare region iii) above the detection limit. PtZn particles are preferentially found decorating grain boundaries. The SEM image also has two large scratches that cross each other, and they are also decorated more extensively with PtZn, similar to grain boundaries.

Taguchi *et al.*, investigated Zn underpotential deposition (UPD) in 0.1 M sulfuric acid solution onto Pt (111), Pt (110), and Pt (100) surfaces. They observed no significant difference observed on (111) and (100) surfaces with or without the presence of Zn^{2+} in the electrolyte, whereas they clearly observed the formation of Zn UPD layer on a Pt (110)-(1×2) surface [106]. This work suggests Zn preferentially deposits onto particular crystal faces of Pt. Also, a number of articles have shown electrodeposited films with preferred orientations depending on the deposition conditions [148-150] or on the crystallinity of substrates [151]. When the interactions

between substrate atoms and atoms in a deposited film are relatively strong, the crystal structure of substrate affects the resulting structure of deposits [151].
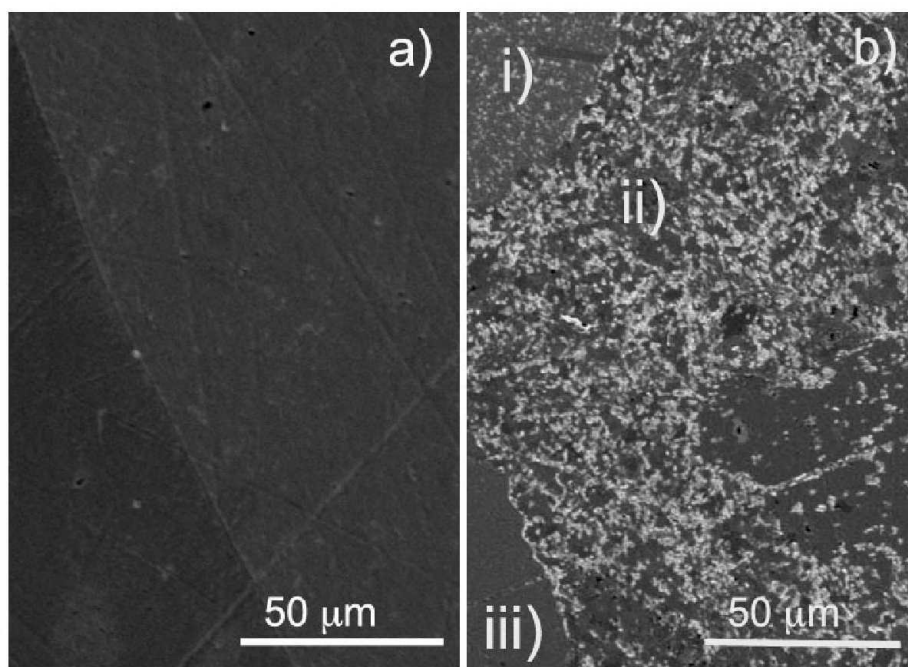
Figure 5-2 SEM images of a) smooth Pt and b) PtZn surfaces. EDX analysis showed both Pt and Zn on the white particles in b), whereas the flat gray part contains only Pt. PtZn particle densities are different and seem to depend on the different Pt surfaces. Region i) and ii) have approximately 40% and 80% coverage, respectively, whereas no particles were seen in Region iii). Reprinted from [8]. Copyright 2009 with permission from Elsevier Ltd.

In **Chapter 4**, we observed a migration of Zn to Pt after leaving the PtZn sample in the UHV chamber for 10 hours. Diffusion of Zn into Pt was further confirmed on the Pt bead surface by backscattered electron detection. Heavy atoms backscatter electrons more than light atoms. The regions containing heavy atoms appear bright in the image. **Figure 5-3** shows both the regular SEM (a) and backscattered SEM images (b) of the same regions of the PtZn

electrode. It was noted the middle white patch in backscattered image showed dark "shadow" around the grain boundaries which gradually fades away from the grain boundary. This indicates Zn is migrating into Pt region from a more Zn rich region resulting in a depleted region of about 1~1.5 μm.

Because the PtZn particles were present only on the surface, and polishing the surface would easily remove them, we carried out our experiments on the alloy without further modification. Therefore, the electrochemical data presented in this contribution was recorded on a rough surface which was considered and compensated for in all electrochemical measurements reported in this chapter.

5.3.2. Ar saturated cyclic voltammograms of Pt and PtZn

Ar saturated CVs recorded on smooth Pt and freshly prepared PtZn in an Ar saturated 0.1 M H_2SO_4 solution are shown in **Figure 5-4** (Also shown in **Chapter 4**). Again, hydrogen adsorption/ desorption ($H_{ads/des}$) regions diminished on PtZn, and an anodic shift in Pt (or PtZn alloy) oxidation potential is also realized. As mentioned in **Chapter 2**, the Pt electrochemical surface area can be determined by integrating the $H_{ads/des}$ peaks; however, the surface area of PtZn could not be reliably determined using the same method; instead, the surface area was estimated by comparing the double layer capacitance of the CV recorded for the PtZn electrode to that of the smooth Pt. This method can estimate the electrochemical surface area within 7.5 % error relative to the surface area determined based on the charge under hydrogen adsorption peaks (confirmed by using the Pt electrode with a varieties of surface roughnesses). Generally, when the PtZn alloy was created, the resulting surface was considerably rougher than the original Pt substrate. The surface area of PtZn (as-prepared) was generally about 10 times larger when comparing the double layer capacitance to that obtained with a smooth polished Pt electrode in the same solution.
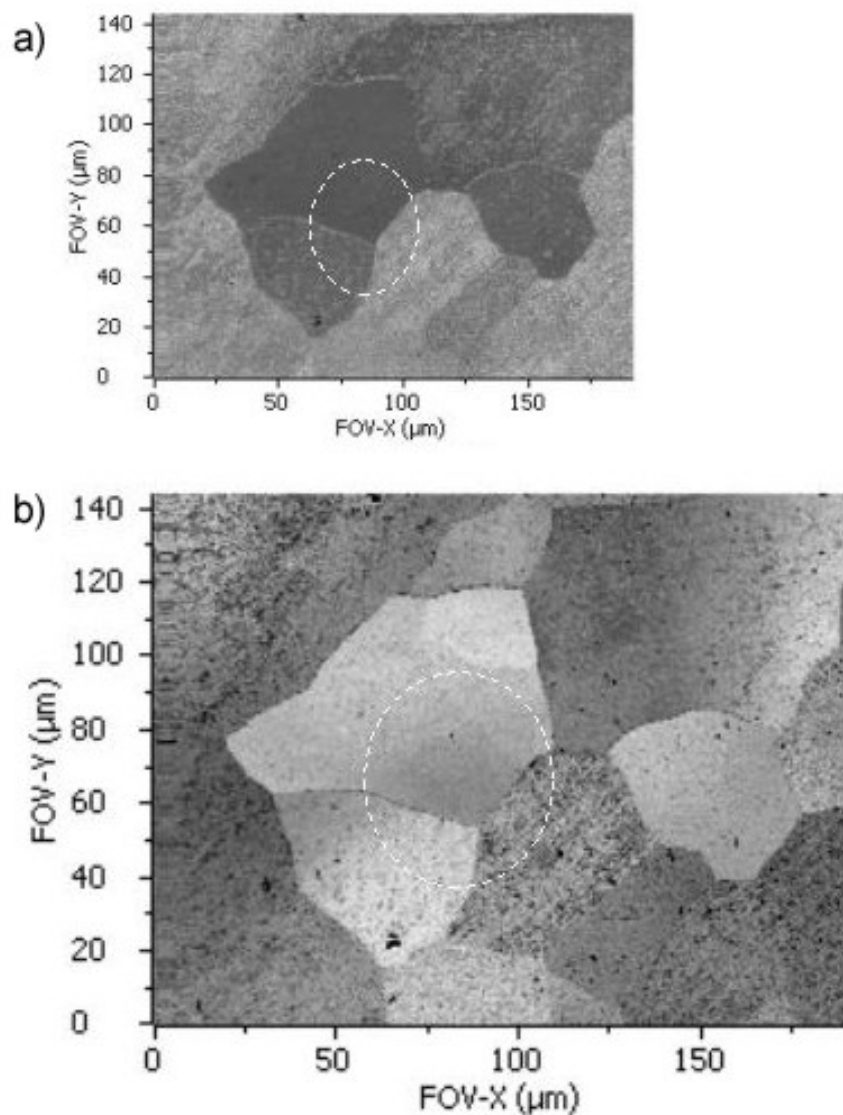
Figure 5-3 a) SEM image of the PtZn bead electrode, and b) backscattered SEM of the same region of the electrode. Backscattered SEM shows heavier atoms in darker colors relative to lighter atoms. The white particles in the regular SEM appear in a darker color in the backscattered SEM, indicating the white particles contain Zn. The grain boundaries appear to be decorated with PtZn. Also the middle bright patch in b) shows in backscattered image showed dark "shadow" around the grain boundaries which gradually fades away from the grain boundary. This indicates Zn is migrating from either the grain boundaries or from the neighboring Zn-rich region into Pt.
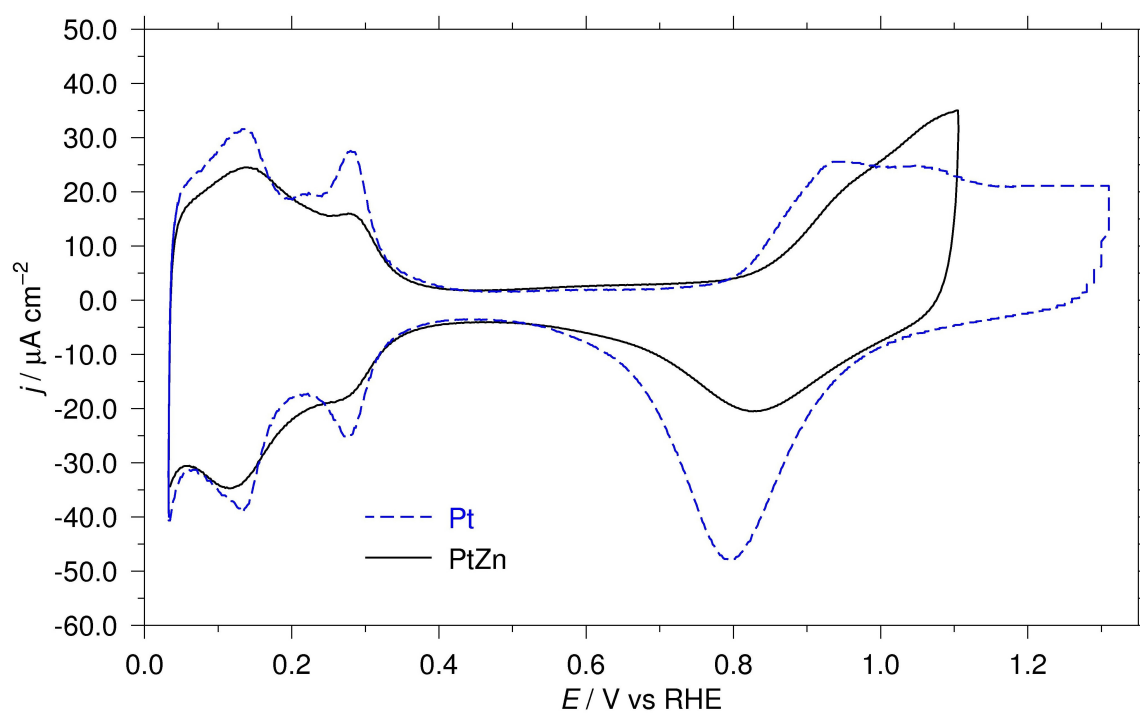
Figure 5-4 Ar saturated CVs of smooth Pt (dotted line) and PtZn (solid line) recorded at 50 mV/s in Ar saturated 0.1 M H_2SO_4 at 22 °C. PtZn electrode shows a positive shift in Pt-oxide formation. Also hydrogen adsorption/desorption peaks on PtZn are diminished. Reprinted from [8]. Copyright 2009 with permission from Elsevier Ltd.

5.3.3. CO oxidation and Pt enrichment of the alloy surface

CO oxidation voltammograms for a smooth Pt surface and a freshly prepared PtZn electrode are shown in **Figure 5-5a**. The CO stripping peaks for the Pt and PtZn were at 0.91 V and 0.75 V, respectively. A 150 mV negative shift was observed with the PtZn electrode. However, when the electrode surface is rough or contains defect sites, the nature of CO adsorption and the oxidation are quite different from a smooth surface, as has been shown theoretically and experimentally [59], and reviewed by Yates [60]. Briefly, Xu *et al*., found that CO oxidation proceeds preferentially on a metal surface containing both step and terrace sites due to both electronic and geometric effects [59].

To investigate if the negative shift was due to the effect of alloying or to the effect of surface roughness, CO stripping voltammetry was also performed on Pt electrodes that were purposely roughened by electrodeposition of Pt onto a smooth Pt surface. Electrodes with two roughnesses were prepared: one is slightly less, and the other is slightly more rough than the surface of the freshly prepared PtZn surface. Relative roughness of each of electrodes was assigned by taking the ratio of the double layer capacitance of roughened surface to that of the smooth Pt. The ratios were 7.89, 6.0, and 8.45 for the PtZn electrode and the two roughened Pt electrodes, respectively. CO stripping voltammetry was then performed on those surfaces. The results shown in **Figure 5-5b** indicate that the shift observed with PtZn was most likely due to surface roughness.

However, an interesting observation was made after either the Pt or PtZn electrodes were immersed into a CO saturated acidic solution and their potentials were scanned between 0.03 and 1.05 V at 50 mV/s over prolonged time (~3 hours; this procedure is designated as "CO treatment" hereafter). **Figure 5-6a** and **b** show the Ar saturated CVs recorded before (curve 1) and after CO treatment (curve 2 to 3 or to 4) on Pt and PtZn, respectively. Each CV presented in **Figure 5-6** was recorded in fresh electrolyte, thereby differences observed among the CVs were not due to the solution contamination. Curve 3 (or 4) experienced more CO treatment than curve 2 (or 3). Both electrodes were RDEs and had well-defined geometric areas. This suggests that the surfaces of both electrodes became smoother after CO oxidation. Further CO treatment on PtZn did not change the electrochemical surface area very much, as measured by the double

layer capacitance (shown in **Figure 5-6c**); however, the hydrogen adsorption/desorption peaks of CVs (E = 0.3 V) after the CO treatment became greatly enhanced, suggesting the surface was becoming Pt-rich, further confirmed by the cathodic shift in the Pt-oxide formation. (shown with arrows in the figure.)
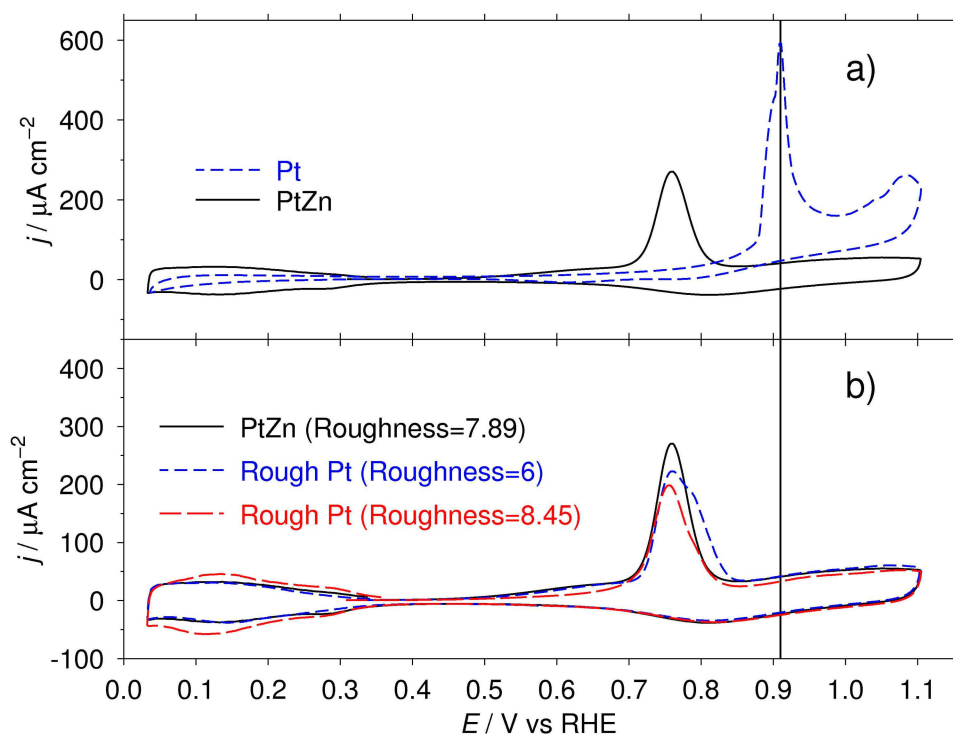
Figure 5-5 a) CO stripping voltammograms recorded at 50 mV/s in CO saturated 0.1 M H_2SO_4 on a smooth Pt (dotted line) and on a PtZn (solid line) electrodes recorded at 22 °C. A 200 mV negative shift was observed on the PtZn electrode relative to Pt; b) CO stripping voltammograms on Pt and PtZn electrodes of comparable roughnesses (recorded in the same manner as [a]). "Roughness" were calculated by comparing the double layer capacitances measured with Ar saturated CVs to that of smooth Pt. The negative shift in the CO stripping peak observed with PtZn in a) was purely due to roughness. Reprinted from [8]. Copyright 2009 with permission from Elsevier Ltd.
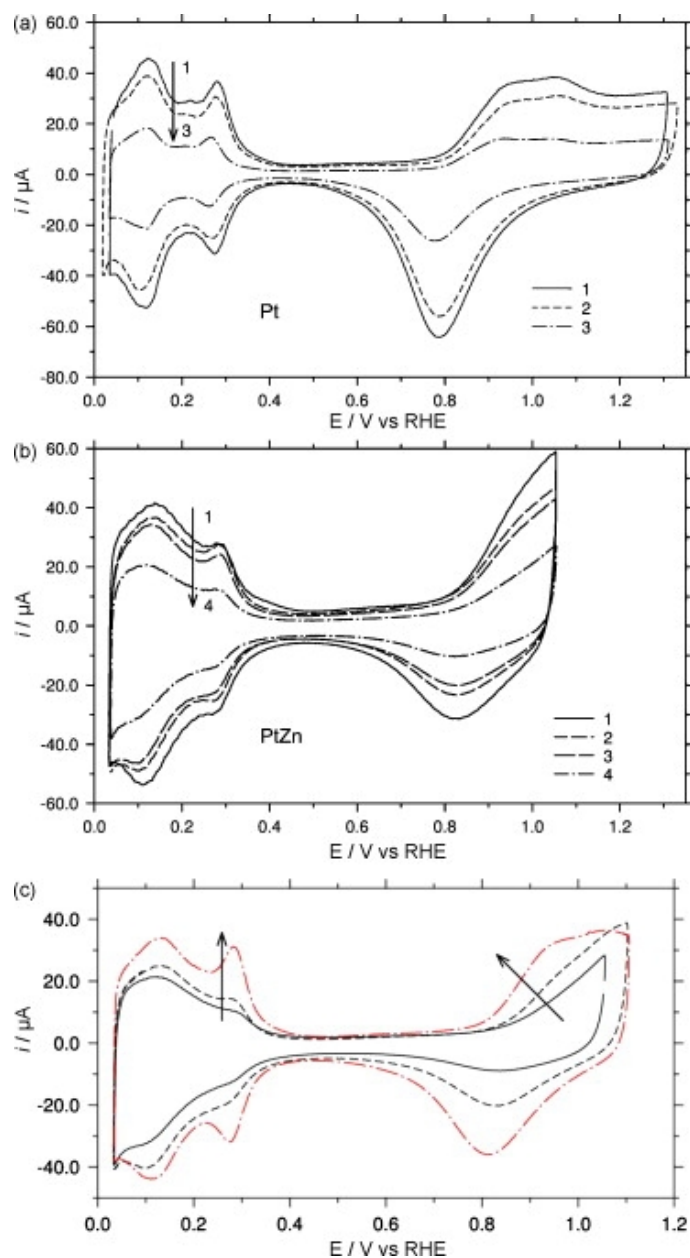
Figure 5-6 Ar saturated CVs recorded with a) smooth Pt and b) PtZn. All CVs presented in here were recorded at 50 mV/s in fresh electrolyte (Ar saturated 0.1 M H_2SO_4). On both electrodes, the charge under the CVs decreased as more CO-treatment was applied, suggesting the surface became smoother.; c) CVs recorded (in fresh electrolyte) on PtZn after further CO-treatment was applied. Pt oxide formation was shifted negatively, and hydrogen adsorption/desorption peaks were enhanced (indicated by arrows), suggesting the surface became Pt-rich after CO-treatment. Reprinted from [8]. Copyright 2009 with permission from Elsevier Ltd

Figure 5-7 shows the CO stripping voltammograms on the PtZn electrode recorded on the same days as curves 1 - 4 in **Figure 5-6b** were obtained (designated as Day 1 - 4). A dotted line at 0.92 V corresponds to the potential of the stripping peak recorded on a smooth Pt surface. The voltammogram for Day 1 was recorded with a freshly prepared PtZn electrode before CO treatment was applied. Each successive day (after CO treatment for ~ 3 hours), the main CO stripping peaks shifted to more positive potentials, with the stripping curves also changing shape. As expected from the CVs shown in **Figure 5-6b**, the charge under the voltammograms also diminished with time. On Day 1, there is only one peak observed at E = 0.77 V, but on Day 2, CO stripping occurred over a wider potential range, with the main peak at about 0.83 V with a shoulder at 0.78 V. On Day 3, no shoulder was observed in the stripping curve, but the main peak appeared at a potential between the peak and the shoulder observed on Day 2. On Day 4, the main peak was observed at a more positive potential than that of Day 3. This also shows that the surface is changing with CO-treatment, and it appeared that the surface of PtZn was becoming smoother and more Pt-rich – consistent with our observations from **Figure 5-6**. It was also noted that the charge density during CO stripping experiments generally increased as the electrode was exposed more to CO. The charge passed during CO oxidation was determined by integrating the CO stripping peaks and shoulders, if applicable, and **Table 5-1** shows the electrochemical surface areas and charge densities determined by the method outlined in reference [55].

As mentioned in **Chapter 2**, Rodriguez *et al.*, performed CO temperature programmed desorption studies on PtZn surface and found CO desorption temperature was less than that measured for Pt, suggesting that incorporation of Zn into the surface of the metal decreased substrate-CO interactions [112]. This supports our conclusion that with CO-treatment, the surface becomes more like Pt. Also, the surface reorganization may occur if the interaction between the adsorbates and surface atoms are stronger than the interaction between the atoms in the surface [152]. For example, Gritsch *et al.,* observed the reorganization of Pt(110) surface from (1×2) to (1×1) after CO was adsorbed onto the surface [64]. It is likely that the PtZn surface is also going through a surface reorganization similar to these reports. Arenz *et al.,* investigated the CO oxidation catalytic behavior on Pt nanoparticles [152]. As part of their electrode cleaning procedure, they compared two methods: "Oxide annealing" and "CO annealing". The potential of the electrode was scanned in an Ar saturated acidic solution for the

"oxide annealing procedure", whereas the potential was cycled in the CO saturated solution in the "CO annealing procedure". They previously found CO annealing removed the surface irregularities similar to flame annealing. They recorded current transient curves for CO oxidation with the electrodes pretreated by the two different annealing methods and found that the nucleation and growth process for OH_{ads} occurred more slowly on CO annealed electrode than on oxide annealed electrode. This indicated that the CO annealed sample had a lower active site density than the oxide annealed sample due to a smoother surface after the annealing process.
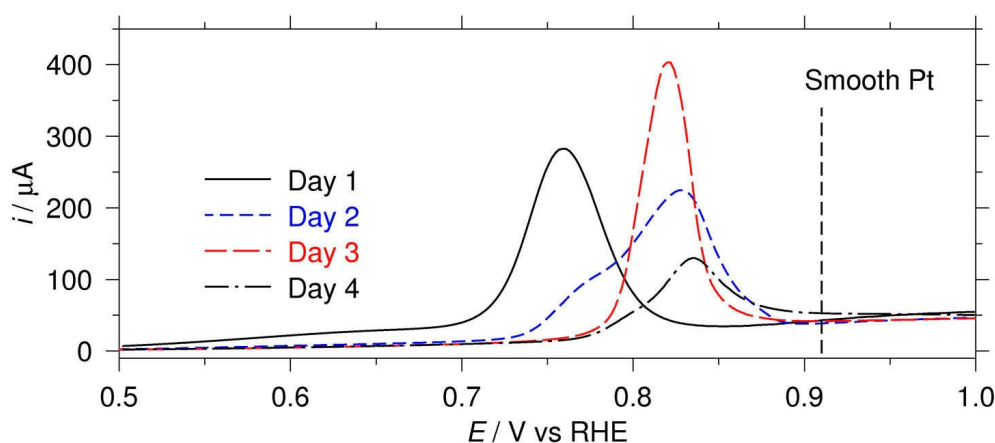
Figure 5-7 CO stripping voltammograms recorded at 50 mV/s in CO saturated 0.1 M H_2SO_4 (22 ºC) on PtZn electrode over four days. CO-treatment was applied for approximately 3 hours on the electrode on each day. The dotted line at 0.92 V corresponds to the CO stripping peak on smooth Pt. As more CO-treatment was applied the stripping peaks recorded on PtZn were moving towards the peak potential measured on smooth Pt. Reprinted from [8]. Copyright 2009 with permission from Elsevier Ltd.

Shoulders on the CO stripping peaks shown in **Figure 5-7** have been observed. Cuesta *et al.,* reported a CO stripping voltammogram similar to the curve recorded on Day 2 and concluded that the shoulder corresponds to the oxidation of bridge-bonded CO, whereas the main peak corresponds to the oxidation of linearly-bonded CO [53]. Therefore it is possible that as the PtZn surface changed with CO-treatment and more sites for bridge-bonded CO were created.

Table 5-1 Electrochemical surface areas and the charge densities of CO stripping voltammograms on a smooth Pt electrode and a CO-treated PtZn electrode (over 4 days). As PtZn electrode was treated with CO, the electrochemical surface areas decreased and the charge densities increased. Reprinted from [8]. Copyright 2009 with permission from Elsevier Ltd.
* Calculated based on the double layer capacitance.

Type of electrode	Electrochemical surface area* (cm^2)	Charge density (μC cm^{-2})
Smooth Pt	0.097 ± 0.007	6.17×10^2
PtZn (Day 1)	1.04 ± 0.08	4.44×10^2
PtZn (Day2)	0.85 ± 0.06	4.56×10^2
PtZn (Day3)	0.79 ± 0.06	5.12×10^2
PtZn (Day 4)	0.52 ± 0.04	6.08×10^2

5.3.4. ORR and Zn enrichment of the alloy surface

Pt enrichment of the PtZn surface was observed after CO-treatment. In **Figure 5-6c**, H_{ads}/ H_{des} peaks were enhanced after the treatment. We also realized Pt-oxide formation on PtZn was shifting cathodically as more CO-treatment was applied, similar to what we observed in **Figure 5-4** when CVs of Pt and PtZn were compared. In the previous chapter, we observed improved kinetics in ORR with our PtZn alloy as a catalyst compared to Pt. This improvement may be correlated to the potential shift in the oxide formation. Stamenkovic *et al.*, showed the same trend for Pt_3Co and Pt_3Ni [26]. As shown, however, the PtZn surface became rough once the alloy was formed. It is known that oxygen dissociation catalysis on a rough surface is significantly different than on a smooth surface. Adsorption and subsequent dissociation of oxygen molecules on Pt surfaces have been extensively studied [41, 40], showing that a Pt surface having steps and terraces exhibits more O_2 adsorption/dissociation at step sites due to the stabilization of the dissociated transition state. This is due to the higher coordination number for Pt atoms on terrace sites than those on step sites [42]. Work reported by Gee *et al.*, showed that the difference in the extent of oxygen dissociation process between Pt (111) (no step sites) and Pt (533) (with step sites) was governed by the presence of defects or steps [41]. Maciá *et al.*, also observed higher current on Pt(*n*+1, *n*-1, *n*-1) surface (*i.e.,*, contains steps) than on Pt(2*n*-1,11) surface (*i.e.*, contains more terraces) during ORR [27]. They also showed Pt electrodes with different crystal structures exhibited significantly different kinetics for ORR.

The comparison made on the ORR curves, presented in **Figure 4-9** was between PtZn (with a rough surface) and a smooth Pt surface. To ensure a reasonable comparison, the ORR on the PtZn electrode was compared to the roughened Pt electrode which had a slightly rougher surface than the PtZn electrode. The ORR anodic scans for the roughened Pt and the PtZn electrodes are shown in **Figure 5-8** including an ORR curve recorded for a smooth Pt electrode. The rough Pt surface showed a +15 mV shift at the current density of -1.0 mA/cm^2 compared to smooth Pt. On the other hand, the ORR onset potential for PtZn was approximately 35 mV more positive at the current density of -1.0 mA/cm^2 compared to the smooth Pt electrode. Gambardella *et al.*, reported that having a Pt surface with step and terrace sites show much more pronounced ORR kinetics than on a Pt surface with only terrace sites. However, the authors also

discovered that when the stepped sites were decorated with Ag, the reactivity of the sites towards oxygen dissociation decreased. They found that the amount of oxygen adsorption decreased even though Ag did not physically block Pt atoms at the edge, indicating an electronic perturbation caused by Ag adjacent to Pt atoms [42]. Together with Gambardella's work, our observation strongly suggests that the shift is due to both roughness and electronic perturbation, which resulted from the formation of a PtZn alloy. Once compensated for roughness, it is convenient to use the shift in onset potential for ORR as an indication of the the presence of PtZn alloy on the surface of the electrode.
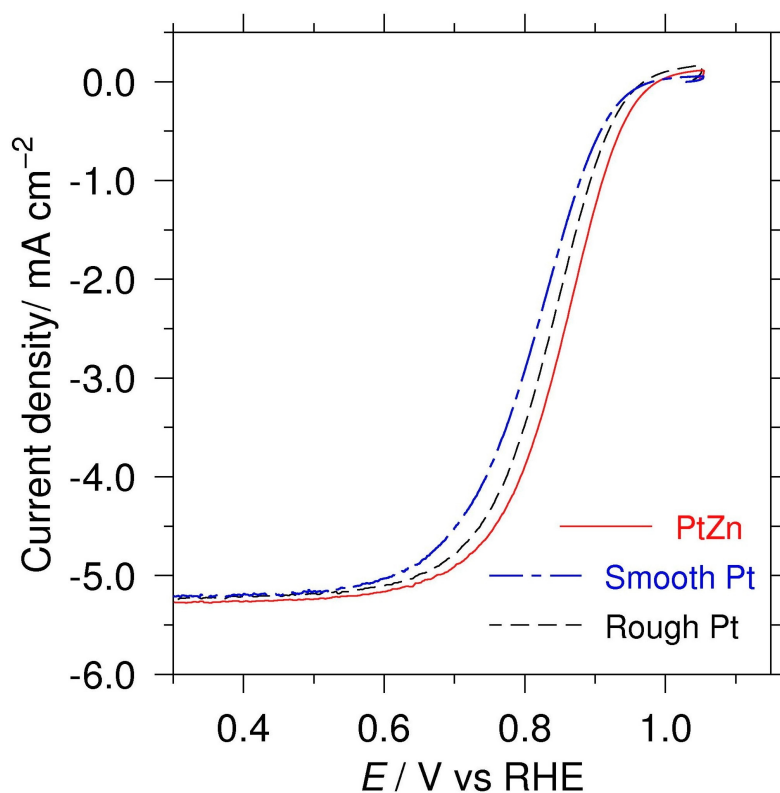
Figure 5-8 ORR curves recorded at 20 mV/s with the rotation speed of 2000 rpm in oxygen saturated 0.1 M H_2SO_4 (22 ℃)on smooth Pt, rough Pt, and PtZn electrodes. Roughnesses of PtZn and "rough Pt" are equivalent. The rough Pt showed a 15 mV positive shift, whereas PtZn showed a 35 mV positive shift, compared to the smooth Pt electrode at current density of -1.0 mA/cm². Reprinted from [8]. Copyright 2009 with permission from Elsevier Ltd.

ORR voltammograms were recorded before and after CO treatment. **Figure 5-9** shows ORR curves recorded on Pt and PtZn RDEs before (solid line) and after (dashed line) CO treatment. Polarization curves for Pt were identical before and after CO treatment, whereas PtZn showed a slight negative shift after the electrode was treated with CO. This negative shift also suggests Pt enrichment of the alloy surface after CO treatment.
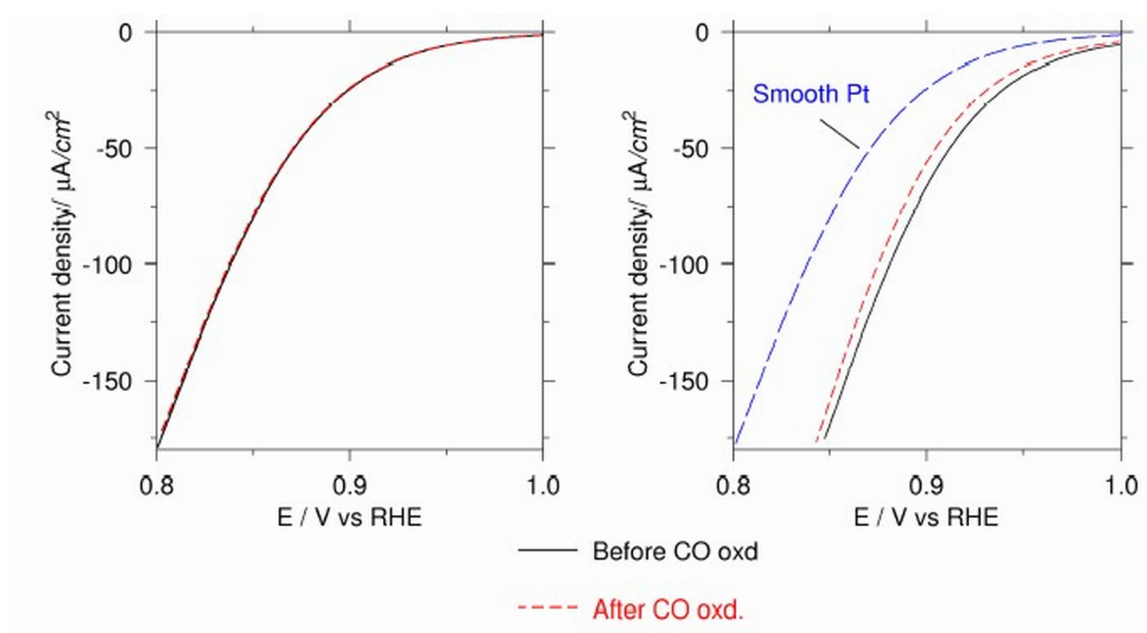
Figure 5-9 ORR curves in kinetic-limited regions recorded at 20 mV/s with the rotation speed of 2000 rpm in oxygen saturated 0.1 M H_2SO_4 (22 $^\circ$C) on smooth Pt and PtZn electrodes before (solid line) and after (dotted line) CO-treatment. ORR curve recorded on the smooth Pt surface is plotted on the PtZn graph for comparison. There is a slight negative shift observed after CO-treatment was applied to the PtZn surface. Reprinted from [8]. Copyright 2009 with permission from Elsevier Ltd.

The apparent Pt enrichment of the surface may be due to loss of Zn from the surface, or by changing the surface composition through segregation. Shen *et al*., observed an adsorption-induced site exchange phenomenon on Al alloyed with Pd(001) [153]. During temperature annealing above 800 K (as a part of the alloy-formation process), the authors found that Pd formed a "skin" over the surface, and it remained on the surface when the temperature of the substrate was dropped to room temperature. However, when the alloy was exposed to a significant amount of oxygen, Al segregated to the surface. This process was reversible; Al migrated back into the bulk when oxygen was desorbed from the surface. They did not observe the same phenomenon when CO adsorbed onto the alloy surface. They explained this observation realizing that the formation of Al-O bonding is energetically favoured over Pd-O bonds and exposure to oxygen resulted in a site exchange [153]. According to this report, site exchange between atoms in the bulk and on the surface is certainly possible, and the composition of the surface is determined by the strength of metal-adsorbate interaction. We have already demonstrated Pt enrichment on the surface due to CO adsorption, but it is also reasonable to predict oxygen adsorption may enrich Zn at the surface.

The influence of ORR on the behavior of a PtZn surface was studied after various treatment regimes. **Figure 5-10** shows the ORR curves at low current regions recorded on the PtZn electrode previously exposed to CO for an extended period of time (labeled PtZn 1 in **Figure 5-10**). The same electrode was then exposed to an oxygen saturated solution and the potential was scanned between -0.3 and 1.05 V at 20 mV/s for several hours. Another ORR polarization curve was measured (labeled PtZn 2). The electrode was immediately re-exposed to CO saturated solution, and the potential was swept between 0.03 and 1.1 V at 50 mV/s for several hours. At the end of this experiment, another ORR polarization curve was recorded (labeled PtZn 3). The ORR onset potentials on the PtZn electrodes were slightly different, with PtZn 2 showing the lowest overpotential.

From our previous observations, the surface of an electrode becomes Pt-rich when it is CO-treated. The same is observed in **Figure 5-10**; previously CO treated PtZn electrode shows the onset of ORR closer to that of smooth Pt. On the other hand, when the electrode was exposed to oxygen for prolonged time, the onset of ORR occurred at a higher potential. Han *et al.,* used density functional theory and Monte Carlo simulations to study the surface state of PtRu(111) as oxygen adsorbed onto the alloy surface. Under a vacuum environment, Pt migrates

towards the surface forming a Pt-skin. The authors found that though the atomic arrangements of Pt, Ru, and O are different depending on the chemical potentials of each atom, Ru generally migrates towards surface when oxygen is adsorbed onto the alloy surface. As in the same argument made by Shen *et al.*, the authors concluded that the strong interaction between Ru and O overcame the Ru surface energy which by itself is higher than that of Pt [154]. Shen *et al.*, reported Al migration towards surface as the PdAl alloy surface was exposed to oxygen. Their explanation was simply that the enthalpy of formation of Al_2O_3 was much more negative than the corresponding constant of PdO [153]. We can make the same argument in our PtZn surface reorganization. $\Delta H^o_{formation}$ of ZnO is -350.5 kJ/mol [155], whereas $\Delta H^o_{formation}$ of PtO_2 is -80 kJ/mol [156] showing that Zn will be preferentially segregated to the surface due to a stronger interaction with oxygen.
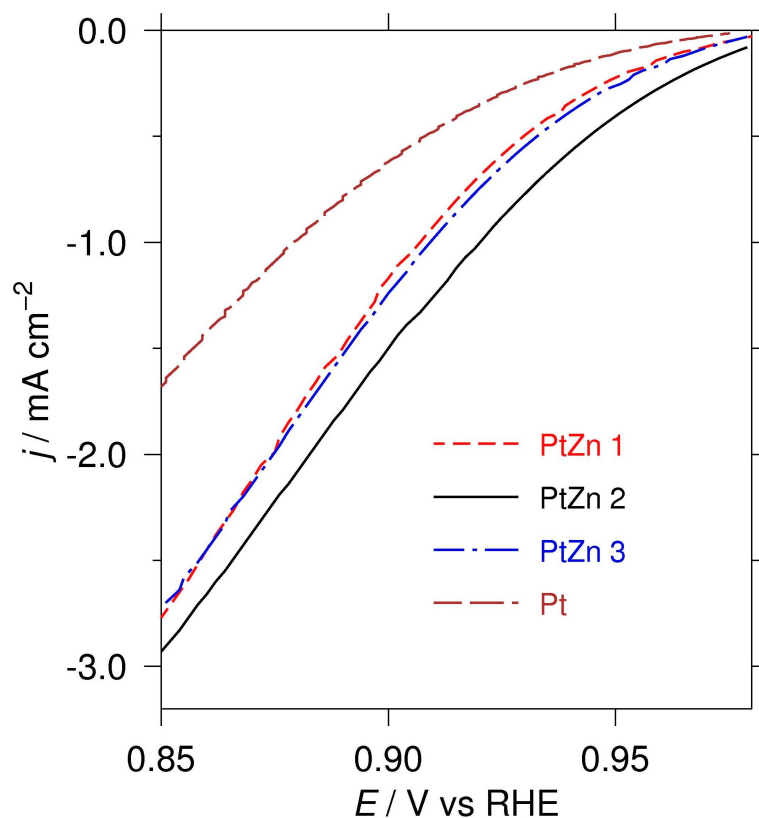
Figure 5-10 ORR polarization curves recorded at 20 mV/s with the rotation speed of 2000 rpm in oxygen saturated 0.1 M H_2SO_4 (22 ºC) on PtZn that has been treated with CO (PtZn 1), then with oxygen (PtZn 2), and then retreated with CO (PtZn 3). Negative shift in the onset potential of ORR on PtZn after CO treatment was reproducible. ORR curve recorded on a smooth Pt surface is shown for comparison. Reprinted from [8]. Copyright 2009 with permission from Elsevier Ltd.

Another possible explanation for the decrease in the onset potential after CO-treatment is surface smoothing. Molecular oxygen adsorption and subsequent dissociation is more facile on a rough surface than on a smooth surface as discussed earlier. Since CO-treatment makes the alloy smoother, this might have decreased the amount of oxygen adsorbed on the surface of the PtZn alloy. In fact, Lebedeva *et al.*, has studied the CO oxidation on a Pt surface containing both steps and terraces and concluded that oxidation reactivity is enhanced at the step sites because oxygen-containing species adsorption preferentially occurs at step sites rather than at terrace sites [157]. This suggests concentration of oxygen adsorbed at step sites is higher than at terrace sites, which may be related to the fact oxygen dissociation preferentially happens at step sites [41]. Losing these step sites by CO-treatment will decrease the ORR onset potential. Our observation in **Figure 5-10** also suggests that the PtZn surface becomes rougher after oxygen-treatment. Nevertheless, the extent of shifts observed in onset potentials of ORR after CO-treatment or oxygen treatment was very reproducible, indicating the site exchange between Pt and Zn occurred within the metal. Therefore, we believe it is unlikely that the negative shift after CO treatment was due to irreversible loss of Zn from the electrode surface.

5.3.5. Surface reorganization and the CO oxidation reaction mechanisms

Both CO- and oxygen-treatments of the PtZn alloy have altered its surface, which subsequently led to a change in the adsorption of oxygen or CO. As mentioned in **Chapter 2**, Buatier *et al.*, and Rodriguez *et al.*, showed a decrease in Pt($5d$) electron density and a decrease in CO desorption temperature on PtRu and PtZn alloys, respectively, compared to pure Pt [112, 146]. In fact, these changes have also been observed with Pt_3Co [76], PtTi [115, 77], and PtMo [116]. These Pt-alloys have been reported to enhance ORR catalysis compared to pure Pt, but only PtRu has been experimentally well-known to improve CO oxidation catalysis relative to Pt. This may be related to the site exchange process. The adsorption energy of CO onto Pt(111) surface is determined to be -1.39 ~ -1.43 eV[81]. On pure Zn, however, no adsorption of CO was observed [119]. On pure Ru(0001), CO adsorption energy was reported as -1.70 eV [81]; similar to that on Pt. For PtZn exposed to CO, Pt migrated to the surface, leaving Zn in the bulk. In the case of PtRu, because CO adsorption energies on both atoms are very similar, the surface

composition does not change dramatically. Bifunctional theory suggests that Ru provides -OH$_{ads}$ to neighboring Pt sites [82] which is reasonable since the binding energy of -OH onto Ru is approximately 5 times greater than on Pt [81]. The observed site exchange occurring on PtZn may add to the developing picture addressing the mechanism of ORR (or CO oxidation) on Pt alloys, which is currently explained by a decrease in Pt (5d) electron density, the electronegativity of admetals, and decrease in the Pt-Pt bond distance [74].

5.4. Summary and conclusions

The work described in this chapter details the roughness-compensated CO oxidation and the ORR electrocatalysis on the Pt and PtZn surfaces. PtZn showed no improvement on the CO oxidation catalysis as compared to Pt. Apparent enhancement in catalytic activity on PtZn compared to smooth Pt was purely due to the roughness of the PtZn surface. On the other hand, PtZn showed a better catalytic activity for ORR compared to Pt surface of equivalent roughness. Moreover, we observed Pt-enrichment and smoothing on the PtZn surface after extended CO-oxidation, whereas we observed Zn-enrichment and possible roughening of the surface after extended oxygen-reduction.

Comparing Ar saturated CVs of Pt and PtZn in sulfuric acid, there was approximately 80 mV anodic shift at current density of 20 μA/cm^2 in the onset of Pt-oxide formation for PtZn. SEM-EDX confirmed the presence of Zn on the Zn-modified Pt surface before and after electrochemical treatments were applied. SEM also showed that Zn modification of Pt produces a rougher surface and the preferential formation of PtZn on various surface regions.

Segregation of selected atoms to the surface was explained by simple thermochemical effects. More detailed studies on the surface segregation effect, composition of Zn-modified Pt surface, and the stability of PtZn are presented in the next chapter.

6. Stability of PtZn Alloy in Acidic Aqueous Environment

6.1. Introduction

A number of Pt-alloy catalysts have demonstrated an improvement in kinetics of ORR. Many of them have been tested in fuel cells and also shown promising results. However, one of the challenges researchers have faced upon developing fuel cells is the chemical stability of catalysts [26, 97]. During fuel cell operation, the non-precious metal components of the Pt-alloys typically leach out into the electrolyte, leading to five unfavourable outcomes: 1) decrease in ionic conductivity of membrane due to dehydration as cation contaminants take water away from membrane [158]; 2) increase in ionic resistivity in the cathode due to blocking of cation exchange sites; 3) decrease in oxygen transport to the catalyst layer; 4) damaging the membrane if a certain metals, such as Ti or Fe, are released [97]; and 5) decrease in catalytic activity [159].

As shown in **Chapter 2**, the stability of PtZn alloy in an acidic condition is theoretically quite promising and, if so, this is an advantage for the fuel cell application. This chapter investigates the chemical stability of PtZn under conditions similar to an operating fuel cell. There are three sections to this chapter; the first two are the results of preliminary stability tests, with more concrete experimental results at the end. They all involve applying a prolonged polarization (*i.e.*, constant potential) to PtZn in acidic electrolyte. The first experiment was performed by Ms. Olivia Ye as the fourth year Honours project which was supervised by Dr. Bizzotto and myself. Stability of the alloy was tested by weighing the alloy before and after polarization, looking for evidences of weight loss due to leaching. The second part involved determination of the concentration of Zn in the electrolyte after the polarization using anodic stripping voltammetry. Unfortunately these two sets of experiments did not provide us convincing results on the stability of PtZn.

The last section of this chapter investigates the chemical stability of a PtZn alloy particles dispersed onto a glassy carbon (GC) substrate. This section builds upon our findings in

Chapter 5. Those results indicated that the PtZn surface became enriched with Pt upon interaction with CO, while Zn segregated to the surface upon the interaction with oxygen. Previous work was performed on large Pt samples which resulted in uncertainty in the surface concentration of Zn; both the concentration of Zn and the possible Zn dissolution. A GC substrate will be used instead of bulk Pt in this chapter. When we analytically observed the decrease in Zn concentration in the alloy in Chapter **5**, we were unsure if Zn was leached out into solution or diffusing deeper into the Pt substrate. However, Zn does not appear to react or form an alloy with carbon under the conditions used [106], so Zn will not persist on the substrate. The use of small nanoparticles of Pt on GC would improve our ability to determine the fate of the Zn atoms in the alloy under electrochemical environments. We predicted that, for small particles at a fixed applied potential, the surface concentration of Zn would increase until it reached an equilibrium concentration. If the alloy is stable, the surface concentration would eventually plateau. If the alloy is unstable, the surface concentration would initially increase but quickly decay due to constant Zn dissolution, leaving only Pt on GC substrate. The surface concentration of Zn was determined by Auger electron spectroscopy (AES) and the bulk composition was determined by dissolution of the remaining metal and analysis by inductively coupled plasma mass spectroscopy (ICP-MS).

6.2. Experimental method:

6.2.1. Preliminary test 1 – Gravimetric determination of Zn loss

This section investigates the stability of PtZn by measuring the weight loss before and after the stability test, *i.e.,* polarizing PtZn foils. This set of experiment was performed by Ms. Olivia Ye as her 4th year Honours project at Department of Chemistry, University of British Columbia, supervised by Dr. Dan Bizzotto and myself.

6.2.1.1. Preparation of PtZn foil

Three Pt foils (25 μm 99.99% Alfa Aesar) were cut into 2 cm by 0.4 cm strips. The weight of each foil was measured using a microbalance (Mettler, Toledo) with accuracy of 0.1 μg. To ensure accuracy, the foils were heated at 150 ^{o}C overnight, followed by cooling in a desiccator to eliminate moisture. PtZn alloy was formed on the foils as outlined in **Chapter 3**. After Zn deposition, the foil was removed from the solution, rinsed with Millipore water, dried with Ar, and was left under Ar atmosphere for 1 hour. Then the foil was either immersed into the acidic solution to the strip remaining Zn from the surface or placed in a 300 ^{o}C furnace overnight. The latter step was introduced to deposit a large amount of Zn into the Pt foil. After heat treatment, unreacted Zn was then removed with warm acid mixture of HNO_3 and H_2SO_4. The sample was then dried in 150 ^{o}C oven overnight. The foils were again weighed on the microbalance (after cooling in a desiccator) and the difference in mass before and after Zn deposition was determined.

6.2.1.2. Stability test

The PtZn foils thus prepared were then immersed into a 0.1 M H_2SO_4 solution. It was necessary first to remove un-alloyed Zn that was driven into the bulk of the foil. All the foils were first polarized at 0.5 V for 36 hours. In a fresh electrolyte, the foils were then polarized at 0.5, 0.75, and 1.0 V for 2 h and 24 h in an oxygen saturated 0.1 M H_2SO_4 solution at 22 ^{o}C. The foils were then removed from the solution, washed with the acid mixture and water, dried in a 150 ^{o}C oven overnight, and weighed on a microbalance. The amount of Zn lost during the polarization process was determined by comparing the weights before and after polarization.

6.2.2. Preliminary test 2 – Determination of Zn loss by anodic stripping method

Platinum foil (polycrystalline) of 25 μm thickness (Alfa Aesar, MA 99.99%) was cut into three strips of 1 by 5 cm sheets. The electrochemical deposition of Zn onto these Pt foils was performed as outlined in **Chapter 3**. The potentiostat used was the μAutolab (EcoChemie). Zn deposition/stripping processes were repeated for ten times to ensure a copious amount of PtZn alloy was formed on the foil. The amount of Zn that presumably alloyed with Pt was calculated by taking the difference between the charge measured for deposition and stripping in the current transient curves. The stability test was carried out in a similar manner to the Preliminary test 1 for 12 hours, but after the polarization, the foils remained in the same solution for another 12 hours under ambient conditions without any applied potential. The Zn concentration in the electrolyte was examined.

6.2.2.1. Anodic Stripping- differential pulse voltammetry

Anodic stripping voltammetry (ASV) analysis was performed on a commercially available glassy carbon rotating disc electrode (GC RDE) (Metrohm, Switzerland). The electrode was first polished slightly with 4000 grit sandpaper to ensure a fresh surface, followed by 6 μm and 1 μm diamond slurry. A 50 mL of an acetate (Fisher Scientific) buffer solution (pH 4.5, 0.15 M), containing 2.294×10^{-3} M Hg^{2+} (Bethlehem Apparatus Co., PA) dissolved in nitric acid, was measured into the electrochemical cell with 5.00 mL of the electrolyte solution in which the stability test was performed and 30 μL Cd^{2+} solution (7.91×10^{-4} M, $Cd(NO_3)_2 \cdot 4H_2O$, Fluka) as an internal standard. First, the GC electrode was rotated at 1000 rpm and polarized at –0.2V for 60 seconds in the acetate buffer/Hg solution (deaerated with Ar gas) in order to deposit only Hg onto the electrode. The Zn^{2+} was reduced into the Hg film using a 50-second deposition at –0.9 V and a 7 second equilibration (*i.e.,* stopping the rotation). The potential was then swept positively (to -0.1 V) at a sweep rate of 20 mV/s to oxidize Zn and Cd from the Hg thin film. The differential pulse method was carried out using a modulation time of 0.005 sec, the interval time of 0.1 sec, and the modulation amplitude of 10 mV. At the end of each run, the electrode

was polarized at 1.0 V to strip off deposited Hg from the GC surface. Also, after one ASV run, the electrode was then removed from the solution and sonicated in a methanol and water mixture to ensure the surface of the electrode was clean before the next deposition of a fresh Hg film. The concentration of Zn was determined by the standard addition method.

6.2.3. PtZn nanoparticle stability test:

6.2.3.1. Pt particle deposition

The working electrode was a GC (Tokai Carbon) substrate machined in a "top hat shape" with a surface area of 1.23 cm^2, as shown in **Figure 6-1**. Each substrate was polished with 4000 grid sandpaper, followed by 6 μm and 1 μm diamond slurry. It was then accommodated into a home-made electrode holder, also shown in **Figure 6-1**. The substrate was placed on a shaft where the bottom face contacts an aluminum plate. The substrate was screwed tight by a Teflon holder between which flexible Teflon o-ring was placed to ensure a good seal.

Pt deposition onto the substrate was carried out in a 0.1 M H$_2$SO$_4$ (93-98 %; SeaStar; Baseline) solution containing 1 mM of H$_2$PtCl$_6$ (Aldrich) prepared with Millipore water (22 $^{\circ}$C). Solution was deaerated with Ar (Praxair) before deposition. The potentiostat used was USB-interfaced μAutolab (Metrohm, Switzerland). Nucleation potential of 0.0 V was applied for 10 millisecond followed by a growth potential of 0.16 V for 10 sec.

6.2.3.2. PtZn particle preparation

PtZn particles were prepared by depositing Zn onto Pt particles previously prepared, followed by a heat treatment. A thin film of Zn was first deposited onto the Pt-dispersed GC substrate by potential cycling, and then bulk Zn was deposited on top by applying the potential of -0.81 V for 10 minutes. This created a thick layer of Zn covering the whole surface of the substrate. The substrate was placed in a 120 $^{\circ}$C preheated furnace for an hour to form a PtZn alloy. After the substrate was cooled to room temperature, unreacted Zn was dissolved in diluted

sulfuric acid. As-prepared PtZn particles were analyzed by AES giving surface compositional analysis. Also, the particles were dissolved into aqua regia (1:3 HNO$_3$:HCl), the diluted to 100.00 mL, and the solution was analyzed in ICP-MS for bulk compositional analysis.
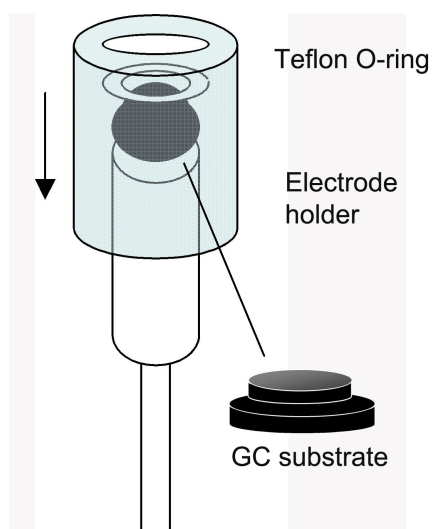
Figure 6-1 Home-made working electrode used for a PtZn nanoparticle stability test. A sheet of glassy carbon was machined in a top hat shape with a surface area of 1.23 cm^2. The substrate was then accommodated into an electrode holder where the bottom face of the substrate is held tight to an aluminum plate. Teflon o-ring is placed in between the substrate and the electrode holder to ensure a tight seal.

6.2.3.3. PtZn stability test

6.2.3.3.1. Polarization of PtZn particles

PtZn particles thus prepared were polarized at potentials of 0.75, 1.0, 0.8, or 1.25 V for various amount of time in an oxygen saturated 0.1 M H_2SO_4 solution at 22 ^{o}C. The polarization time was up to 14, 20, 40, and 2.5 hours, respectively. After the polarization, the electrode was immediately taken out, rinsed with Millipore water, dried with argon, and placed into a UHV chamber for AES analysis.

6.2.3.3.2. Auger electron spectroscopy

Auger electron spectroscopy (AES) instrumentation and operating conditions are outlined in **Chapter 4**. Point analysis was performed on PtZn particles. Spectra were recorded at kinetic energy ranges of 700-1200 eV for Zn and 1800-2100 eV for Pt.

6.2.3.3.3. Inductively coupled plasma – mass spectroscopy measurement

PtZn particles (as prepared and treated with potential) were dissolved in aqua regia (HNO_3 + HCl; Fisher Scientific) and the solution was analyzed by inductively coupled plasma-mass spectroscopy (ICP-MS; ELAN 6000) in order to determine the bulk composition of the metal remaining on the GC. The instrument was calibrated using a standard solution containing Ba, Be, Ce, Co, In, Li, Mg, Pb, Rh, Tl, U, and Y. After polarization, the particles were also dissolved in aqua regia to determine the bulk Pt and Zn content from a calibration curve, and Zn loss was calculated.

6.3. Results and discussion:

6.3.1. Preliminary test 1 – Determination of Zn loss by gravimetry

PtZn foils were created by deposition of bulk Zn onto a Pt foil, followed by stripping of unreacted Zn. According to deposition /stripping current transient curves, the amount of Zn that alloyed to Pt after a spontaneous alloying process (*i.e.,* leaving the sample under Ar atmosphere) was only ~4 % of the amount initially deposited. Therefore it required prolonged deposition numerous times to detect weight changes before and after alloying. Heat treatment was therefore introduced to encourage a sufficient amount of Zn to diffuse into the foil. This method appeared to drive bulk amount of Zn into the Pt foil very rapidly without letting most of the Zn to form bonds with the Pt atoms, possibly because the temperature was too high. When the foil was polarized at non-oxidative potential *(i.e.,* at 0.5 V) or at oxidative potential (*i.e.,* 1.0 V), we observed a significant amount of Zn loss at both potentials by the same extent. Pre-polarization leaching was therefore necessary, and this was done by applying the potential of 0.5 V to the PtZn foils in 0.1 M H_2SO_4 until no further weight loss was observed. This process took about 36 hours. The foils were then polarized at 0.5, 0.75, or 1.0V up to 24 hours in an oxygen saturated acidic solution. The percent loss of Zn (the total amount of weight lost compared to the initial amount of Zn deposited) after the polarization tests are shown in **Table 6-1**. Polarization at 1.0 V showed the most Zn loss from the PtZn foil, although the other foils also showed similar loss within 7 %, and overall the amount of Zn (presumably) leached out was not as significant as compared to those reported in literature [69]. However, it is not clear whether this Zn loss simply came from the residual un-alloyed Zn in the bulk. Due to time constraints, the experiment was performed only once, and a better experimental design was necessary. Therefore further reproducibility for this experiment was not tested.

Table 6-1 Stability of the PtZn alloy at various fixed potential in a 0.1 M H_2SO_4 solution for 24 hours determined by gravimetry.

Polarization potential	PtZn foil	
(V vs. RHE)	Weight lost ($\mu g/cm^2$)	% loss of Zn (wt/wt)*
0.5	3	3
0.75	7	4
1.0	5	7

6.3.2. Preliminary test 2 – Determination of Zn loss by anodic stripping voltammetry

PtZn alloy formation was performed as outlined in the experimental section. The foils prepared were polarized at 0.75, 1.0, and 1.3 V in a 0.1 M H_2SO_4 solution for 12 hours at 22 ^{o}C. After the polarization, the foils remained in the same solution for another 12 hours under the ambient conditions. The initial amount of Zn deposited onto the Pt foil was predicted according to the previous preliminary test 1 showing that only 4% of Zn deposited on Pt remains as an alloy. The resultant solution was analyzed using the ASV technique with standard addition and internal standard methods. No significant loss was observed with 0.75 and 1.0 V polarized samples (only 1~3 % loss), whereas 1.2V one showed 78.1 ± 10.0 % loss of Zn leached out of the foil. Although the error associated with these measurements were high, the result was consistent with Despic's work [106]. However, the measurements were not always consistent, possibly due to contamination of solutions. Therefore we proposed the next stability test which involves dispersion of PtZn particles on glassy carbon substrates.

6.3.3. Pt particle deposition

Pt was electrochemically deposited onto a GC substrate as outlined in Experimental section. A deposition current transient curve is shown in **Figure 6-2** and an SEM image of the surface of the GC substrate is shown in **Figure 6-3**. The typical particle size was 50 ~ 100 nm with a round shape. AES was recorded on those particles, and they showed the Auger transition lines at kinetic energies of 1700, 1780, 1960, and 2400 eV, in agreement with the results in **Chapter 4**. During recording, however, it was noted that the beam current measured on the particles was approximately five times less than the current measured on the GC substrate, indicating the poor adhesion of Pt particles or small contact areas between the particles and the GC substrate.
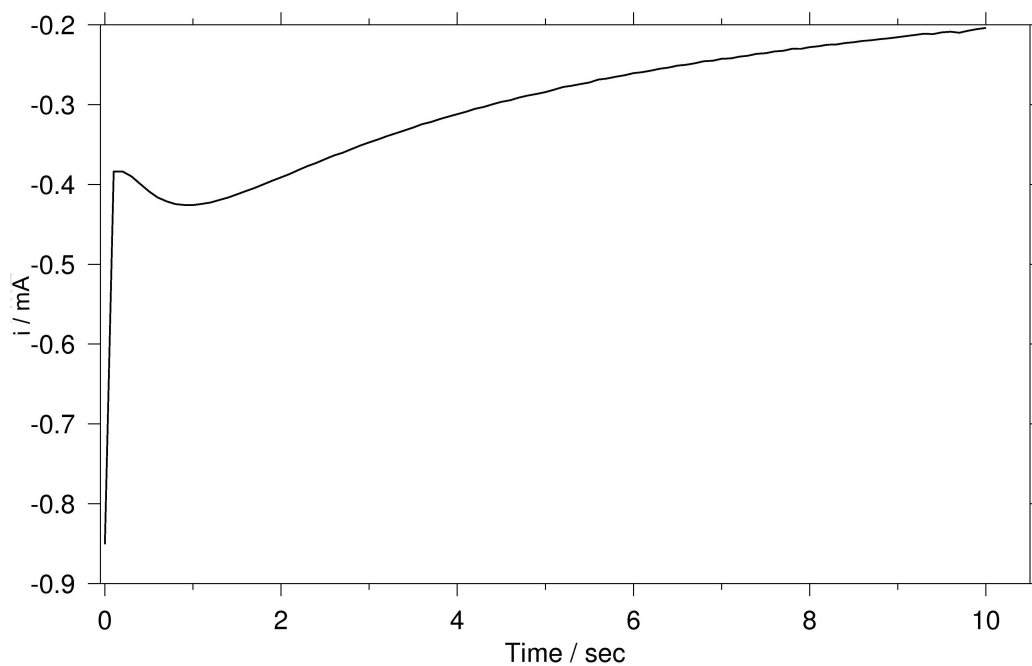
Figure 6-2 Current transient curve showing the deposition of Pt particles onto a glassy carbon substrate. The working solution was deaerated 0.1 M H_2SO_4 containing 1 mM H_2PtCl_6. Nucleation of Pt particle was performed by applying the nucleation potential of 0.0 V for 10 seconds, followed by applying the growth potential of 0.16 V for 10 seconds.
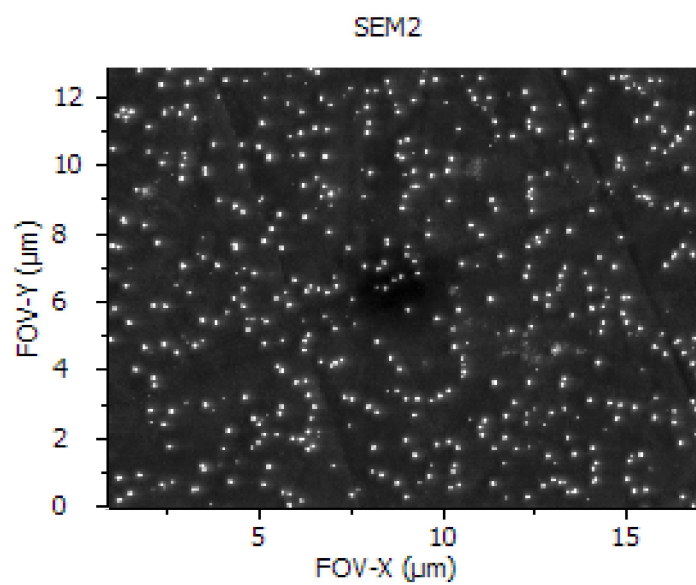
Figure 6-3 SEM image of Pt particles dispersed on a glassy carbon substrate. The particles are spherical with diameters typically 50 ~ 100 nm.

6.3.3.1. Zn deposition on the Pt particles

Once Pt particles were formed on the GC substrate, Zn was also electrodeposited onto the substrate. The deposition potential was determined similar to the one introduced in **Chapter 4**; *i.e.,* ~50 mV more negative than the reversible potential. However, before the bulk Zn deposition, it was necessary to form a thin coating of Zn over the GC substrate because the bulk Zn deposition requires a large negative potential causing extensive hydrogen evolution on Pt particles. As a result, Zn would not be deposited uniformly. The thin coating of Zn was formed by 20 potential sweep cycles between -0.8 V and -0.63 V at 50 mV/s, where Zn is not completely oxidized from the GC surface, as shown in a dotted line in **Figure 6-4**. Once the thin film was formed, bulk Zn was deposited by applying a constant potential.

However, when the alloy formation was attempted under an Ar atmosphere, we were not able to detect any Zn in AES. This was probably because of the poor adhesion of Pt onto the GC substrate. Although the alloy formation occurs very quickly, it requires a reductive potential applied to Pt and Zn atoms. Because of the poor electrical contact between the Pt and carbon, sufficient current did not flow to form the alloy. In fact, when the deposition time was increased to 1 hour, alloyed Zn was detected in AES. However, this is time consuming and also presents a high risk of contaminating the surface. Therefore, the PtZn preparation procedure was modified. Zn was electrodeposited, and then a heat treatment at 120 $^{\circ}$C was applied for 1 hour. This temperature is below the boiling point of surface Zn, which is ~460 K [144] and also, as shown previously, heating at 300 $^{\circ}$C may send bulk Zn deep into the Pt particles without forming Pt-Zn bonds. After the heat treatment, Zn was successfully alloyed to Pt. In **Chapter 4**, we deposited Zn onto a Pt-dispersed GDE. We described that the PtZn was spontaneously formed after the Zn deposition was performed on bulk Pt; however, considering that Zn did not spontaneously alloy with Pt particles of size 50~100 nm, it is reasonable to assume the Pt nanoparticles in the GDE also did not naturally form alloys after the Zn deposition. Rather, they formed alloys when the GDE was hot-pressed to the MEA, which requires elevated temperature and pressure.
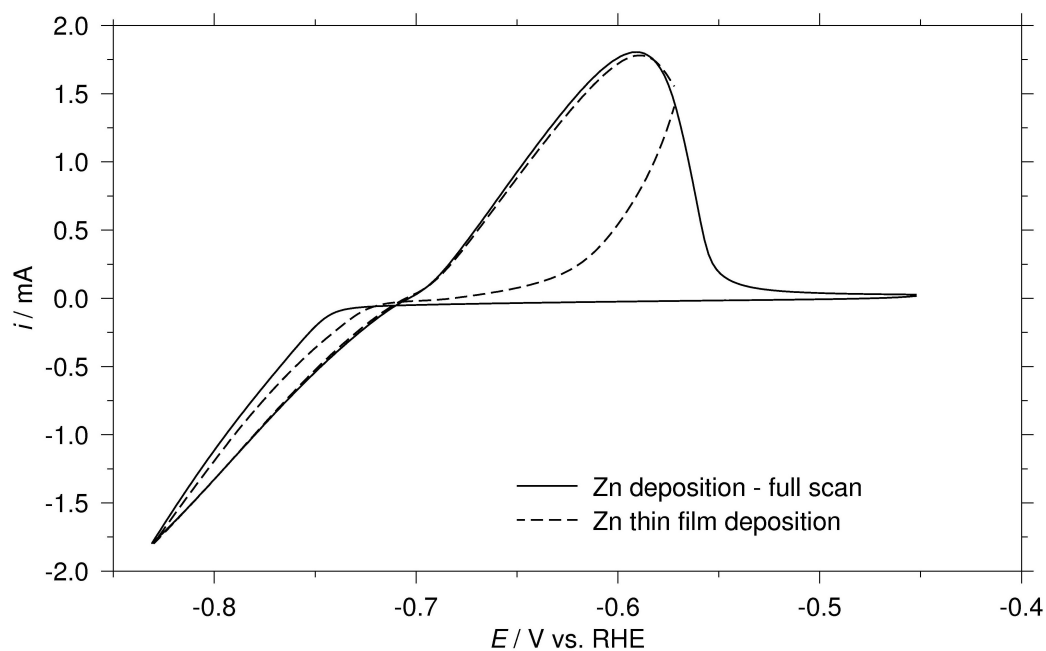
Figure 6-4 Zn thin film deposition over the Pt dispersed glassy carbon substrate was performed by sweeping the potential between -0.8 V and -0.63 V 20 times in a deaerated 0.1 M zinc sulfate solution at the sweep rate of 50 mV/s (shown in a dotted line). The CV in a solid line shows a complete oxidation of deposited Zn, whereas partial oxidation of deposited Zn leaves a thin film of Zn over the glassy carbon substrate. This will be useful when a bulk Zn deposition is applied in the following experimental step as hydrogen evolution from Pt particles are suppressed.

147

6.3.3.2. Zn-modified Pt particles

Figure 6-5 shows the AES of Zn and Pt recorded from a single particle. Only the Zn and Pt kinetic energy ranges were selectively scanned because the scale of a spectrum in general is set according to the highest peak of the recorded spectrum. If a survey scan is recorded for the entire or even a small part of the substrate, the spectrum is adjusted to the large carbon peak, scaling both Pt and Zn down. Integrating the Zn LM_2 (at 990 eV) and Pt MN_3 (at 1960 eV) peaks, the average composition of Zn and Pt were determined to be 4.2, and 95.8 ± 1.6 atomic %, respectively. It was noted in **Chapter 4** that peak heights of Pt MN_3 and MN_2 (at 2040 eV) were almost 1:1 for most of particles, suggesting chemical interaction between Pt and Zn.

The particles on the GC substrate were dissolved in aqua regia, and the solution was analyzed for Pt and Zn by ICP-MS. This was to confirm the bulk PtZn composition. The maximum Zn content in the alloy particles was determined to be approximately 40 atomic %, assuming all Pt reacted with Zn. This is consistent with the data obtained in **Chapter 4**; the composition of the bulk alloy was determined to be 42 atomic % Zn.
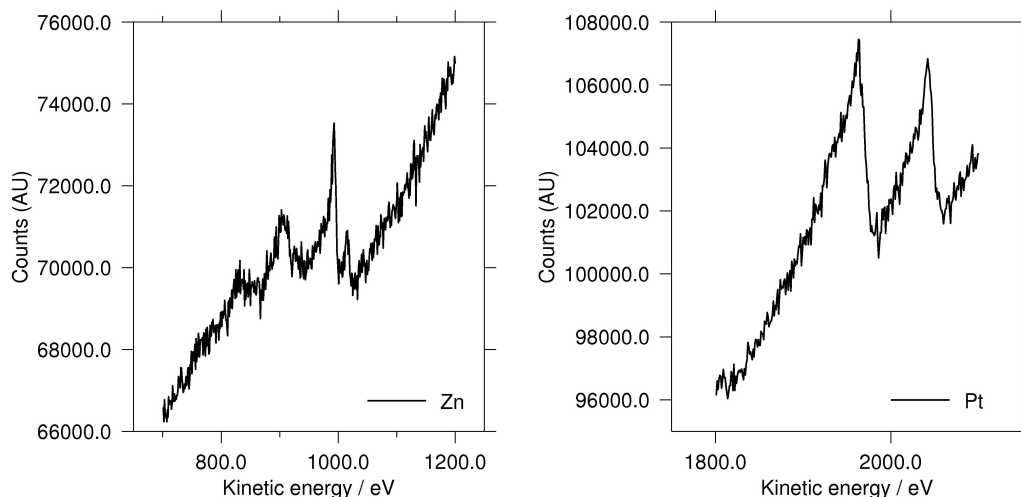
Figure 6-5 Auger electron spectra of Zn (left) and Pt (right) recorded from a single Zn-modified Pt particle after the heat treatment. The average % amount of Zn on the surface on as-prepared particles was 4.2 %.

6.3.3.3. Polarization of PtZn particles

The Pt and PtZn particles on GC substrates were then polarized at potentials of 0.75, 0.8, 1.0, and 1.25 V for various durations to test stability. These potential values were chosen for the following reasons: (1) Potential of 0.75 V is where both Pt and PtZn do not participate in any reaction, according to the Ar saturated CVs, and therefore the metals are expected to be stable at this potential. (2) Potential of 1.0 V (or 0.8 V) is where oxidation of Pt or PtZn starts to occur and we could not predict if the metals were stable. (3) Potential of 1.25 V is where PtZn is known to oxidize, and therefore we would be able to monitor the Zn dissolution behavior. The substrates were then rinsed with water, dried with Ar, and immediately transferred into the UHV

chamber for AES analysis. SEM images showed that after any polarization process, the particles became larger by the factor of 3 to 5 than those on unpolarized substrates due to the sintering process. Sintering is the agglomeration of Pt particles during the fuel cell operation, decreasing the active catalytic surface area. Sintering mainly occurs either by dissolution/ re-precipitation of particles or by the surface diffusion [160, 161]. The particles tend to agglomerate during the polarization, making them larger. Also, some of the larger particles appeared to be spherical. AES on such particles showed a trace amount of Zn, but with the surface mainly Pt, possibly because Zn diffused into the bulk. Also, one of the difficulties in AES analysis was to obtain a number of scans from a single particle because when illuminated by the electron beam, the particles moved due to the poor particle-substrate adhesion. However, there also were particles that had irregular shapes and also appeared to adhere very well to the substrate, as shown in **Figure 6-6**. These particles were not affected by sintering and seemed to be a good representative of PtZn particles. For these reasons, the Zn concentrations were measured on such irregular shaped particles. Such strong adhesion of a Pt-alloy onto a carbon substrate (known as the anchoring effect) has also been reported for the PtFe [162] and for the PtNi nanoparticles [163] Although the reasoning behind the effect was not clarified by these reports, they both observed the suppression in particle sintering and strong adhesion to carbon with these Pt alloys. The PtZn alloy we prepared on the GC substrate shows the same phenomenon. This anchoring effect is certainly beneficial in a fuel cell application since the sintering decreases the active surface area for catalysis and results in an uneven distribution of catalyst particles in an MEA [131].

Figure 6-7 shows the surface Zn concentration (in atomic %) with respect to the duration of polarization measured at the applied potential. The first hour of polarization at 1.0 V increased the Zn surface concentration to 6.5 atomic %, and it further increased to 19.3 atomic % after 20 hours of polarization. We did not observe a decrease in the surface concentration, meaning either the particles are stable, or some Zn may have leached out, yet the particles may contain sufficient Zn to maintain an equilibrium surface concentration. It was also noted no oxygen was detected in AES, indicating no metallic Zn was left on the surface.

The polarization potential of 0.75 V is, according to the Ar saturated CV, the region where no obvious redox reaction occurs in the absence of oxygen, and therefore we predicted PtZn is probably stable at this potential. In fact the open circuit potential of the electrode was

0.95 V; much more oxidative than the applied potential. After 1 hour of polarization, the concentration of Zn did not seem to change from unpolarized sample (4 atomic %), but after 5 hours, the concentration increased to 7.13 atomic %. Further polarization did not seem to dramatically change the surface concentration; 7.76 atomic % after 12 hours. This indicates the equilibrium surface composition at the applied potential of 0.75 V is approximately 8 atomic % Zn. No further polarization was applied as PtZn is considered stable at this potential.

Polarization at 1.25 V provided quite different results. Only 30 minutes of polarization made the surface concentration of Zn 3.22 atomic %; less than the unconditioned one (4.2 atomic %). After 2.5 hours of polarization, AES detected Zn just above the detection limit of the instrument, which is 0.2 atomic %. It is clear from this plot that at 1.25 V, PtZn is unstable and Zn is completely leached out of the alloy.
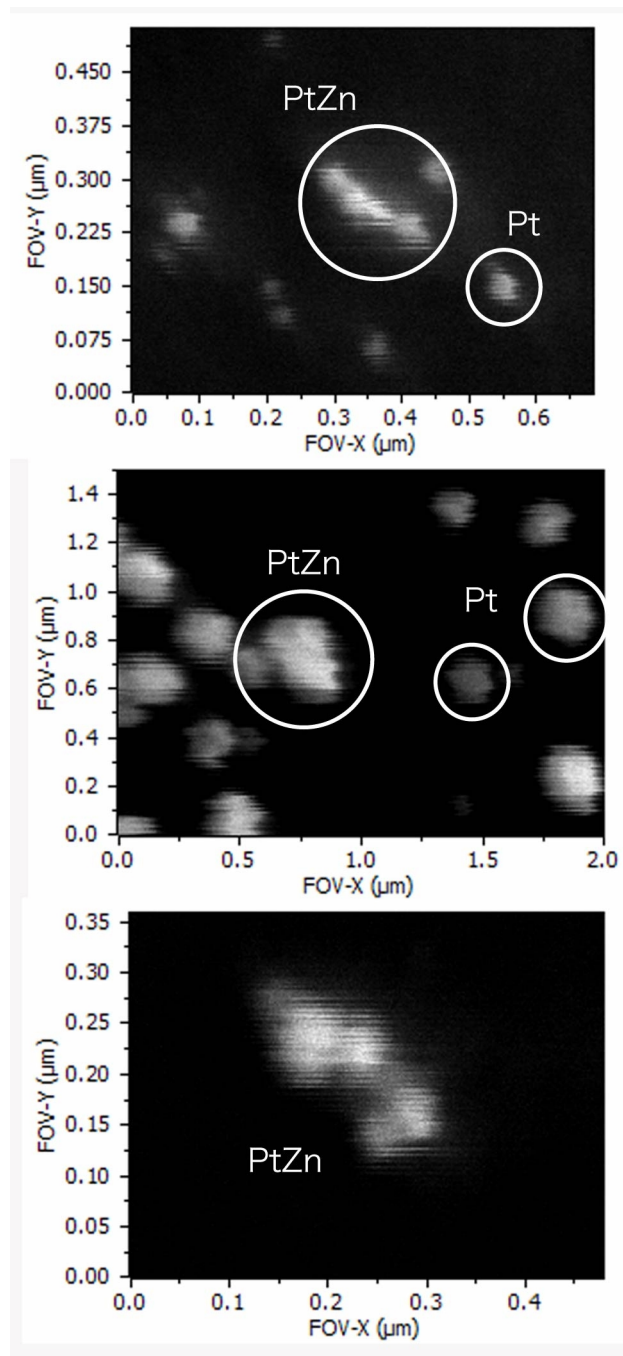
Figure 6-6 SEM image of PtZn particles on the glassy carbon substrate. Unlike Pt particles that appeared round and showed poor adhesion, PtZn particles appeared in irregular shapes and adhered to the substrate well. Generally, Pt particles grew in size as longer polarization was applied due to sintering, but this was not an issue with PtZn particles.
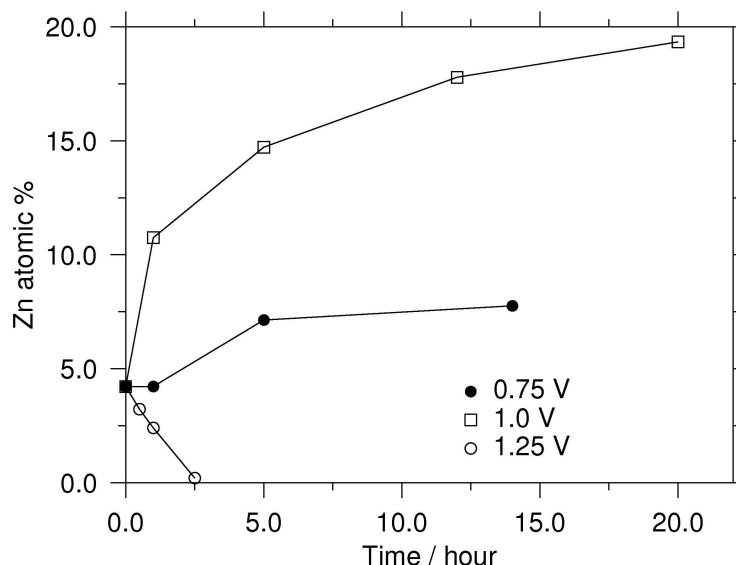
Figure 6-7 The change in surface concentration of Zn with respect to duration of polarization at the potential of 0.75 V (filled circle), 1.0 V (square), or 1.25 V (empty circle). Polarization was performed in an oxygen saturated 0.1 M sulfuric acid solution at 22 °C. Zn concentration on the surface increases as the duration increased for the samples polarized at 0.75 and 1.0 V. They even reached a plateau, but it never decreased during the polarization period, indicating the surface became Zn-saturated with or without having more Zn leached out into the solution. On the other hand, the samples polarized at 1.25 V showed a rapid decrease in the surface Zn concentration indicating PtZn is unstable at this potential and Zn immediately leaches out from the bulk into the solution.

PtZn particles polarized at 1.0 V for 12 h and 20 hours were further analyzed by ICP-MS after the AES analysis. The results are tabulated in **Table 6-2**. The particles were dissolved in aqua regia, and the solutions were analyzed. After 12 h polarization, the sample did not show a drastic difference compared to the unpolarized sample; only 0.77 ± 0.09 % loss. The measurements after 20 h of polarization were duplicated, and the average Zn:Pt after the polarization was determined to be 0.59:1. Polarization of PtZn for 30 h at 1.0 V was also attempted, but this treatment oxidized and damaged the surface of GC so that it delaminated

from the surface. Therefore, we performed the polarization tests for 30 h and 40 h at 0.8 V and then dissolved the remaining particles in aqua regia, and analyzed the solution by ICP-MS. Auger analysis on these samples were not recorded due to technical constraints. After 30 h, the amount of Zn lost was 16.1 ± 1.9 %, and after 40 hours, 18.8 ± 2.3 %. It should be noted that only one sample (except for 1.0 V, 20 h polarization samples) was available from each polarization condition. Reproducibility of these measurements needs to be assessed in the future. Although we observed approximately 20% loss of Zn after 40 hour polarization at 0.8 V, the composition of PtZn was about 1:0.53 (almost 3:1); still retaining a high Zn content. The Pt-Zn phase diagram (**Figure 2-15)** shows Pt_3Zn, as well as Pt_1Zn_1, is stable as a bulk intermetallic compound. Colon-Mercado and Popov studied the stability of 20 wt% PtCo and PtNi MEAs in a similar manner to ours (alloy compositions of 1:1 and 3:1 for both alloys). The authors reported 40 % and 30 % of the transition metal dissolution from Pt_1Co_1 and Pt_1Ni_1, respectively, after only a few hours of polarization. Stabilities of Pt_3Co_1 and Pt_3Ni_1 were, on the other hand, much more improved; less than 10 % metal dissolution over 60 hours of polarization [163]. Considering Zn loss between 30 and 40 hours was only about 2 %, Pt_3Zn may be significantly more stable than other Pt alloys. In the literature, Pt_3M_1 alloys (where M is to a transition metal) show a better stability; less than 10% transition metal dissolution over 80 hours of polarization, whereas Pt_1M_1 alloys showed almost 40% dissolution within an hour of polarization in an acid solution [69].

Table 6-2 Relative Zn loss from an initial concentration on the nanoparticles calculated from ICP-MS measurements (Zn:Pt was 0.65_3:1 before polarization)

Polarization potential (V)	Duration (hour)	Zn loss (%)	Zn:Pt ratio
1.0	12	0.77 ± 0.09	0.64:1
	20	8.9 ± 1.1	0.59:1
0.8	30	16.1 ± 1.9	0.54:1
	40	18.8 ± 2.3	0.53:1

The apparent PtZn stability relative to other Pt alloys may be explained by considering the Pt-Pt and M-M (where M is a transition metal) bond lengths. Various types of bond lengths in Pt-transition metal alloys and in the PtZn alloy are tabulated in **Table 6-3** [101, 70]. In the table, percent changes in Pt-Pt and M-M bond lengths are also shown (The presented values were not obtained in an equivalent method, but the trends in the changes would be apparent by calculating the percent differences). As described in **Chapter 2**, the Pt-Pt bond distance generally decreases when a Pt-M alloy is formed, which is evident from -Cr, -Co, and -Ni alloys, where the Pt-Pt bond distances decrease by 3 % [70]. In contrast, M-M distances tend to increase after Pt-alloys are formed; 5.2 and 1.6 % changes in -Co and -Ni alloys, respectively. This may suggest that only the transition metals contribute to heteronuclear bonding in Pt-M alloys. The heteronuclear bond distances in these alloys are slightly smaller than their Pt-Pt distances.

In the PtZn alloy, on the other hand, the Pt-Pt distances increased to 2.81 Å in PtZn from 2.77 Å in bulk Pt (+1.44 % change). The Zn-Zn bond lengths changed significantly from the value for bulk Zn (2.66 to 2.85 Å corresponding to + 8.64 % change). Interestingly, the Pt-Zn bond length was much shorter (2.65 Å) than the homonuclear bond lengths, reflecting the increase in electron density in the bimetallic bond which makes the Pt-Zn bond strong. In fact, the Pd-Zn and Pt-Zn surfaces displayed the largest changes in the CO desorption temperature

155

and were the first and second strongest metal-Zn bimetallic bonds respectively in the DFT study [101]. This suggests that these alloys may be significantly stable, which is important for a fuel cell catalyst. The changes observed for CO adsorption on the Pt/Zn alloy surface, as compared to Pt, is similar to that reported for Pt alloyed with the early transition metals [112].

Table 6-3 Pt-Pt and M-M bond lengths (M denotes the transition metal) in the pure forms or in the Pt alloys; percent change in bond lengths before and after alloying. The values for Pt, PtCr, PtCo, and PtNi were taken from [70], whereas the ones for PtZn were taken from [101]. PtCr, PtCo, and PtNi show approximately 3 % decrease in Pt-Pt bond distance after alloying, although the Pt-Pt bond distance in PtZn increased by 1.4 %. On contrary, M-M bond distances in PtCr, PtNi, and PtZn increased. This may be because only transition metal electrons contribute to the bimetallic bonding. Pt-M bond distance in PtZn is considerably shorter in PtZn than Pt-Pt or Zn-Zn. Pt appears to contribute to the bimetallic bonding in PtZn, which may be important in designing a stable catalyst in fuel cells.

M	Pt-Pt (Å)	Pt-M (Å)	M-M$_{pure}$ (Å)	M-M$_{alloy}$ (Å)	% change (Pt-Pt)	% change (M-M)
Pt	2.77		2.77			
PtCr	2.71	2.69	2.49		-2.16	
PtCo	2.68	2.63	2.50	2.63	-3.25	+5.20
PtNi	2.68	2.61	2.49	2.53	-3.25	+1.61
PtZn	2.81	2.696	2.66	2.89	+1.44	+8.64

Another interesting observation was the AES peak height ratio between Pt MN_3 and MN_2. **Figure 6-8** shows the typical AES Pt signals from the PtZn particles polarized at 1.25 V for 1 hours (a), 1.0 V for 20 hours (b), and 0.75 V for 14.5 hour (c). In **Chapter 4**, we observed that the MN_3 and MN_2 peak heights become similar when Pt interacts with Zn. As shown in the figure, peak heights at polarization at 0.75 V and 1.0 V show almost 1:1 peak heights (the ratio of 1.30 and 1.28, respectively), whereas it is no longer the case for the 1.25 V polarized sample (the ratio of 1.52). This is another indication that polarization at 0.75 V and 1.0 V retains the chemical interaction between Pt and Zn for a prolonged period, in contrast to 1.25 V. The peak ratio for the pure Pt determined in **Chapter 4** was 1.86, therefore the polarized sample at 1.25 V may be retaining a little interaction between Pt and Zn.
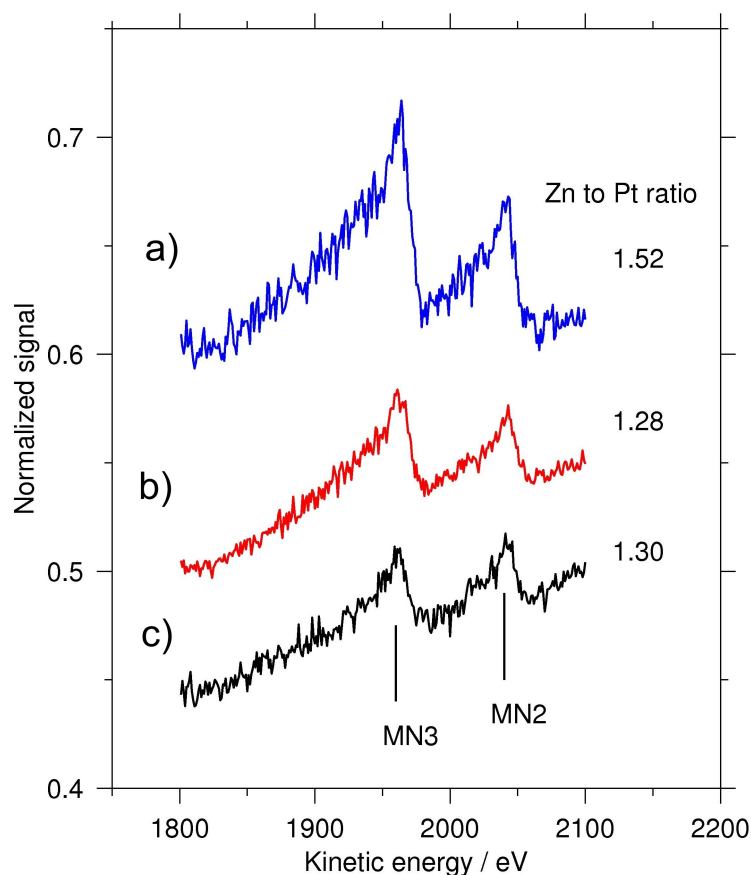
Figure 6-8 Typical Pt Auger spectra from the PtZn particles polarized at a) 1.25 V for 1 hours, b) 1.0 V for 20 hours, and c) 0.75 V for 14.5 hour. The ratios of Pt MN_3 to MN_2 peak heights are shown on the right hand side of the spectra. As shown in **Chapter 4**, 1:1 ratio of those peaks implies the interaction between Pt and Zn. Spectra b) and c) show almost 1:1 peak height ratios whereas the spectrum a) (the sample polarized at 1.25 V) shows an obvious difference in the peak heights. This indicates that the samples polarized at 0.75 and 1.0 V after 14.5 and 20 hours, respectively, still maintain Pt-Zn bimetallic bonds, whereas the sample polarized at 1.25 V for 1 hour does not.

6.4. Summary and conclusions

In this chapter, the chemical stability of PtZn was investigated by forming PtZn particles on GC substrates and applying constant potentials of 0.75, 1.0, 0.8, or 1.25 V for a variety of durations under ambient conditions. $Pt_{60}Zn_{40}$ particles (bulk composition) were successfully formed after a heat treatment. Initially, the surface concentration of Zn was 4.2 atomic %; however, it increased and plateaued at 7.7 % after 14.5 hours of polarization at 0.75 V or at 19 % after 20 hours at 1.0 V. This supports the increase in the Zn surface concentration as described in **Chapter 5**. Samples polarized at 1.25 V showed almost no Zn at the surface concentration after 2.5 hours of polarization, showing the alloy was not stable at this potential.

PtZn particles polarized at 1.0 V for 12 and 20 hours, as well as those polarized at 0.8 V for 30 and 40 hours, were dissolved in aqua regia and the bulk concentrations were determined by ICP-MS. Approximately 9 % of Zn was lost up to 20 hours of polarization at 1.0 V compared to the unpolarized particle. After 30 and 40 hour polarization at 0.8 V, 16 and 19 atomic % of Zn was lost from the original composition. Although more prolonged investigation is necessary for assessing the leaching behavior, $Pt_{60}Zn_{40}$ appears more stable than other 1:1 Pt alloys reported in literature. Moreover, the remaining PtZn after 40 hour polarization showed 3:1 composition, which is also a stable form of the alloy according to the phase diagram. Considering the amount of Zn lost over 30 to 40 hour polarization was by 2 %, it can be predicted Zn dissolution will not be severe after 40 hours. Further investigations are necessary to confirm the even longer term stability.

Stability of the PtZn alloy after 0.75 and 1.0 V polarization was further confirmed by comparing Pt MN_3 and MN_2 peak heights. Particles treated at those polarization potentials retained almost 1:1 peak ratios, whereas the ones polarized at 1.25 V showed a ratio of 3:1, indicating a minimal interaction between Pt and Zn. Although the experimental data need to be confirmed, the results indicate the chemical stability of PtZn may be quite promising for use in fuel cells.

7. Conclusions And Future Work

The fuel cell will be one of the key power sources in the future for its environmentally benign operation, the high energy conversion efficiency, and the wide applicability in electrical devices. It is also a device that encompasses knowledge in numerous branches of science stacked together. The fuel cell is certainly a state of the art device, yet with a large number of challenges. This project involved a number of people assisting us either to support our experimental data or to expand our knowledge with their expertise. That is essential to the fuel cell research as it is such an interdisciplinary field of science with a lot of correlations from one branch to another. This thesis focused on the electrocatalysis of the fuel cell reactions on an electrochemically-prepared PtZn alloy as the catalyst and outlined new findings which create experimental opportunities for future work.

This chapter first summarizes the results presented in **Chapter 4 to 6** followed by suggestions for future work.

7.1. Summary of the thesis

In **Chapter 4** the formation of the PtZn alloy on a bulk Pt substrate was first confirmed by scanning electron microscopy (SEM) and Auger electron spectroscopy (AES). Our PtZn alloy also revealed more facile oxygen uptake than metallic Zn which gave us the impetus to apply this alloy as an ORR catalyst. Improved catalytic activity (by 30 mV) towards the ORR was observed both in an electrochemical cell setup and in a single stack fuel cell. The Tafel slopes measured on smooth Pt and PtZn were both very similar, and the number of electrons exchanged during the ORR on the PtZn surface was 3.97. The work presented in this chapter envisages the prospect of the PtZn in the PEMFC application.

The catalytic activity of the CO oxidation reaction on the PtZn surface was investigated in **Chapter 5**. When compensated for the surface roughness induced by Zn deposition/

modification, our PtZn alloy did not show improved activity for the CO oxidation. However, more facile reaction kinetics for the ORR was still observed after the roughness correction. Also the alloy surface exhibited a structural reorganization after the adsorption of oxygen or CO. This was observed in electrochemical measurements. The oxygen adsorption induced more Zn segregation to the surface, whereas CO adsorption induced Pt to segregate to the surface. The findings in this chapter could be important for reaction mechanism studies. The enhancement in the ORR or the CO oxidation catalysis is currently explained by an electronic structure change induced in Pt atoms or by the decrease in the Pt-Pt bond distance due to alloying, but the observed site exchange process may add another element to the explanation of the ORR mechanism or the CO oxidation reaction.

The PtZn surfaces presented throughout **Chapter 4** and **Chapter 5** are prepared by the Zn electrodeposition followed by spontaneous alloy formation on bulk Pt, but this methodology raises a question – what is the amount of Zn remaining in the Pt or on the surface? Currently we do not have a clear answer to this somewhat obvious question because (1) Zn electrodeposition efficiency is limited by hydrogen evolution, and it is a challenge to quantify the current efficiency; (2) the resultant PtZn surface is heterogeneous as presented in **Chapter 5** and the reproducibility of PtZn surfaces depend on the character of the Pt substrate; and (3) the diffusion of Zn into Pt occurs quickly as presented in **Chapter 4**, therefore the amount of Zn diffusing into Pt during the alloy formation is difficult to estimate. This question may not have been an issue if we made a bulk PtZn alloy by sputtering, but the facility was not available, and it would not meet the original motivation of the project. This is still an open question which requires a further investigation.

Chapter 6 explored different methods to investigate the chemical stability of the PtZn alloys using electrochemistry and AES. All stability studies involved the polarization of the alloy in an oxygen saturated acidic solution at the room temperature. The preliminary studies using gravimetry and anodic stripping voltammetry showed that the alloy was stable under the fuel cell operating conditions. To further study the stability of the PtZn alloy, we created PtZn particles on glassy carbon (GC) substrates and then performed the polarization study. Because Zn does not form an alloy with carbon, Zn remaining on the GC substrates must be in the form of the Pt-alloy. During the polarization process, Zn was expected to migrate to the surface of the alloy, based on the results presented in **Chapter 5**. The surface Zn concentration measured by

AES showed an increase initially, but eventually reached a plateau at the polarization potentials of 0.75 and 1.0 V (the surface concentrations of 6.5 and 19.3 atomic % Zn, respectively), whereas the surface concentration constantly decreased for the polarization potential at 1.25 V, showing the instability of the alloy. The polarized samples at 0.75 and 1.0 V may still suffer from Zn dissolution from the alloy, as the bulk concentrations of the PtZn particles constantly decreased during a prolonged polarization was applied (8.9 % of Zn was lost over 20 hours of polarization at 1.0 V); however, the amount of Zn leached out from the alloy is quite small relative to other transition metals, such as PtCo or PtNi, dissolving from their Pt-alloys. The work presented in this chapter is still incomplete and more data relating the surface and bulk Zn concentrations within the alloy particles needs to be obtained to fully describe the stability of the PtZn alloy. However, our data so far suggests reasonable stability of the PtZn alloy under a rather severe fuel cell condition over the duration of the stability studies.

Another very interesting finding from the work shown in **Chapter 6** was that PtZn particles adhere to the carbon substrate more strongly than Pt. Pt-rich particles, especially after the prolonged polarization process, exhibited sintering (*i.e.,* coagulation of smaller particles), but this was not the case for the PtZn particles. This is very important for the fuel cell application because sintering decreases surface area-to-volume ratio of the Pt particles on the catalyst layer which subsequently leads to the uneven distribution of Pt particles in an MEA and subsequent decrease in current density. If we could successfully prepare a catalyst layer with the catalysts well-adhered to the support, it would be very beneficial for fuel cell durability.

The experimental results presented in this work lead to four main findings: 1) The PtZn alloy improves the ORR kinetics compared to Pt; 2) the adsorption of oxygen or CO molecules induced surface restructuring on the alloy surface – the adsorption of oxygen makes the alloy surface enriched with Zn, whereas the adsorption of CO makes the surface enriched with Pt; and 3) the stability of PtZn; and 4) the PtZn alloy may be free from sintering process as it adheres well to carbon. Since there still are numerous uncertainties regarding fuel cell reactions, such new findings may significantly aid understanding the fundamental questions, thus developing the fuel cell technology. Also, the finding (2) is an interesting one for surface analysis in general, as the adsorbate-induced segregation of one component of an alloy has been observed with

various systems, but not with a PtZn alloy, to our best knowledge.

Although these findings are unique, there are several experiments need to be performed to further clarify the fuel cell reaction process on the PtZn surface. Suggested experiments are outlined next.

7.2. Future work

7.2.1. Hydrogen peroxide production on the PtZn surface and the reaction mechanisms

The first experiment one could perform is the measurement of hydrogen peroxide (H_2O_2) production during ORR on the PtZn alloy. The presence of H_2O_2 is, as mentioned in **Chapter 2**, unfavorable as the oxygen molecule reduction to H_2O_2 only involves two electrons and damages the solid electrolyte in the MEA. The number of electrons transferred calculated in Chapter 4 was 3.97, but this still does not eliminate the possible H_2O_2 production at a lower potential. There are a number of literature reports showing the H_2O_2 production both on a pure Pt surface and the Pt-based alloy surfaces, confirmed by rotating ring disk electrodes (RRDEs) [164, 29, 27, 26]. An RRDE is similarly constructed to an RDE, except there is a ring electrode (usually Pt) around the disk electrode, separated by an insulating material. As the electrode rotates, the reactants in the solution are forced to come to the disk surface, the redox reaction occurs, and the reaction products depart from the surface. If an appropriate potential is applied to the ring, the products could either be reduced or oxidized at the ring, resulting in a current flow.

The investigation of H_2O_2 formation on our PtZn surface can also be done using an RRDE; or alternatively, it could also be performed by placing a microelectrode (the electrode with a small but well defined area) in the vicinity of the RDE. The microelectrode essentially acts as the ring on the RRDE. The Bizzotto laboratory at University of British Columbia has

also been developing the method to fabricate the in-house microelectrode using a pipet puller and a coax cable [165]. The challenge with this method is the collection of H_2O_2 by the microelectrode surface, but could be an alternative way to investigate not only H_2O_2 but products in any reactions and spatial distribution of the production.

An alternative method to the RRDE is scanning electrochemical microscopy (SECM) [166, 167]. This technique uses a microelectrode to probe the surface of interest, in this case it would be the PtZn alloy. There are different modes of operations, but the one employed in determining H_2O_2 generation is called the substrate generation/tip collection (SG/TC). This is shown in **Figure 7-1** [168] The microelectrode is connected to piezo-controller to allow rastering of the electrode just above the substrate at a constant height in a controlled manner. The microelectrode is held at the H_2O_2 oxidation potential while that of the substrate is changed. Once H_2O_2 is produced at the substrate, the microelectrode oxidizes the H_2O_2 and the current is recorded.

The operating principle is equivalent to the RRDE method, but SECM is more versatile [169]. For example, it can also be used to study the ORR mechanism. Assume the substrate is immersed into an oxygen saturated electrolyte, and the tip (microelectrode) is placed above the substrate [170, 171]. When the tip is far enough from the substrate so that all oxygen hemispherically diffuses onto the tip (*i.e.*, nothing hinders the oxygen molecules to diffuse onto the surface), the current measured at the tip, $i_{T,\infty}$, is constant and determined by the equation below:

$$i_{T,\infty} = 4nFD_oC_o^*a \tag{7-1}$$

In this equation, n is a number of electrons transferred, F is Faraday Constant, D_o is the diffusion coefficient of oxygen, C_o^* is the bulk concentration of oxygen, and a is the radius of the microelectrode. When the tip is brought closer to the substrate, the current measured at the tip, i_T, will decrease because the oxygen diffusion is now hindered. The tip is then approached to the substrate so that measured $i_{T,\infty}$ is, *e.g.*, 90% of $i_{T,\infty}$. Keeping the same distance between the tip and the substrate, the microelectrode is then moved across the substrate so the measured

current is constant (*i.e.*, 90% $i_{T,\infty}$). During this measurement, the substrate potential is maintained in the kinetic region for ORR. The tip is scanned across the sample. The measured current will be constant (*i.e.*, at 90% $i_{T,\infty}$) above an inactive region. However, when the tip is brought above the active site, some oxygen is consumed at the site, so the microelectrode senses a lower concentration of oxygen, resulting in decrease in measured current at the microelectrode. Therefore, by knowing the position of the tip and by monitoring the tip current, the location of active sites can be approximated. Once the position of the active sites are known, *in-situ* spectroscopic analysis, such as Raman spectroscopy, can be employed to determine the chemical properties of the active site during ORR.
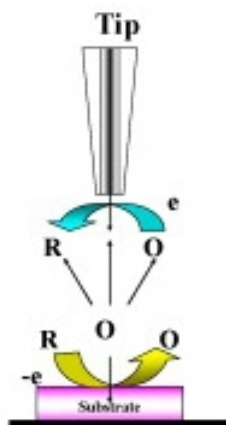
Figure 7-1 Substrate generation/ tip collection mode in SECM. The microelectrode is connected to piezo-controller to allow rastering of the electrode just above the substrate at a constant height in a controlled manner. The microelectrode is held at the appropriate oxidation potential while that of the substrate is changed. Once oxidizable products are produced at the substrate, they are detected at the microelectrode, generating the oxidative current. Reprinted from [168]. Copyright 2007 with permission from Elsevier Ltd.

7.2.2. Density functional theory calculations

Previously reported density functional theory (DFT) calculations on small clusters for PtZn were published by Rodriguez *et al.,* [112, 143, 119]] and Chen *et al.* [101]. These authors came to similar conclusions: When Pt and Zn were alloyed, both the Pt-Pt and Zn-Zn bond distances increased relative to the lengths in their pure forms, but the Pt-Zn bond distance was shorter than either of bond lengths. Also the Pt 5*d* orbital population decreased after the alloying. In addition, Rodriguez used ab initio calculations and showed Pt acts as an electron acceptor, whereas Zn acts as an electron donor [112].

Currently DFT calculations on the Zn modified Pt surface and the interaction of oxygen with the resultant surface have been investigated in collaboration with Dr. Eben Dy in Department of Chemical Engineering at University of British Columbia. Dr Dy was able to reproduce the results obtained by Rodriguez and Chen listed above using the DFT method. He was also able to calculate the distance of an oxygen molecule approaching to the Pt(111) surface in "end-on" or "Pauling arrangement" (see **Figure 2-10** in **Chapter 2**.), and his data agreed well with the previously reported experimental result [172].

Theoretical calculations for fuel cell reactions on Pt-based alloys have extensively been carried out, especially by Nørskov and coworkers, *e.g.,* [173, 35, 174]. For example, they have successfully reproduced the volcano plot. They also used density functional theory (DFT) calculations to model the oxygen reduction reaction pathway on Pt and calculated the energies of intermediates as a function of applied potentials. Based on the calculated energies, they developed a kinetic model that allowed them to predict the reaction rate at a given potential [35]. This is certainly useful for the determination of the rate determining step for ORR. DFT methods are powerful for simulating complex systems and for confirming if the theories and experimental data agree each other.

DFT can also be useful in understanding the PtZn system, such as the surface energy of the alloy with or without adsorbates. When oxygen molecules are adsorbed onto the PtZn surface, Zn migrates to the surface, and this appears to enhance the ORR kinetics. The driving force is assumed to be a thermochemical effect, but the electronic state of Zn in the alloy is obviously different from its pure form. The DFT calculations would help determining the

segregation energy of Zn from which the characteristics of the alloy surface could be better understood.

7.2.3. Alternative PtZn alloy formation – A bulk alloy or alloy particles

Our method of the PtZn preparation is simple and cost-effective for catalyst layer mass production; it requires an electrochemical Zn deposition onto Pt, and the alloying would subsequently occur at ambient conditions. However, the formation of surface alloys introduces severe surface roughening. This is unfavorable if one needs to conduct the kinetic studies because defects on the surface play an important role in the kinetics, as introduced in **Chapter 2** and **5**. In **Chapter 5**, we prepared an equivalently "rough" Pt surface to the alloy surface by Pt deposition, but this does not mean we have perfectly equivalent surfaces. Preparation of bulk PtZn followed by polishing would provide a better comparison to the equivalently polished Pt surface.

There are several preparation methods introduced in the literature, such as arc melting, chemical vapor deposition of Pt onto a zinc oxide substrate or a sputtering method, followed by the heat treatment, [119, 175, 5, 176]. The method introduced by Huang and coworkers uses $ZnCl_2$-1-ethyl-3-methelimidazolium chloride (EMIC) ionic neat solution containing Pt (II) to electrochemically codeposit both Pt and Zn onto a tungsten substrate. Ionic liquids are aprotic, thereby hydrogen evolution from the Pt surface is not an issue [177]. Also, the composition of the alloy can be controlled by tuning the deposition potential. The PtZn alloy formation was confirmed after applying a fixed reductive potential for as short as 20 seconds.

Also observed by Huang and coworkers was the formation of particles on the PtZn deposited film. The SEM images recorded by the authors in the $ZnCl_2$ -EMIC is shown in **Figure 7-2**. The middle image shows the appearance of irregular shaped flakes which are presumably PtZn alloys [177]. Once any unalloyed Zn is eliminated from the deposit (as the authors claimed these films are ~90 atomic % Zn prepared at the conditions they applied), these particles may anchor well to the carbon support in the catalyst layer in an MEA, just as we observed in **Chapter 6**, but without the bulk Pt particles which will, if present in the MEA,

aggregate during the course of the fuel cell operation.
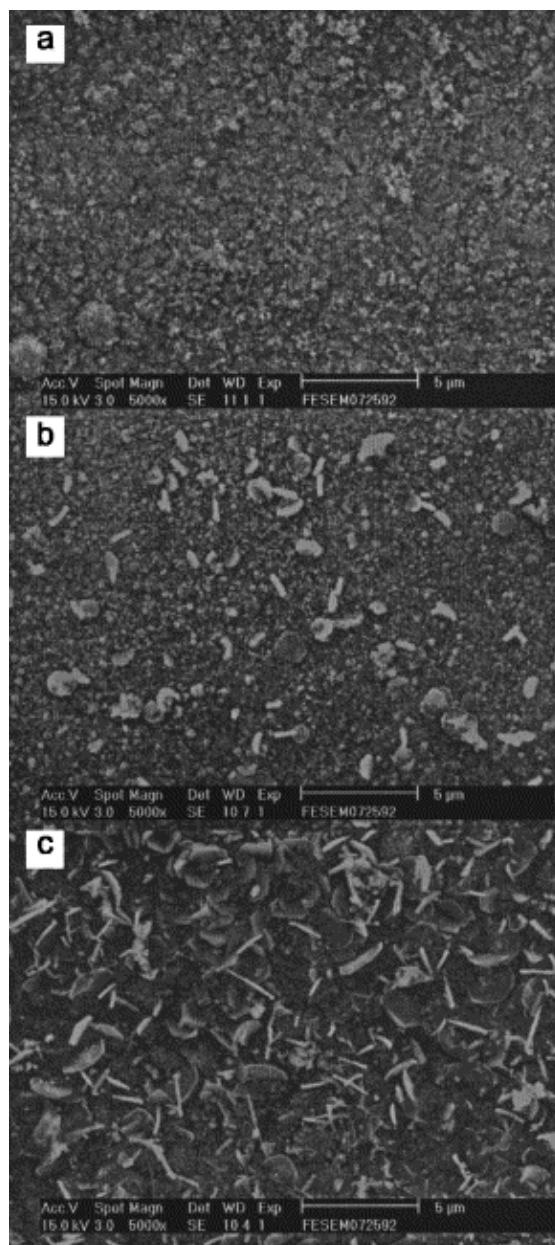
Figure 7-2 SEM images of the PtZn alloy deposited on a tungsten substrate from the ZnCl$_2$-EMIC ionic solution at a) E=-0.2 V vs. Zn (Pt atomic % = 15.69) ; b) E=-0.22 V vs. Zn (Pt atomic % = 7.71); and c) E=-0.25 V vs. Zn (Pt atomic % = 5.67). The SEM image b) shows irregular-shaped particles, similar to the PtZn particles on glassy carbon reported in **Chapter 6**. Reprinted from [177]. Copyright 2004 with permission from Elsevier Ltd.

7.2.4. Application of PtZn in the PEMFC

A PtZn GDL was prepared and used as a fuel cell catalyst in **Chapter 4**. Our alloy exhibited enhanced performance in the single stack fuel cell compared to the one with a Pt MEA. However, the power output of the fuel cell was significantly worse than the one reported in literature. Experimental optimization for *e.g.,* the Zn deposition process or hot-pressing conditions, is necessary to achieve adequate power output.

It is also important to investigate the stability of the PtZn alloy under fuel cell operating conditions. In **Chapter 6**, we examined the chemical stability of PtZn in an electrochemical cell at room temperature, but this method may not sufficiently mimic the fuel cell conditions. It is also important to test the durability of components, i.e. membrane and GDL, in a fuel cell containing a PtZn catalyst.

7.2.5. *In-situ* Neutron reflectometry

Neutron reflectometry (NR) is a powerful technique used to investigate the metal/liquid, metal/gas, or the thin film formed on a metal surface with the probing depth from a few to thousands of angstroms in the direction normal to the sample surface. A collimated neutron beam is directed to a surface of interest at an extreme grazing angle. The neutrons interact with the nuclei of the atoms, and the reflectivity of neutron is measured as a function of momentum transfer, which is related to the angle of incidence, the wavelength of the neutron beam, and the *scattering-length density,* ρ, which is defined as,

$$\rho = \sum_j b_j n_j \tag{7-2}$$

In this equation, b_j is the number density of nuclei j, and n_j is nucleus-dependent *coherent neutron scattering length* analogous to the refractive indices of materials for neutrons [178]. In practice, the angle of incidence or the wavelength of the neutron beam is changed (thus the

penetration depth of the beam into the sample) and the scattering-length density is measured to probe the metal surface or the corresponding interface.

NR also allows us to measure the metal surface while electrochemistry is performed on the sample [179-181]. In **Chapter 5**, we observed surface segregation of Pt or Zn, depending on different molecules adsorbed onto the surface of the PtZn. Surface enrichment of one component of the alloy may be observed by NR if the scattering-length density of Pt and Zn is sufficiently different. According to Noel *et al*., [180], two materials with their scattering-length densities differ by 1×10^{-6} Å^{-2} are clearly distinguishable. According to NIST Centre for Neutron Research [182], the values for n_{Pt} and n_{Zn} are 9.60 and 5.682 fm, respectively. Assuming their b values are equal or similar, as our PtZn is 1:1 in atomic composition and the lattice mismatch is small, we should be able to see a reasonable contrast between Pt and Zn. Also, we can monitor the layering of Pt and Zn and watch the movement of Zn or Pt to the surface when ORR or CO oxidation is performed. The NR facility is available at Canadian Neutron Beam Centre in National Research Council of Canada, located in Chalk River, Ontario.

8. References

[1] H. Hassanzadeh, S. Mansouri, Proc IME J Power Energ, 219 (2005) 245-254.

[2] X. Li, *Principles of Fuel Cells*, Taylor & Francis Group, NY, 2006.

[3] M. Al-Baghdadi, in: Fuel Cell Research Trends. Vasquez, L.O. ed., Nova Science Publisher Inc., New York, 2007, p. 273 Ch. 7.

[4] Kitco Preious Metals. Accessed October 23, 2008.
<http://www.kitco.com/charts/liveplatinum.html>.

[5] T. He, E. Kreidler, L. Xiong, E. Ding, J. Power Sources, 165 (2007) 87-91.

[6] Kitco Base Metals. Accessed October 23, 2008. <http://www.kitcometals.com/>.

[7] A. Sode, W. Li, Y. Yang, P. Wong, E. Gyenge, K. Mitchell, D. Bizzotto, J. Phys. Chem. B, 110 (2006) 8715-8722.

[8] A. Sode, D. Bizzotto, Electrochimica Acta, 54 (2009) 1095-1101.

[9] A. Bard, L. Faulkner, *Electrochemical Methods: Fundamentals and Applications.*, 2nd ed., John Wiley & Sons Inc., New York, 2001.

[10] N. Lang, W. Kohn, Phys. Rev. B, 1 (1970) 4555-4568.

[11] G. Somorjai, *Chemistry in Two Dimentions*, Cornell University Press, USA, 1981.

[12] S. Trasatti, in: Handbook of Fuel Cells - Fundamentals, Technology, and Applications. Woulf Vielstich, Hubert A. Gasteiger, and Arnold Lamm eds., John Wiley & Sons Ltd., New York, 2003, pp. 81, Ch. 9.

[13] G. Ertl, Angew. Chem. Int. Ed., 47 (2008) 3524-3535.

[14] G. Somorjai, in: Chemistry in Two Dimentions, Cornell University Press, USA, 1981, pp. 381-413.

[15] N. Markovic, P.J. Ross, in: Interfacial Electrochemistry: Theory, Experiment, and Applications. A. Wieckowski ed., Marcel Dekker, Inc., New York, 1999, p. 821 Ch. 46.

[16] S. Trasatti, in: Handbook of Fuel Cells - Fundamentals, Technology, and Applications. Woulf Vielstich, Hubert A. Gasteiger, and Arnold Lamm eds., John Wiley & Sons Ltd., New York, 2003, pp. 71-78 Ch.8.

[17] S. Trasatti, in: Handbook of Fuel Cells. Wolf Vielstich, Arnold Lamm, Hubert A. Gasteiger (Eds.), John Wiley & Sons Ltd., New York, 2003, p. 88 (Ch. 10).

[18] J. Clavilier, R. Faure, R. Durand, J. Electroanal. Chem., 107 (1980) 205-209.

[19] J. Clavilier, D. Armanda, B. Wu, J. Electroanal. Chem., 135 (1982) 159-166.

[20] C. Green, A. Kucernak, J. Phys. Chem. B, 106 (2002) 1036-1047.

[21] N. Anastasijevic, V. Vesovic, R. Adzic, J. Electroanal. Chem., 229 (1987) 305.

[22] M. Gattrell, B. MacDougall, in: Handbook of Fuel Cells - Fundamentals, Technology, and Applications. Woulf Vielstich, Hubert A. Gasteiger, and Arnold Lamm eds., John Wiley & Sons Ltd., New York, 2003, pp. 443-464.

[23] E. Yeager, J. Mol. Catal, 38 (1986) 5.

[24] S. Chen, A. Kucernak, J. Phys. Chem. B, 108 (2004) 3262-3272.

[25] A. Damjanovic, D. Sepa, M. Vojnovic, Electrochim. Acta, 24 (1979) 887-889.

[26] V. Stamenkovic, T. Schmidt, P. Ross, N. Markovic, J. Phys. Chem. B, 106 (2002) 11970-11979.

[27] M.D. Macia, J.M. Campiña, E. Herrero, J.M. Feliu, J. Electroanal. Chem., 564 (2004) 141-150.

[28] A. Damjanovic, V. Brusic, Electrochim. Acta, 12 (1967) 615-628.

[29] N. Markovic, H. Gasteiger, P.N. Ross, J. Electrochem. Soc., 144 (1997) 1591-1597.

[30] R. Adzic, in: Electrocatalysis. Lipkowski, J. and Ross, P.N. eds., Wiley-VCH, New York, 1998, pp. 197, Ch.5.

[31] E. Yeager, Electrochim. Acta, 29 (1984) 1527-1537.

[32] O. Antorine, Y. Baltel, R. Durand, J. Electroanal. Chem., 499 (2001) 85-94.

[33] D. Sepa, M. Vojnovic, L. Vracar, A. Damjanovic, Electrochim. Acta, 32 (1987) 129-134.

[34] S. Mukerjee, J. Appl. Electrochem., 20 (1990) 537-548.

[35] J. Norskov, J. Rossmeisl, A. Logadottir, L. Lindqvist, J. Kitchin, T. Bligaard, H. Jonsson, J. Phys. Chem. B, 108 (2004) 17886-17892.

[36] A. Damjanovic, J.O. Bockris, Electrochim. Acta, 11 (1966) 376-377.

[37] N. Markovioc, H. Gasteiger, P. Ross, J. Phys. Chem., 100 (1996) 6715-6721.

[38] P. Faguy, N.M. Markovic, P.J. Ross, J. Electrochem. Soc., 140 (1993) 1638-1641.

[39] J. Clavilier, R. Durand, G. Guinet, R. Faure, J. Electroanal. Chem., 127 (1981) 281-287.

[40] A.C. Luntz, M.D. Williams, D.S. Bethune, J. Chem. Phys., 89 (1988) 4381-4395.

[41] A.T. Gee, B.E. Hayden, J. Chem. Phys., 113 (2000) 10333-10343.

[42] P. Gambardella, Ž. Šljivančanin, B. Hammer, M. Blanc, K. Kuhnke, K. Kern, Phys. Rev. Lett., 87 (2001) 056103.

[43] B. Beden, F. Hahn, J. Leger, C. Lamy, J. Electroanal. Chem., 258 (1989) 463-467.

[44] J. Wintterlin, S. Volkening, T.V. Janssens, T. Zambelli, G. Ertl, Science, 278 (1997) 1931-1934.

[45] S. Enback, G. Lindbergh, J. Electrochem. Soc., 152 (2004) A23-A31.

[46] M. Liao, C.R. Cabrera, Y. Ishikawa, Surf. Sci., 445 (2000) 267-282.

[47] Laidler, K.J, Meiser, John H, *Physical Chemistry*, 3rd ed., Houghton Mifflin College Div, MA, 1999.

[48] C.T. Campbell, G. Ertl, H. Kuipers, J. Segner, J. Chem. Phys., 73 (1980) 5862-5873.

[49] G. Jerkiewicz, G. Vatankhah, J. Lessard, M.P. Soriaga, Y. Park, Electrochim. Acta, 49 (2004) 1451-1459.

[50] B. Andreaus, F. Maillard, J. Kocylo, E. Savinova, M. Eikerling, J. Phys. Chem. B, 110 (2006) 21028-21040.

[51] C. Lamy, J. Leger, J. Electroanal. Chem., 150 (1983) 71-77.

[52] E. Herrero, B. Álvarez, J.M. Feliu, S. Blais, Z. Radovic-Hrapovic, G. Jerkiewicz, J. Electroanal. Chem., 567 (2004) 139-149.

[53] A. Cuesta, A. Couto, A. Rincón, M. Pérez, A. López-Cudero, C. Gutiérrez, J. Electroanal. Chem., 586 (2006) 184-195.

[54] A. Miki, S. Ye, T. Senzaki, M. Osawa, J. Electroanal. Chem., 563 (2004) 23-31.

[55] A. López-Cudero, A. Cuesta, C. Gutiérrez, J. Electroanal. Chem., 548 (2003) 109-119.

[56] K. Chou, N. Markovic, J. Kim, P. Ross, G. Somorjai, J. Phys. Chem. B, 107 (2003) 1840-

1844.

[57] C. McCallum, D. Pletcher, J. Electroanal. Chem., 70 (1976) 277-290.

[58] K. Mikita, M. Nakamura, N. Hoshi, Langmuir, 23 (2007) 9092-9097.

[59] J. Xu, J. Yates, J. Chem. Phys., 99 (1993) 725-732.

[60] J. Yates, Jr., J. Vac. Sci. Technol. A., 13 (1995) 1359-1367.

[61] F. Besenbacher, I. Stensgaard, in: The Chemical Physics of Solid Surfaces. King, D.A. and Woodruff, D.P. eds., Elsevier, Amsterdam, 1994, pp. 573-629 Ch.14.

[62] N.M. Markovic, P.N. Ross, Surf. Sci. Rep., 45 (2002) 117-229.

[63] D. Woodruff, in: The Chemical Physics of Solid Surfaces. King, D.A. and Woodruff, D.P. eds., Elsevier, Amsterdam, 1994, pp. 465-499. Ch.12.

[64] T. Gritsch, D. Coulman, R.J. Behm, G. Ertl, Phys. Rev. Lett., 63 (1989) 1086.

[65] R.J. Behm, P.A. Thiel, P.R. Norton, G. Ertl, J. Chem. Phys., 78 (1983) 7437-7447.

[66] P.A. Thiel, R.J. Behm, P.R. Norton, G. Ertl, J. Chem. Phys., 78 (1983) 7448-7458.

[67] G. Chen, D.A. Delafuente, S. Sarangapani, T.E. Mallouk, Catal. Today, 67 (2001) 341-355.

[68] J. Whitacre, T. Valdez, S. Narayanan, Electrochim.Acta, 53 (2008) 3680-3689.

[69] H.R. Colón-Mercado, B.N. Popov, J. Power Sources, 155 (2006) 253-263.

[70] S. Mukerjee, S. Srinivasan, M.P. Soriaga, J. McBreen, J. Phys. Chem., 99 (1995) 4577-4589.

[71] B. Brown, S.D. Wolter, B.R. Stoner, J.T. Glass, J. Electrochem. Soc., 155 (2008) B852-B859.

[72] M. Mavrikakis, B. Hammer, J.K. Nørskov, Phys. Rev. Lett., 81 (1998) 2819.

[73] S. Mukerjee, S. Srinivasan, J. Electroanal. Chem., 357 (1993) 201-224.

[74] N. Markovic, T. Schmidt, P. Ross, Fuel Cells, 1 (2001) 105-116.

[75] Y. Xu, A. Ruban, M. Mavrikakis, J. Am. Chem. Soc., 126 (2004) 4717-4725.

[76] U. Bardi, B. Beard, P. Ross, J. Catal., 124 (1990) 22-29.

[77] S. Hsieh, T. Matsumoto, M. Batzill, B. Koel, Phys. Rev. B, 68 (2003) 205417/1-205417/11.

[78] J.G. Chen, C.A. Menning, M.B. Zellner, Surf. Sci. Rep., 63 (2008) 201-254.

[79] G. Treglia, B. Legrand, F. Ducastelle, A. Saul, C. Gallis, I. Meunier, C. Mottet, A. Senhaji, Comput. Mater. Sci., 15 (1999) 196-235.

[80] V. Stamenkovic, T.J. Schmidt, P.N. Ross, N.M. Markovic, J. Electroanal. Chem., 554-555 (2003) 191-199.

[81] P. Liu, A. Logadottir, J.K. Nørskov, Electrochim. Acta, 48 (2003) 3731-3742.

[82] C. Roth, A. Papworth, I. Hussain, R. Nichols, D. Schiffrin, J. Electroanal. Chem., 581 (2005) 79-85.

[83] H.A. Gasteiger, N. Markovic, P.N. Ross, Jr., E.J. Cairns, J. Phys. Chem., 98 (1994) 617-625.

[84] H.A. Gasteiger, N.M. Markovic, P.N. Ross, J. Phys. Chem., 99 (1995) 8290-8301.

[85] M. Watanabe, S. Motoo, J. Electroanal. Chem., 60 (1975) 267-273.

[86] M. Arenz, V. Stamenkovic, B. Blizanac, K. Mayrhofer, N. Markovic, P. Ross, J. Catal., 232 (2005) 402-410.

[87] S. Sen Gupta, J. Datta, J. Electroanal. Chem., 594 (2006) 65-72.

[88] A. Kalinkin, A. Pashis, V. Bukhtiyarov, Kinet. Catal., 48 (2007) 298-304.

[89] B.N. Grgur, N.M. Markovic, P.N. Ross, Electrochim. Acta, 43 (1998) 3631-3635.

[90] A. Aramata, I. Toyoshima, M. Enyo, Electrochim. Acta, 37 (1992) 1317-1320.

[91] M. Janssen, J. Moolhuysen, J. Catal., 46 (1977) 289-296.

[92] C. Lu, C. Rice, R. Masel, P. Babu, P. Waszczuk, H. Kim, E. Oldfield, A. Wieckowski, J. Phys. Chem. B, 106 (2002) 9581-9589.

[93] T. Frelink, W. Visscher, A.P. Cox, J.A.R. van Veen, Electrochim. Acta, 40 (1995) 1537-1543.

[94] C. Roth, N. Benker, T. Buhrmester, M. Mazurek, M. Loster, H. Fuess, D. Koningsberger, D. Ramaker, J. Am. Chem. Soc., 127 (2005) 14607-14615.

[95] P. Waszczuk, G.-. Lu, A. Wieckowski, C. Lu, C. Rice, R.I. Masel, Electrochim. Acta, 47 (2002) 3637-3652.

[96] J. Spendelow, P. Babu, A. Wieckowski, Curr. Opin. Solid State Mater. Sci., 9 (2005) 37-48.

[97] H.A. Gasteiger, S.S. Kocha, B. Sompalli, F.T. Wagner, Appl. Catal., B, 56 (2005) 9-35.

[98] S. Mukerjee, S. Srinivasan, in: Handbook of Fuel Cells - Fundamentals, Technology, and Applications. Woulf Vielstich, Hubert A. Gasteiger, and Arnold Lamm eds., John Wiley & Sons Ltd., New York, 2003, pp. 502-519 Ch. 34.

[99] G. Somorjai, M. Van Hove, Prog. in Sur. Sci., 29-30 (1989) 201-231.

[100] A. West, *Basic Solid State Chemistry*, 2nd ed., John Wiley & Sons Inc., West Sussex, UK, 1999.

[101] Z. Chen, K.M. Neyman, A.B. Gordienko, N. Rösch, Phys. Rev. B, 68 (2003) 075417.

[102] Z. Moser, J. Phase. Equilib, 12 (1991) 439-443.

[103] S. Taguchi, A. Aramata, J. Electroanal. Chem., 457 (1998) 73-81.

[104] D. Kolb, Adv. in Electrochem. and Electrochem. Eng., 11 (1978) 125.

[105] A. Aramata, M. Quaiyyum, W.A. Balais, T. Atoguchi, J. Electroanal. Chem., 338 (1992) 367-372.

[106] A. Despic, M. Pavlovic, Electrochim. Acta, 27 (1982) 1539-1549.

[107] E. Guerra, G.H. Kelsall, M. Bestetti, D. Dreisinger, K. Wong, K.A.R. Mitchell, D. Bizzotto, J. Electrochem. Soc., 151 (2004) E1-E6.

[108] M. Quaiyyum, A. Aramata, S. Moniwa, S. Taguchi, M. Enyo, J. Electroanal. Chem., 373 (1994) 61-66.

[109] V. Sudha, M. Sangaranarayanan, J. Chem. Sci., 117 (2005) 207-218.

[110] H. Uhlig, J. MacNairn, D. Vaughn, Acta Metall. , 3 (1955) 302-304.

[111] S. Taguchi, A. Aramata, J. Electroanal. Chem., 374 (1994) 275-277.

[112] J.A. Rodriguez, M. Kuhn, J. Chem. Phys., 102 (1995) 4279-4289.

[113] Handbook of Chemistry and Physics. Accessed on September 19, 2008. <http://www.hbcpnetbase.com/>.

[114] J. Fernandez, D. Walsh, A. Bard, J. Am. Chem. Soc., 127 (2005) 357-365.

[115] S. Cameron, D. Dwyer, Surf. Sci., 176 (1986) L857-L862.

[116] A. Linsebigler, G. Lu, J. Yates, Surf. Sci., 294 (1993) 284-296.

[117] R. Demmin, S. Shivaprasad, T. Madey, Langmuir, 4 (1988) 1104-1108.

[118] S. Mukerjee, S. Srinivasan, M.P. Soriaga, J. McBreen, J. Electrochem. Soc., 142 (1995) 1409-1422.

[119] Rodriguez, J.A., Surf. Sci., 289 (1993) L584-L590.

[120] J.A. Rodriguez, J. Hrbek, J. Vac. Sci. Technol. A., 12 (1994) 2153-2158.

[121] J. Rodriguez, Science (Washington, D.C.), 257 (1992) 897-903.

[122] W. Albery, M. Hitchman, *Ring-disc Electrodes*, Oxford University Press, London, UK, 1971.

[123] V. Filinovsky, Y. Pleskov, in: Comprehensive Treatise of Electrochemistry., J.O. Bockris ed., Plenum Press, New York, 1980.

[124] H.J. Mathieu, in: Surface Analysis - The Principal Technique, John Wiley & Sons Ltd., 1997, p. 99.

[125] M.P. Seah, W.A. Dench, Surf. Interface Anal., 1 (1979) 2-11.

[126] J. Riviere, *Surface Analytical Techniques*, Claresdon Press, Oxford, 1990.

[127] L. Reimer, *Scanning Electron Microscopy: Physics of Image Formation and Microanalysis*, Springer-Verlag, Berlin, 1985.

[128] J. Bozzola, L. Russell, *Electron Microscopy: Principles and Techniques for Biologist*, 2nd ed., Jones & Bartlett Publishers, Sudbury, 1998.

[129] S.J. Hill, *Inductively Coupled Plasma Spectroscopy And Its Application*, 1st ed., CRC Press, Florida, 1999.

[130] S.M. Nelms, *ICP Mass Spetrometry Handbook*, 1st ed., Blackwell Publishing, Florida, 2005.

[131] S. Kocha, in: Handbook of Fuel Cells - Fundamentals, Technology, and Applications. Woulf Vielstich, Hubert A. Gasteiger, and Arnold Lamm eds., John Wiley & Sons Ltd., New York, 2003, pp. 538-565 Ch.43.

[132] L. Xiong, A. Manthiram, Electrochim. Acta, 50 (2005) 3200-3204.

[133] S. Litster, G. McLean, J. Power Sources, 130 (2004) 61-76.

[134] T. Ralph, M. Hogarth, Platinum Met. Rev., 46 (2002) 3-14.

[135] X. Li, H. Colón-Mercado, G. Wu, J. Lee, B. Popov, ECS Trans., 11 (2007) 1259-1266.

[136] M. Vos, D. Van den Marel, G. Sawatzky, Phys. Rev. B, 29 (1984) 3073-3084.

[137] P.A. Bennett, J.C. Fuggle, F.U. Hillebrecht, A. Lenselink, G.A. Sawatzky, Phys. Rev. B, 27 (1983) 2194.

[138] A. Aramata, S. Taguchi, T. Fukuda, M. Nakamura, G. Horányi, Electrochim. Acta, 44 (1998) 999-1007.

[139] E. Guerra, Ph.D. dissertation, UBC, Vancouver, (2003).

[140] U. Paulus, A. Wokaun, G. Scherer, T. Schmidt, V. Stamenkovic, V. Radmilovic, N. Markovic, P. Ross, J. Phys. Chem. B, 106 (2002) 4181-4191.

[141] S.J. Seo, H. Joh, H.T. Kim, S.H. Moon, J. Power Sources, 163 (2006) 403-408.

[142] R. Connel, M.SC. Dissertation, UBC, Vancouver, (2005).

[143] J. Rodriguez, M. Kuhn, J. Phys. Chem., 100 (1996) 381-389.

[144] J. Rodriguez, Surf. Sci. Rep., 24 (1996) 223-287.

[145] Taft, C. A., Guimaraes, T. C., Pavao, A. C., Lester, W. A., Int. Rev. Phys. Chem., 18 (1999) 163-233.

[146] F. Buatier de Mongeot, M. Scherer, B. Gleich, E. Kopatzki, R. Behm, Surf. Sci., 411 (1998) 249-262.

[147] T. Biegler, D. Rand, R. Woods, J. Electroanal. Chem., 29 (1971) 269.

[148] P.L. Cavallotti, M. Bestetti, S. Franz, Electrochim. Acta, 48 (2003) 3013-3020.

[149] S. Itoh, N. Yamazoe, T. Seiyama, Surf. Technol., 5 (1977) 27-42.

[150] K. Raeissi, A. Saatchi, M. Golozar, J. Szpunar, J. Appl. Electrochem., 34 (2004) 1249-1258.

[151] V.M. Kozlov, L. Peraldo Bicelli, Mater. Chem. Phys., 77 (2003) 289-293.

[152] M. Arenz, K. Mayrhofer, V. Stamenkovic, B. Blizanac, T. Tada, P. Ross, N. Markovic, J. Am. Chem. Soc., 127 (2005) 6819-6829.

[153] Y.G. Shen, D.J. O'Connor, J. Yao, Appl. Surf. Sci., 125 (1998) 300-312.

[154] B.C. Han, A. Van der Ven, G. Ceder, B. Hwang, Phys. Rev. B, 72 (2005) 205409-9.

[155] S. Le, A. Navrotsky, J. Solid State Chem., 180 (2007) 2443-2451.

[156] Y. Nagano, J. Therm. Anal. Cal., 69 (2002) 831-839.

[157] N. Lebedeva, M. Koper, J. Feliu, R. van Santen, J. Phys. Chem. B, 106 (2002) 12938-12947.

[158] A. LaConti, R. McDonald, in: Handbook of Fuel Cells - Fundamentals, Technology, and Applications. Woulf Vielstich, Hubert A. Gasteiger, and Arnold Lamm eds., John Wiley & Sons Ltd., New York, 2003, pp. 647-677. Ch.49.

[159] Y. Shao, G. Yin, Y. Gao, J. Power Sources, 171 (2007) 558-566.

[160] A. Arico, A. Stassi, E. Modica, R. Ornelas, I. Gatto, E. Passalacqua, V. Antonucci, J. Power Sources, 178 (2008) 525-536.

[161] E. Antolini, J.R. Salgado, E.R. Gonzalez, J. Power Sources, 160 (2006) 957-968.

[162] Z. Wei, H. Guo, Z. Tang, J. Power Sources, 62 (1996) 233-236.

[163] H.R. Colón-Mercado, H. Kim, B.N. Popov, Electrochem. Commun., 6 (2004) 795-799.

[164] U.A. Paulus, T.J. Schmidt, H.A. Gasteiger, R.J. Behm, J. Electroanal. Chem., 495 (2001) 134-145.

[165] H. Zietzman, B.Sc. Dissertation, UBC, Vancouver, (2007).

[166] A. Bard, M.E. Mirkin, *Scanning Electrochemical Microscopy*, Marcel Dekker, Inc., New York, 2001.

[167] J. Kwak, A. Bard, Anal. Chem., 61 1221-1227.

[168] X. Lu, Q. Wang, X. Liu, Anal. Chim. Acta, 601 (2007) 10-25.

[169] M.V. Mirkin, B.R. Horrocks, Anal. Chim. Acta, 406 (2000) 119-146.

[170] J. Fernandez, A. Bard, Anal. Chem., 75 (2003) 2967-2974.

[171] J. Fernandez, A. Bard, Anal. Chem., 76 (2004) 2281-2289.

[172] C. Puglia, A. Nilsson, B. Hernnäs, O. Karis, P. Bennich, N. Mårtensson, Surf. Sci., 342 (1995) 119-133.

[173] V. Stamenkovic, B.S. Mun, K.J. Mayrhofer, P.N. Ross, N.M. Markovic, J. Rossmeisl, J. Greeley, J.K. Nørskov, Angew. Chem. Int. Ed., 45 (2006) 2897-2901.

[174] J. Greeley, J. Nørskov, Electrochimica Acta, 52 (2007) 5829-5836.

[175] Y. Okano, A. Katagiri, J. Electrochem. Soc., 144 (1997) 1927-1932.

[176] W. Harding, Surf. Finish., 65 (1978) 30.

[177] J. Huang, I. Sun, Electrochim.Acta, 49 (2004) 3251-3258.

[178] R. Thomas, Annu. Rev. Phys. Chem., 55 (2004) 391-426.

[179] J.J. Noel, H.L. Jensen, Z. Tun, D.W. Shoesmith, Electrochem. Solid-State Lett., 3 (2000) 473-476.

[180] J.J. Noel, D.W. Shoesmith, Z. Tun, J. Electrochem. Soc., 155 (2008) C444-C454.

[181] V. Zamlynny, I. Burgess, G. Szymanski, J. Lipkowski, J. Majewski, G. Smith, S. Satija, R. Ivkov, Langmuir, 16 (2000) 9861-9870.

[182] NIST Center for Neutron Research, Accessed October 25, 2008. <http://www.ncnr.nist.gov/resources/n-lengths/list.html>.